Numerical simulation of electromagnetic fields in complex multi-cavity superconducting radio frequency resonators

Dissertation
zur
Erlangung des akademischen Grades
Doktor-Ingenieur (Dr.-Ing.)
der Fakultät für Informatik und Elektrotechnik
der Universität Rostock

vorgelegt von
Johann Heller, geboren am 14.03.1990 in Rostock
Rostock, 10. Oktober 2018
Verteidigung: 20. Dezember 2018

Gutachter:
Prof. Dr. rer. nat. habil. U. van Rienen, Universität Rostock
Prof. Dr. ing. H. De Gersem, Technische Universität Darmstadt

https://doi.org/10.18453/rosdok_id00002402

Optimism is true moral courage.

– Sir Ernest Shackleton, South: The Endurance Expedition

Zusammenfassung

Diese Arbeit befasst sich mit der Berechnung elektromagnetischer Felder in komplexen, supraleitenden Resonatoren. Für den Betrieb und das Design solcher Resonatoren ist eine effektive und genaue Berechnung derartiger Felder notwendig. Dies ist mit Hilfe konventioneller Hardware in vielen Fällen kaum möglich. Durch diese Limitation werden in der Praxis daher meist zwei verschiedene Auswege gewählt: zum einen die Parallelisierung des Problems auf kostenintensiver Hardware mit hoher Leistungsaufnahme und zum anderen die Vereinfachung der Struktur. In dieser Arbeit wird ein Verfahren untersucht und automatisiert, welches diese Lücke schließen soll und die genannten Probleme ohne grobe Vereinfachung der Struktur auf Arbeitsplatzrechnern lösen kann. Bei dem verwendeten Verfahren *State-Space Concatenation* (SSC) wird mit Hilfe einer Kombination aus Modellordnungsreduktion und Gebietszerlegung der Berechnungsaufwand stark reduziert. Für eine effektive Verwendung wurde in dieser Arbeit eine Automatisierung von SSC für nahezu beliebige Hochfrequenzresonatoren implementiert und getestet. Ein weiteres Problem ist die effektive Berechnung der Verluste derartiger Resonanzen durch die Koppler und Strahlrohre. Daher wird in dieser Arbeit ein Störungsansatz verwandt, welcher auf SSC beruht. Das daraus entstehende nichtlineare Eigenwertproblem wird mit Hilfe des Newton-Verfahrens gelöst und erlaubt eine vergleichsweise schnelle Berechnung derartiger Verluste. Die verwandte Methode wird auf ihre physikalische Konsistenz getestet und teilweise mit Messergebnissen verglichen. Zusammenfassend werden alle in dieser Arbeit erdachten und implementierten Methoden an drei state-of-the-art Problemen aus der aktuellen Beschleunigerphysik getestet. Dabei werden aktuelle Fragestellungen der Forschung für das Third Harmonic Module des FLASH-Beschleunigers, des bERLinPro Haupt-Linacs sowie des Designs der BESSY$^{\mathrm{VSR}}$ Resonatoren beantwortet.

Abstract

This thesis deals with the computation of electromagnetic fields in complex, superconducting resonators. For the operation and design of such resonators, an efficient and accurate computation of these fields is necessary, which is hardly possible on conventional hardware in many cases. Due to this limitation, there are generally two different approaches in practice: on the one hand, the parallelization of the problem on costly hardware with high power consumption and, on the other hand, the simplification of the structure. In this thesis a method is investigated and automated to close this gap, which can solve the considered problems without extensively simplifying the structure on workstation computers. The used method, *State-Space Concatenation* (SSC) employs a combination of model order reduction and domain decomposition to significantly reduce the computational effort needed. For an efficient use of SSC, in this thesis an automation, ready to handle almost arbitrary high-frequency resonators is implemented and tested. Another problem is the efficient calculation of the losses of such resonances by the couplers and beampipes. Hence, this work is using a perturbation approach based on SSC. The resulting nonlinear eigenvalue problem is solved by using the Newton method, which allows for the comparatively fast computation of such losses. The exploited method is tested for physical consistency and partly compared to measurement results. In summary, all the methods discussed and implemented in this work are tested for three state of the art problems from accelerator physics. In the process current research questions for the Third Harmonic Module of the FLASH accelerator, the bERLinPro main linear accelerator (linac) and the BESSY$^{\mathrm{VSR}}$ cavity-design will be answered.

Acknowledgement

I would like to show my deepest acknowledgement and gratitude to several people.

- Professor Ursula van Rienen for letting me work at her group, for always trusting in my skills and letting me realize my ideas (even if they sometimes did not work out) and for the grading of this thesis. I had a wonderful time in the work-group and I will never forget it.
- Professor Herbert De Gersem for the review of this thesis and many helpful discussion during conferences and workshops.
- My friend Tomasz Galek for listening to my (sometimes outlandish) ideas, the help with the pole-fitting and the multi-pole expansion for bERLinPro , countless discussions about scifi, literature, AI, astrophysics and philosophy and for many, many unforgettable anecdotes during this time.
- My friend Thomas Flisgen, who mentored me during my time as a student and PhD candidate, always had an open ear for my questions and ideas and without whom, neither would this thesis exist, nor would I probably have even half of my skills in field-theory and linear algebra.
- My friend Franzi Reimann for interesting morning discussions about literature and philosophy as well as listening to my doubts.
- My friend Korinna Brackebusch for Mensa-lunch motivation and listening to my sorrows.
- My friend Christian Bahls for many valuable insights and WhatsApp pep talks about finishing my thesis.
- To all the students I had the pleasure to work with, especially Konstantin, Hermann, Emanuelle, Gowrishankar, Rishab and Prasanth for being fun to work with and being so smart that it pushed me a lot.
- All of my colleagues at the IAE, namely Christian S., Dawei Z., Shahnam Z., Eden T., Alex M., Andrea B., Hendrikje R. and Dirk H. It was always a blast working with so many talented and friendly people.
- Maja, Kathrin and Dr. Himmel without whom the entire institute would probably fall apart within weeks.

- My "brother" Joshi for being my friend and an inspiration.
- All of my friends, especially Roccy, Bennie and Max for being people I can always count on.
- My (twin)-brother Jakob, for being my role model in his strength of character and wisdom, for his unconditional support and advice.
- My cats Louis and Sir Ernest for trying countless times to sit on the keyboard in effort to make a contribution to this thesis. Unfortunately, none of their helpful changes made it into the final version.
- My In-Laws Ines and Uwe, for their moral support during my studies and letting me be part of their family.
- To my brother Paul and sister Jule for giving me such a wonderful and loving childhood, moral support and language editing this thesis.
- My father Detlef, for his unconditional love, trust and pride in me, for teaching me discipline, strength, grit and self-esteem and for giving a young boy a dream and faith that he could be a scientist just as his heroes in the books he loved so much.
- My mother Barbara and her husband Olaf, for their loving support through all my education and for a wonderful and loving childhood.
- To Annemarie for giving me her unconditional love and support even when I worked through weekends and sometimes vacations. Thank you for being such an important part of my life.

Thesis Statements

of the dissertation

Numerical simulation of electromagnetic fields in complex multi-cavity superconducting radio frequency resonators

by Johann Heller

1. For the design and operation of strings of superconducting cavities, the numerical computation of their electromagnetic resonances is a standard task in accelerator physics. Unfortunately, due to the high computational demand, this task is often performed using either major simplifications of the structure or by parallelizing the computations on expensive hardware.

2. The State-Space Concatenation (SSC) algorithm is an excellent solution to solving Maxwell's equations in large superconducting radio-frequency structures. By employing a combination of domain decomposition and model-order reduction, the computational demand can be lowered such that the required investigations can be performed, without simplifications of the structure, on standard workstation computers.

3. The simplifications of the structures commonly introduced for such multi-cavity resonators are only valid for certain modes which are confined to substructures such as the cavities. Therefore, the computation of the fields in the full structure is inevitable, even below the first cutoff frequency of the beampipe.

4. The combination of SSC with modern discretization techniques is required for the efficient usage. Both techniques, the Finite Integration Technique (FIT) as well as the Finite Element Method (FEM), allow for the discretization of Maxwell's equations in the substructures. Furthermore, for both discretization techniques, there are strong hints that for simple topologies, the combination with SSC does not disturb the underlying convergence order regarding the number of degrees of freedom (DOF).

5. For high reliability and performance an automation of SSC is needed. For the underlying discretization FIT is an appropriate candidate due to the availability of powerful commercial software such as CST Microwave Studio ® which allows the export of the matrices arising from the discretization.

6. The presented implementation of SSC is validated with an analytical example which shows that the accuracy of solutions in both field and frequencies increases with the number of degrees of freedom with the expected convergence order. The implementation has some minor limitations that mostly originate

from the underlying commercial software, especially regarding the placing of the waveguide ports.

7. Compared to other domain decompositions that are applied in accelerator physics, SSC has several advantages, especially the fact that fields are readily available in a cheap post processing step.

8. The computation of external losses leads to a Nonlinear Eigenvalue Problem (NLEVP). The commonly applied solution approaches of the NLEVP are inefficient for large structures. While several approaches were proposed in the past, none of them can compute large numbers of solutions without major simplifications of the structure or the requirement of expensive hardware.

9. The non-simplified solution of the NLEVP is inevitable due to the shortcoming of the simplified solutions. A perturbation approach based on discretized Maxwell's equations in the closed structure can achieve an efficient discretization of the NLEVP.

10. The Newton method offers an effective solution to the NLEVP. While the convergence is guaranteed if certain parameters are met, there is no guarantee that all solutions in a certain frequency domain are found.

11. The algorithms proposed in this thesis are able to investigate lossless as well as lossy (restricted to external losses) electromagnetic fields in real-life structures with several millions of degrees of freedom. Furthermore, the method is logically consistent and the results agree well with available measurements.

12. The introduced algorithms for the solution of the Helmholtz-equation and the NLEVP are very well suited to investigate real-life examples of SRF structures. Possible applications are the identification of potentially disruptive modes and the comparison of different design-candidates. Both are shown on three real-life applications, namely the FLASH Third Harmonic Module, the bERLinPro main linac, as well as the BESSY$^{\mathrm{VSR}}$ cavities.

Inhaltsverzeichnis

List of Acronyms

ACE3P	Advanced Computational Electromagnetic 3D Parallel
bERLinPro	Berlin Energy Recovery Linac Prototype
BESSY$^{\text{VSR}}$	Upgrade to BESSY II - The variable pulse-length storage ring
CME	Corrected Modal Expansion
CSC	Coupled S-Parameter Calculation
CST MWS	CST MICROWAVE STUDIO®
DESY	Deutsches Elektronen Synchrotron
DLL	Dynamic Link Library
DOF	Degree of Freedom
FEM	Finite Element Method
FLASH	Free-Electron Laser Hamburg
GSM	Globalised Scattering Matrix
HOM	Higher Order Mode
HZB	Helmholtz Zentrum Berlin
Linac	Linear Accelerator
LHC	Large Hadron Collider
MOR	Model Order Reduction
NM	Newton Method
PBA	Perfect Boundary Approximation
PEC	Perfect Electric Conducting
PETSc	Portable, Extensible Toolkit for Scientific Computation
PMC	Perfect Magnetic Conducting
PML	Perfectly Matched Layer
POD	Proper Orthogonal Decomposition
RAM	Random-access Memory
ROM	Reduced Order Model
ROSWELL	Rostock Maxwell
SPICE	Simulation Program with Integrated Circuit Emphasis
SRF	Superconducting Radio-Frequency
SSC	State-Space Concatenations
SSM	State-Space Model
SVD	Singular Value Decomposition
TESLA	TeV-Energy Superconducting Linear Accelerator

TE	Transverse Electric
TEM	Transverse Electromagnetic
TM	Transverse Magnetic

List of Symbols

Symbol	Unit	Description
a	m	Width of rectangular waveguide
$\mathbf{a}_{\mathrm{ext}}(t)$	$\sqrt{\mathrm{V\,A}}$	Normalized, incident wave-amplitude
$\mathtt{A}_{\mathtt{n,u}}$	m^2	Cell surface of n-th FIT grid cell in **u** direction
$\mathtt{A}_{\mathtt{n,v}}$	m^2	Cell surface of n-th FIT grid cell in **v** direction
$\mathtt{A}_{\mathtt{n,w}}$	m^2	Cell surface of n-th FIT grid cell in **w** direction
$\mathbf{A}_{\mathrm{full,n}}$	$1/\mathrm{s}^2$	State-Matrix of the n-th full SSM
$\mathtt{A}_{\mathrm{full,n,FIT}}$	$1/\mathrm{s}^2$	State matrix of FIT discretized SSM
$\mathbf{A}_{\mathrm{cme}}$	$1/\mathrm{s}^2$	State matrix of the SSM reduced with a complete eigendecomposition
$\mathbf{A}_{\mathrm{cme,diag}}$	$1/\mathrm{s}^2$	State matrix of the diagonalized SSM reduced with a complete eigendecomposition
$\mathbf{A}_{\mathrm{red,e}}$	$1/\mathrm{s}^2$	State matrix of the SSM reduced with an incomplete eigendecomposition
$\mathbf{A}_{\mathrm{conc}}$	$1/\mathrm{s}^2$	State matrix of the concatenated SSM
$\mathbf{A}_{\mathrm{conc,red}}$	$1/\mathrm{s}^2$	State matrix of the concatenated, reduced SSM
$\mathbf{A}_{\mathrm{s}}$	$1/\mathrm{s}^2$	State matrix of the scattering formulation SSM
$\mathbf{A}_{\mathrm{b}}$	$1/\mathrm{s}^2$	Block diagonal system matrix of cocatenated SSM
$\mathbf{b}_{\mathrm{ext}}(t)$	$\sqrt{\mathrm{V\,A}}$	Normalized, scattered wave-amplitude
$\mathbf{B}_{\mathrm{full,n}}$	$\sqrt{\mathrm{V}}/\sqrt{\mathrm{A\,s}}$	Input matrix of the n-th full SSM
$\mathbf{B}(\mathbf{r},t)$	Vs/m^2	Magentic flux density
$\widehat{\widehat{b}}$	Vs	Integral-state magnetic flux density through a surface of a FIT grid
$\mathbf{b}$	Vs/m^2	Sampled-state magnetic flux density on a surface of a FIT grid
b	m	height of rectangular waveguide
$\mathtt{B}_{\mathrm{full,n,FIT}}$	$\sqrt{\mathrm{V}}/\sqrt{\mathrm{A\,s}}$	Input matrix of FIT discretized SSM
$\mathbf{B}_{\mathrm{cme}}$	$\sqrt{\mathrm{V}}/\sqrt{\mathrm{A\,s}}$	Input matrix of the SSM reduced with a complete eigendecomposition
$\mathbf{B}_{\mathrm{cme,diag}}$	$\sqrt{\mathrm{V}}/\sqrt{\mathrm{A\,s}}$	Input matrix of the diagonalized SSM reduced with a complete eigendecomposition

Symbol	Unit	Description
$\mathbf{B}_{\mathrm{red,e}}$	$\sqrt{\mathrm{V}}/\sqrt{\mathrm{A\,s}}$	Input matrix of the SSM reduced with an incomplete eigendecomposition
$\mathbf{B}_{\mathrm{conc}}$	$\sqrt{\mathrm{V}}/\sqrt{\mathrm{A\,s}}$	Input matrix of the concatenated SSM
$\mathbf{B}_{\mathrm{conc,red}}$	$\sqrt{\mathrm{V}}/\sqrt{\mathrm{A\,s}}$	Input matrix of the concatenated, reduced SSM
$\mathbf{B}_{\mathrm{s}}$	$\sqrt{\mathrm{V}}/\sqrt{\mathrm{A\,s}}$	Input matrix of the scattering formulation SSM
$\mathbf{W}_{\mathrm{full}}$	1	Projection Matrix of MOR
$\mathbf{B}_{\mathrm{b}}$	$\sqrt{\mathrm{V}}/\sqrt{\mathrm{A\,s}}$	Block diagonal input matrix of cocatenated SSM
c_0	m/s	Speed of light in vacuum
$\mathtt{C}$	1	Discretized Curl operator on the FIT grid
$\tilde{\mathtt{C}}$	1	Discretized Curl operator on the FIT dual grid
$\mathbf{D}_z$	Ω	Diagonal matrix containing the wave impedances of the corresponding 2D modes
$\mathbf{D}_{\mathrm{s}}$	Vs/A	Feed forward matrix of the scattering formulation SSM
$\mathbf{D}(\mathbf{r},t)$	$\mathrm{As/m^2}$	Electric flux density
$\widehat{\widehat{d}}$	As	Integral-state electric flux density over a surface of a FIT grid
$\mathbf{d}$	$\mathrm{As/m^2}$	Sampled-state electric flux density over a surface of a FIT grid
$\mathtt{D}_A$	$\mathrm{m^2}$	Matrix holding the area of the grid cell-surfaces
$\tilde{\mathtt{D}}_A$	$\mathrm{m^2}$	Matrix holding the are of the dual grid cell-surfaces
$\mathtt{D}_V$	$\mathrm{m^3}$	Matrix holding the volume of the grid cells
$\tilde{\mathtt{D}}_V$	$\mathrm{m^3}$	Matrix holding the volume of the dual grid cells
$\mathtt{D}_S$	m	Matrix holding the length of the grid edges
$\tilde{\mathtt{D}}_S$	m	Matrix holding the length of the dual grid edges
$\bar{\mathbf{E}}\,(\mathbf{r},t)$	$\sqrt{VAs/m^3}$	Normed electric field strength
$\mathbf{E}\,(\mathbf{r},t)$	V/m	Electric field strength
$\widehat{\mathbf{e}}$	V	Integral-state electric voltage over an edge of a FIT grid
$\mathbf{e}$	V/m	Sampled-state electric voltage on an edge of a FIT grid
$\mathbf{E}_n(\mathbf{r})$	V/m	n-th solution of the Helmholtz-equation of the electric field
$\mathbf{E}_\nu(\mathbf{r})$	V/m	ν-th solution of the Helmholtz-equation of the electric field
$\mathbf{E}_{\mathrm{t}}(\mathbf{r}_{\mathrm{t}})$	V/m	Transversal electric field strength
$\mathbf{E}_{\mathrm{t,Prt}}(\mathbf{r}_{\mathrm{t}},t)$	V/m	Transverse electric field inside the port-surface

Symbol	Unit	Description
$\mathbf{E}_{\mathrm{z}}(z)$	V/m	Longitudinal electric field strength
$\mathbf{F}(\mathbf{r},t)$	arb	Arbitrary vector field
$f(\mathbf{r},t)$	arb	Arbitrary scalar function
$\mathbf{F}_{\mathrm{L}}$	$\mathrm{kg\,m/s^2}$	Lorentz force
$\mathbf{F}$	1	Auxiliary matrix to remove linearly dependent states
$\mathtt{G}$		FIT Grid
$\tilde{\mathtt{G}}$		FIT Dual Grid
$G_{\mathrm{tc,n}}(s)$	$1/\Omega$	Wave admittance of the n-th 2D mode
$\mathbf{G}(s)$	$1/\Omega$	Matrix containing the wave admittance of all 2D modes on the diagonal
$\bar{\mathbf{H}}\,(\mathbf{r},t)$	$\sqrt{VAs/m^3}$	Normed magnetic field strength
$\mathbf{h}$	A/m	Sampled-state magnetic field strength on an edge of a FIT grid
$\widehat{\mathbf{h}}$	A	Integral-state magnetic field over an edge of a FIT dual grid
$\mathbf{h}$	A/m	Sampled-state magnetic field over an edge of a FIT dual grid
$\mathbf{H}_n(\mathbf{r})$	A/m	n-th solution of the Helmholtz-equation of the magnetic field
$\mathbf{H}_{\mathrm{t,Prt}}(\mathbf{r}_{\mathrm{t}},t)$	A/m	Transverse magnetic field inside the port-surface
$\mathbf{H}(\mathbf{r},t)$	A/m	Magnetic field strength
$\mathbf{I}$	1	Identity matrix
$\mathbf{i}_{\mathrm{can}}(t)$	A	Canonically ordered modal currents
$\mathbf{i}_{\mathrm{sorted}}(t)$	A	Sorted modal currents
$\mathbf{i}_{\mathrm{int}}(t)$	A	Modal currents associated with port surfaces originating from domain decomposition
$\mathbf{i}_{\mathrm{ext}}(t)$	A	Modal currents associated with port surfaces
$\hat{\mathbf{i}}_{\mathrm{int}}(t)$	A	Redundancy free modal currents used in concatenation
$\widehat{\widehat{j}}$	A	Integral-state electric current density over a surface of a FIT grid
$\mathbf{j}$	$\mathrm{A/m^2}$	Sampled-state electric current density over a surface of a FIT grid
$\mathbf{J}(\mathbf{r},t)$	$\mathrm{A/m^2}$	Electric current density
$\mathbf{J}_{\mathrm{imp}}$	$\mathrm{A/m^2}$	Imprinted electric current density
$\mathbf{J}_{\mathrm{Beam}}$	$\mathrm{A/m^2}$	Beam current density

Symbol	Unit	Description
$\mathbf{J}_{\mathrm{Prt},m}(\mathbf{r},t)$	$\mathrm{A/m^2}$	m-th current density in the port surface
$\mathtt{k}_{\mathrm{t,m}}$	1/m	m-th wave number of discretized Helmholtz equation
k	1/m	Angular wavenumber
k_n	1/m	n-th angular wavenumber
$\mathbf{K}$	1	Auxiliary matrix to remove internal states
$\mathtt{L}_{\mathrm{t,m}}(\mathbf{r}_{\mathrm{t}})$	1/m	Discretized 2D field distributions in portsurfaces
$\mathtt{L}_{\mathtt{n,u}}$	m	Edge length in $\mathbf{u}$ direction of n-th FIT grid
$\mathtt{L}_{\mathtt{n,v}}$	m	Edge length in $\mathbf{v}$ direction of n-th FIT grid
$\mathtt{L}_{\mathtt{n,w}}$	m	Edge length in $\mathbf{w}$ direction of n-th FIT grid
$\mathbf{L}_{\mathrm{t,m}}(\mathbf{r}_{\mathrm{t}})$	$\mathrm{1/m^2}$	2D field distributions in Portsurfaces
$\mathbf{M}_{\mathrm{full,n}}$		n-th non reduced SSM
$\mathbf{M}_{\mathrm{red,n}}$		n-th non reduced SSM
$\mathbf{M}_{\mathrm{conc}}$		Concatenated, non-reduced model
$\mathbf{M}_{\mathrm{conc,red}}$		Concatenated reduced model
$\mathtt{M}_{\epsilon}$	As/V	Matrix mapping the electric grid voltages to electric grid fluxes
$\mathbf{M}$	1	Nullspace of $\mathbf{F}^{\mathrm{T}}\bar{\mathbf{B}}_{\mathrm{b},1}^{\mathrm{T}}$ matrix
M_{2D}	1	Number of 2D modes in port-surface
N_{seg}	1	Number of segments for SSC domain decomposition
N_{DOF}	1	Number of DOFs for 3D FIT Discretization
N_{seg}	1	Number of segments for decomposition
$\mathbf{n}$	1	Arbitrary normal vector
$\mathbf{n}_{\partial\mathbf{\Gamma}_{\mathrm{Prt}}}$	1	Vector normal to the boundary of the waveguide port surface
N_{3D}	1	Number of 3D Modes for Eigenexpansion
$\mathtt{N_G}$	1	n-th FIT Grid Node
p	1	Order of vector ansatzfunctions for FEM discretization
$\mathbf{P}_{\mathrm{s}}$	1	Permutation matrix used for permuting states in SSM
$\mathbf{P}$	1	Auxiliary matrix for assembly of the NLEVP
$p_{\mathrm{loss}}(\mathbf{r},t)$	$\mathrm{VA/m^3}$	Loss density
$P_{\mathrm{int}}(t)$	VA	Losses inside a domain
$P_{\mathrm{ext}}(t)$	VA	Losses outside a domain
$\mathtt{P}$	1	Auxiliary matrix for assembly of the FIT matrices

Symbol	Unit	Description
$P_{\mathrm{loss},n}$	VA	Losses of n-th mode
q	As	Electric charge
$\mathbf{Q}$	arb	Square matrix with the rows being the eigenvectors of an arbitrary matrix
$\mathbf{Q}_{\mathrm{inc}}$	arb	Square matrix with the rows being the first few eigenvectors of an arbitrary matrix
Q_n	1	Quality factor of n-th mode
$Q_{\mathrm{surf,n}}$	1	Quality factor of surface losses of n-th mode
$Q_{\mathrm{mat,n}}$	1	Quality factor of material losses of n-th mode
$Q_{\mathrm{ext,n}}$	1	External quality factor of n-th mode
$\mathbf{R}$	arb	Matrix containing the right singular vectors of the SVD of an arbitrary matrix
$(r/Q)_n$	Ω	R over Q of n-th mode
$\tilde{\mathtt{S}}$	1	Discretized divergence operator of the dual grid
$\mathtt{S}$	1	Discretized divergence operator of the grid
$\mathbf{S}(\mathbf{r},t)$	VA/m^2	Poynting vector
$\mathbf{T}(\lambda)$	1	Auxiliary matrix for NLEVP
$\mathbf{U}$	arb	Matrix containing the left singular vectors of the SVD of an arbitrary matrix
$\mathbf{u}_{i,j}$	$\sqrt{\mathrm{VAs}}$	j-th search direction in search for the i-th eigenvector of the NLEVP
$\mathbf{v}$	m/s	Velocity of charged particle
$\mathbf{v}_{\mathrm{can}}(t)$	V	Canonically ordered modal voltages
$\mathbf{v}_{\mathrm{sorted}}(t)$	V	Sorted modal voltages
$\mathbf{v}_{\mathrm{int}}(t)$	V	Modal voltages associated with port surfaces originating from domain decomposition
$\mathbf{v}_{\mathrm{ext}}(t)$	V	Modal voltages associated with port surfaces
$V_{\mathrm{Particle},n}$	V	Effective voltage acting on a particle
$\mathtt{V_n}$	1/m^3	Cell volume of n-th FIT grid Cell
$\mathbf{v}^{\mathrm{H}}$	1	Normalization vector for the eigenvectors of the NLEVP
$\mathbf{W}_{\mathrm{conc}}$	1	Projection matrix of the MOR of the concatenated system
$\mathbf{W}_{\mathrm{full,n}}$	1	Projection matrix for the MOR of the n-th domain
$w_{\mathrm{e}}(\mathbf{r},t)$	VAs/m^3	Energy density of the electric field
$w_{\mathrm{m}}(\mathbf{r},t)$	VAs/m^3	Energy density of the magnetic field
$W_{\mathrm{e}}(\mathbf{r},t)$	VAs	Energy of the electric field

Symbol	Unit	Description
$W_{\mathrm{m}}(\mathbf{r}, t)$	VAs	Energy of the magnetic field
$\mathbf{x}_{\mathrm{full,n}}$	$\sqrt{\mathrm{VAs}}$	State vector of the n-th full SSM
$\mathbf{x}_{\mathrm{full,n,FIT}}$		State vector of FIT discretized SSM
$\mathbf{x}_{\mathrm{red}}$	$\sqrt{\mathrm{VAs}}$	
$\mathbf{X}_{\mathrm{inc}}$	$\sqrt{\mathrm{VAs}}$	
$\mathbf{x}_{\mathrm{sn},i}$	$\sqrt{\mathrm{VAs}}$	System response of the Fourier-transformed, non-reduced SSM at the i-th port
$\mathbf{X}_{\mathrm{sn}}$	$\sqrt{\mathrm{VAs}}$	System response of the Fourier-transformed, non-reduced SSM
$\mathbf{x}_{\mathrm{cme}}(t)$	$\sqrt{\mathrm{VAs}}$	State vector of the SSM reduced with a complete eigendecomposition
$\mathbf{x}_{\mathrm{red,e}}$	$\sqrt{\mathrm{VAs}}$	State vector of the SSM reduced with an incomplete eigendecomposition
$\mathbf{x}_{\mathrm{cme,diag}}(t)$	$\sqrt{\mathrm{VAs}}$	State vector of the diagonalized SSM reduced with an incomplete eigendecomposition
$\mathbf{x}_{\mathrm{conc}}(t)$	$\sqrt{\mathrm{VAs}}$	State vector of concatenated SSM
$\mathbf{x}_{\mathrm{conc,red}}(t)$	$\sqrt{\mathrm{VAs}}$	State vector of concatenated and reduced SSM
$\mathbf{x}_{\mathrm{s}}$	$\sqrt{\mathrm{VAs}}$	State vector of the scattering formulation SSM
$\mathbf{x}_{i,0}$	$\sqrt{\mathrm{VAs}}$	Initial guess for i-th eigenvector of the NLEVP
$\mathbf{x}_{\mathrm{i,j}}$	$\sqrt{\mathrm{VAs}}$	j-th Approximation of the i-th eigenvector of the NLEVP
Z_0	Ω	Free space wave impedance
$Z_m(j\omega)$	Ω	m-th Wave impedance
$Z_{\mathrm{TE},n}$	Ω	Wave impedance of n-th 2D TE mode
$Z_{\mathrm{TEM},n}$	Ω	Wave impedance of n-th 2D TEM mode
$Z_{\mathrm{TM},n}$	Ω	Wave impedance of n-th 2D TM mode
$Z_{\mathrm{Line,n}}$	Ω	Line impedance of n-th 2D mode
ε	As/(Vm)	Permittivity
ε_0	As/(Vm)	Permittivity of free space
ε_r	1	Relative permittivity
$\nabla\times$	1/m	Curl operator
$\underline{\gamma}_m(j\omega)$	1/m	Complex propagation constant of mth waveguide mode
$\delta(z)$	1/m	Dirac distribution
$\delta_{\nu,\mathrm{n}}$	1	Kronecker Delta
Δ	$1/\mathrm{m}^2$	Laplace operator
Δ_t	$1/\mathrm{m}^2$	Transverse Laplace operator

Symbol	Unit	Description
$\mathbf{0}$	1	Zero Vector
$\hat{\hat{\hat{\rho}}}$	As	Integral-state electric charge density over a volume of a FIT grid
ρ	$\mathrm{As/m^3}$	Sampled-state electric charge density over a volume of a FIT grid
μ	Vs/(Am)	Permeability
μ_0	Vs/(Am)	Permeability of free space
μ_r	1	Relative permeability
$\rho(\mathbf{r}, t)$	$\mathrm{As/m^3}$	Electric charge density
σ	A/(Vm)	Electric conductivity
$\omega_{c0,m}$	1/s	Angular cutoff wavenumber of mth waveguide mode
$\mathbf{\Omega}$		Computational Domain
$\nabla\cdot$	1/m	Divergence operator
$\nabla_t\cdot$	1/m	Transverse divergence operator
∇	1/m	Gradient operator
κ	A/(Vm)	Electrical conductivity
λ	m	Wavelength
λ_n	1	n-th eigenvalue of the NLEVP
$\lambda_{i,j}$	1	j-th approximation of the i-th eigenvalue of the NLEVP
$\lambda_{i,0}$	1	Initial guess for the i-th eigenvalue of the NLEVP
λ_n	m	n-th wavelength
$\mathbf{\Gamma}_{\mathrm{Prt}}$	1	Surface of Waveguide Port
$\partial\mathbf{\Gamma}_{\mathrm{Prt}}$	1	Boundary of waveguide port surface
$\mathbf{\Lambda}$	arb	Square matrix with the diagonal containing the eigenvalues of an arbitrary matrix
$\mathbf{\Sigma}$	arb	Matrix containing the singular values of the SVD of an arbitrary matrix on the diagonal

1 Introduction and Objectives

Superconducting radio-frequency (SRF) resonators are a key component to many scientific and industrial applications in accelerator physics [1]. The design and operation of such structures requires an in-depth knowledge of the electromagnetic fields inside these structures. Furthermore, in order to find an optimum of operational costs and performance, the electromagnetic losses during the operation have to be precisely evaluated and improved accordingly. Said losses are drastically influencing the costs of the entire operation and limit (for SRF structures) certain developments, especially for high beam currents [2] or high repetition rates. Among many influential parameters like chemical treatment, operational temperature, choice of Niobium alloys [3], [4] an important parameter is the shape of the accelerating structure. The shape is optimized using cutting edge computational applications which solve Maxwell's equations numerically inside said domain. However, these commonly used tools have several shortcomings, especially when dealing with large and complex structures which need many degrees of freedom (DOF) to be accurately represented. This thesis addresses some of these shortcomings and outlines improved solutions which allow for a more accurate design of said accelerating shapes in an effort to make a contribution to modern accelerator physics and improve future particle accelerators.

In order to accomplish the latter mentioned goals, the biggest problem regards the computationally disadvantageous scaling behavior of the investigated problems. To further explain this: The sought solutions are harder and harder to obtain with a sufficient accuracy, the larger and more complex the structure is. While the described approaches are no problem for comparably small structures, the scaling behavior limits further research of complex structures. One commonly used solution approach is, to simply scale the computational infrastructure and parallelize the numerical evaluation of the problem as in [5], [6] (to name only a few). In most cases the hardware consists of a cluster of high performance computers. While this approach works in practice and pushes the boundaries of feasible investigations, such computational infrastructure is rarely available[1], comparably expensive and takes specific knowledge and manpower to operate. The second commonly applied method to tackle the scaling behavior of electromagnetic simulations is a simplification of the structure. In this case only a fracture of the structure is taken into account which might be justified in some cases since the structure is highly repetitive. However, when taking the entire structure into account there might be additional effects, like

[1] As an example, the methods proposed in [5] are solely available to researchers employed by the US Department of Energy and their project-partners.

modes propagating through the entire structure, that can not be accounted for.

Therefore, in this thesis it is proposed to close this gap by using methods which reduce the computational demand of the problem by several orders of magnitude, thus allowing its evaluation of standard workstation computers. Firstly, it is important to find a compact mathematical description of electromagnetic fields in arbitrary resonators. Such a description was recently proposed with the State-Space Concatenation (SSC) scheme by T. Flisgen in [7],[8] which gives an excellent foundation to tackle the problems in this thesis.

To address these issues, on the theoretical basis of SSC, methods and/or software for the accurate, numerical investigation of electromagnetic fields in comparably complex collocations of several SRF cavities are developed. Of special interest in this thesis is the efficient evaluation of external losses of said fields on commonly available hardware which, to the authors best knowledge is a currently unsolved problem in accelerator physics. Furthermore, certain effects that occur when dealing with complex, multi-cavity structures are investigated and compared to approaches where the structure is simplified, using the developed tools. As final result, some real-life structures are investigated using the proposed algorithms, trying to show their performance and partly compare them to measurements.

1.1 Particle Accelerators for High-Energy Physics and Superconducting Radio-Frequency Resonators

This thesis deals mainly with topics related to accelerator physics[2]. Therefore a short introduction into the uses and applications of accelerator physics is given in this section.

The usage of high-energy photon or charged particle beams is advantageous due to their superior resolution compared to that of e.g. visible light [9]. Hence, beginning roughly 100 years ago, particle beams have been used directly or indirectly, by generation of synchrotron radiation, to investigate matter [10],[9]. Currently there are roughly 24,000 particle accelerators in industrial use and roughly 11,000 in medical use worldwide [11]. The publicly most known accelerators which are being used for high energy physics like the Large Hadron Collider (LHC) only make a fraction of the total numbers, especially due to their high costs.

A particle accelerator interacts with charged particles using electromagnetic fields in order to accelerate the particles to relativistic velocities and high energies. Generally, there are two main applications: The generation of particle beams e.g. for collision

[2]Though nearly all outcomes of it could be useful to other branches of science that deal with electromagnetic waves in highly resonant systems.

with another beam or a target on the one hand, and the generation of synchrotron radiation on the other hand [9]. For both approaches, the accelerated particles have to have a comparably high kinetic energy (depending on the specific application) which is achieved by an acceleration towards velocities close to the speed of light in vacuum c_0. In modern particle accelerators, the acceleration employs time-varying electric fields in the radio-frequency range[3] in order to transfer energy to the particles due to the superior resistivity to any kind of breakdown, thus increasing the possible energy gain compared to accelerators that use static-electric fields [9]. The basic idea is to have a time-varying electric field that resonates in phase with the moving charged particles. This is highlighted in Fig. 1.1, showing the accelerating electric field on the beam-axis and the direction of the Lorentz-force $\mathbf{F}_\mathrm{L}$ for a positively charged particle with the velocity $\mathbf{v}$ close to the speed of light[4]. In the upper part of Fig. 1.1 the particle traverses the first cell, experiencing a Lorentz-force in its direction of motion. While the particle moves to the next cell, the phase of the electric field changes. By design the phase has changed by 180° when the particle reaches the center of the next cell, resulting again in a Lorentz-force in its initial direction of motion as highlighted by the lower part of Fig. 1.1. This way, the particle (if injected at the correct phase) encounters roughly the same force in all cells, leading to a accumulating effect of the acceleration. Due to the phase change of 180° from cell to cell, this specific electric field is generally denoted as the π-mode. All modes with resonance frequencies higher than that of the π-mode are denoted as higher order modes (HOM). These HOM's are generally unwanted and can be excited by traversing charged particles and might reduce the quality of the beam and increase the cryogenic losses.

For a cost-effective accelerating structure, one design goal is to achieve a comparably high energy-gain per unit length. The applied electric field is commonly in the range of several MV/m[5]. A driving factor for increasing the possible energy gain per unit length while reducing the electromagnetic losses is the decision to use superconducting materials instead of copper [3]. Therefore, the cavities are fabricated from Niobium (or Niobium alloys like Niobium-Tin [4]) and cooled down by a cryogenic infrastructure using liquid helium to 2 K, or 4 K, depending on the application. At such low temperatures Niobium is superconducting and has (depending on the purity of the Niobium and certain fabrication steps) a surface resistivity of several nΩ, which is several orders of magnitude lower than copper. These low losses lead to large intrinsic quality factors of the fabricated cavities above 10^{10}, which are some of the highest observable quality factors in physics [3]. Said cavities are further denoted as SRF cavities, with a typical example shown in Fig. 1.2.

[3] Several MHz up to 300 GHz.

[4] In this thesis all vectors and matrices are highlighted with a bold font.

[5] There are certain ways to overcome these limits up to several GV/m using either plasma-wakefield acceleration or miniature dielectric structures. These techniques are not discussed in this thesis.

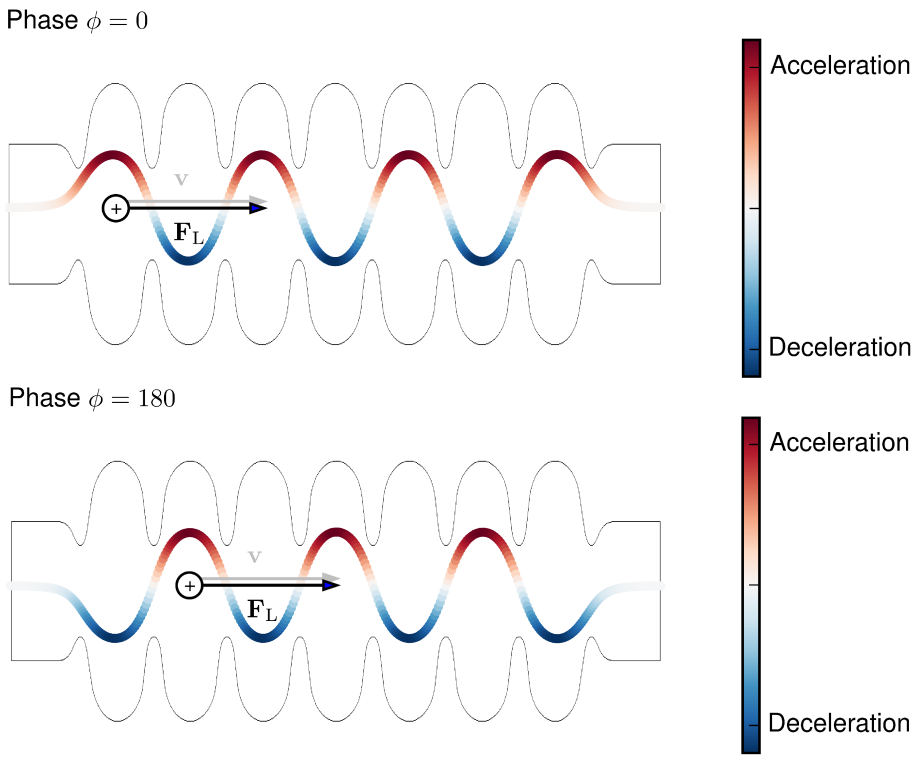

Abbildung 1.1: This picture shows a qualitative plot of the acceleration principle in SRF cavities. It is shown how a single, positively charged particle (highlighted in black) traverses through the cavity with an initial velocity $\mathbf{v}$. Furthermore, the longitudinal electric field of the π-mode on the beam axis and the resulting force $\mathbf{F}_\mathrm{L}$ acting on the particle are shown. The force $\mathbf{F}_\mathrm{L}$ is the later introduced Lorentz-force. If the particle is injected with the correct phase regarding the π-mode, a Lorentz-force in its initial direction of motion is generated in each cell, leading to an increased kinetic energy of the particle. It should be noted that the electric field on axis and the resonator do not share the same axis.

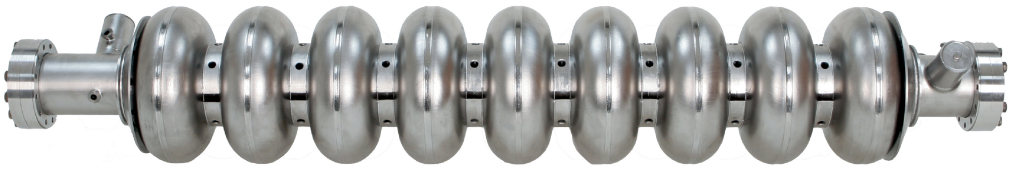

Abbildung 1.2: This picture shows a typical SRF cavity, fabricated from Niobium. The resonator is generally evacuated and operated at 2 K [12]. It consists of nine cells and two couplers to the left and right. These so-called HOM couplers are used to damp parasitic electromagnetic resonances. Furthermore, every resonator has a power or input coupler, through which the π-mode is excited.

Generally many parameters of the cavity like the geometry are chosen according to the relative initial speed of the particles regarding c_0[6]. For medium to high-β cavities the most common geometries are constructed by mean of ellipses and their tangents, leading to so-called elliptical cavities as e.g. in [13]. The cavity then consists of several similar cells, the so-called mid-cells, which are welded together[7]. The cells at both ends, the so-called end-cells, generally have a different geometry to guarantee an optimized damping of unwanted electromagnetic fields. In this thesis the focus is laid on elliptical, high-β cavities, though the introduced formalisms are applicable to all kind of resonators used in SRF technology.

In order to excite the accelerating electromagnetic field, an RF-coupler, connected to a klystron is placed in the vicinity the cavity. This coupler is denoted as the *input coupler*. Furthermore, more couplers are introduced through which the unwanted HOM's are able to propagate out of the system. This coupler is denoted as *HOM coupler*.

1.2 Problem Statement

This section outlines the specific problems this thesis addresses. These problems are later explained in more detail. The numerical simulation of SRF resonators is a computationally challenging task. By design, several similar SRF resonators are concatenated to one accelerating chain whose electromagnetic fields can couple to each other. Since gaining experimental data can be very expensive (due to complexity and operational costs of the structures), the experiments regarding the electromagnetic fields are in many cases conducted using numerical techniques. In most literature investigating SRF cavities, the structure is confined to one single cavity with its couplers attached. Unfortunately, while some fields are confined in one cavity, the majority of HOM energy is stored in electromagnetic fields which are not necessarily confined in one cavity [3] and whose fields can fill the entire structure as shown e.g. in Fig. 1.3. Due to the immense computational demand on computing such fields, an efficient implementation and automation of an appropriate method to enable such computations is desirable. Furthermore, it has to be evaluated in which cases the computation of the fields inside the entire domain is necessary and in which cases it is sufficient to confine the computational domain to just one cavity.

From the resonances of the structure, it is generally tried to make some assessments about their losses. The mathematical formulation leads to a comparably large *nonlinear eigenvalue problem* (NLEVP). While this problem is solved for small

[6] A possible differentiation regarding the cavities is done using the velocity of the particles compared to the vacuum speed of light $\beta = v_z/c_0$. It is differentiated between low-β as $\beta < 0.4$, medium-β as $0.4 < \beta < 0.8$ and high-β as $0.8 < \beta$ cavities [3].

[7] The maximum number of cells is determined by many parameters like cleaning or trapped electromagnetic fields. Generally there exist hardly any cavities with more then nine cells.

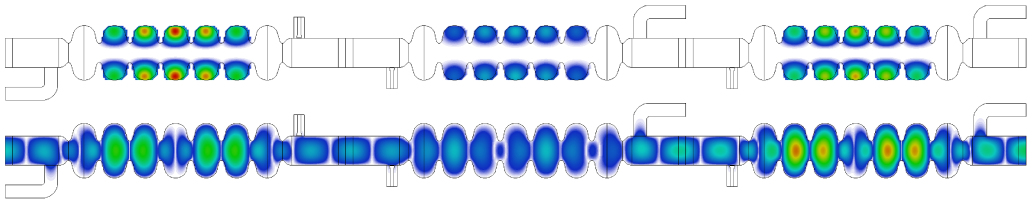

Abbildung 1.3: In this picture the absolute value of the electric fields of two types of eigenmodes are shown for the bERLinPro accelerator. The upper picture shows a mode resonating at 3.6807 GHz which is well confined in the cavities. Such a mode hardly changes its field pattern when several cavities are connected. The lower picture shows a mode resonating at 1.8564 GHz which is able to resonate in the entire structure. Computing these kinds of modes as well as making assessments about their losses is a central element of this thesis which is further discussed in Chapter 5.

structures with few DOFs needed for a sufficiently accurate determination, the efficient computation of lossy resonances in complex SRF structures is an unsolved problem for fairly large structures. Therefore, in this thesis a theoretical solution that enables the computation of the most relevant losses for large-scale resonators was aimed for.

1.3 Structure and Novel Scientific Contributions of the Thesis

This thesis is structured as follows: In the consecutive chapters, first in Chapter 2, an introduction to the foundations of electromagnetic field theory is given by Maxwell's equations as well as some special considerations when dealing with electromagnetic fields in the vicinity of conducting structures. A special focus is laid upon the computation of electromagnetic fields in SRF cavities as well as relevant, secondary quantities derived from the computed fields which are of special interest for applications based in accelerator physics. Furthermore, the numerical discretization of Maxwell's equations using the Finite Integration Technique and the approximation of second order partial differential equations using systems of ordinary differential equations is briefly introduced. Chapter 3 deals with the state-space concatenation scheme, a domain-decomposition scheme that was used throughout this thesis to reduce the numerical effort for solving Maxwell's equations. The theoretical derivation, as well as the conducted implementation and automation of SSC are explained in detail. Furthermore, an analytical example is shown and compared to SSC, and the method is theoretically compared to other, existing domain decomposition schemes. Chapter 4 deals with the accurate computation of external losses with the help of SSC. The resulting NLEVP is discussed with its properties and solution approaches. The solutions are evaluated with a small numerical example of a simplified resona-

tor as well as a real-life cavity. The proposed solution approach is further checked for physical validity and partly compared to available measurements. In Chapter 5 the previously developed and described techniques are used to describe effects that occur when computing multi-cavity accelerating structures, on the example of two relatively simple SRF cavities. Furthermore, some real-life examples that show the application of the developed methods to accelerating structures are discussed, namely the FLASH Third Harmonic Module, the bERLinPro main linac and the BESSY$^{\text{VSR}}$ SRF cavities. The results from one application are further compared to measurements conducted by other researchers. The final chapter comprises the shown scientific contributions in this thesis and discusses some ideas about further applications and developments regarding the topics discussed in this thesis.

Some minor explanations that did not fit naturally into the thesis are explained in the appendix which is referenced at the appropriate chapters.

To the author's best knowledge this thesis contains several new scientific contributions to the fields of RF-engineering, applied mathematics and accelerator physics. Some of these contributions were published in [14] and [15] in preparation of this thesis. The novelty of this thesis consists of three main different contributions

1. The automation of the state-space concatenation scheme. SSC was mentioned in earlier research [7], however, in order to avoid errors and heavily improve the performance and usability, the algorithm had to be effectively implemented and automated for arbitrary topologies of waveguides.

2. The formal derivation of the nonlinear eigenvalue problem resulting from the computation of external losses as well as its combination with model-order reduction and the effective solution for large numbers of solutions.

3. The investigation of electromagnetic fields in complex, multi-cavity structures using the latter mentioned implemented tools and their application to three real-life projects from accelerator physics to answer important scientific questions like certain design choices or the identification of possibly dangerous modes.

These new contributions are discussed in the Chapters 3 and 4 and are applied in Chapter 5.

2 Electromagnetic Field Theory

For the investigation of RF structures the computation of the arising electromagnetic fields is inevitable. These fields are solutions of the well known Maxwell's equations, which are reprised in this chapter. Furthermore, some basic derivations about the behavior of guided electromagnetic waves are discussed. Finally it is shown how these equations are discretized using state of the art schemes i.e. the Finite Integration Technique (FIT). It should be noted that not a complete survey is given, but rather an incomplete introduction to the basic concepts used throughout this thesis. Readers with a deep knowledge in electromagnetic field theory are free to skip this chapter.

2.1 Maxwell's Equations

In the middle of the 19th century, the Scottish mathematician James Clerk Maxwell published a set of equations trying to mathematically outline preceded physical experiments about electromagnetic phenomena [16]. While in the original notation, hyper complex numbers[1] were used, the formulation was later simplified by Oliver Heaviside using vector calculus [17]. The produced set of four partial differential equations comprises a classical electromagnetic field theory describing the interaction of electric fields $\mathbf{E}(\mathbf{r},t)$ and magnetic fields $\mathbf{H}(\mathbf{r},t)$ with matter and vacuum through field equations [18]. The spatial dependency of the introduced quantities is depicted with $\mathbf{r}$ and the time dependency with t. These equations are today known as Maxwell's equations and are most commonly used in the notation

$$\oint_{\partial\mathbf{\Gamma}} \mathbf{H}(\mathbf{r},t)\cdot \mathrm{d}\mathbf{s} = \iint_{\mathbf{\Gamma}} \left(\mathbf{J}(\mathbf{r},t) + \frac{\partial}{\partial t}\mathbf{D}(\mathbf{r},t)\right)\cdot \mathrm{d}\mathbf{A}, \tag{2.1}$$

$$\oint_{\partial\mathbf{\Gamma}} \mathbf{E}(\mathbf{r},t)\cdot \mathrm{d}\mathbf{s} = -\iint_{\mathbf{\Gamma}} \frac{\partial}{\partial t}\mathbf{B}(\mathbf{r},t)\cdot \mathrm{d}\mathbf{A}, \tag{2.2}$$

$$\oiint_{\partial\mathbf{\Omega}} \mathbf{D}(\mathbf{r},t)\cdot \mathrm{d}\mathbf{A} = \iiint_{\mathbf{\Omega}} \rho(\mathbf{r},t)\,\mathrm{dV}, \tag{2.3}$$

$$\oiint_{\partial\mathbf{\Omega}} \mathbf{B}(\mathbf{r},t)\cdot \mathrm{d}\mathbf{A} = 0, \tag{2.4}$$

with the *electric charge density* $\rho(\mathbf{r},t)$, the *electric current density* $\mathbf{J}(\mathbf{r},t)$, the *electric flux density* $\mathbf{D}(\mathbf{r},t)$ and the *magnetic flux density* $\mathbf{B}(\mathbf{r},t)$. The equation (2.1)

[1] In Maxwell's case quaternions were used.

is known as generalized Ampère's circuital law. It describes how the integral over an arbitrary closed curve $\partial\mathbf{\Gamma}$ equals the integral of the current density and the derivative with respect to time of the electric flux density over the surface $\mathbf{\Gamma}$ enclosed by said line. The equation (2.2) denotes the *induction law* and describes that the integral of a closed curve $\partial\mathbf{\Gamma}$ equals the integral over the derivative with respect to time of the magnetic flux density over the surface $\mathbf{\Gamma}$ enclosed by the curve. Furthermore, *Gauss's law* (2.3) describes that the integral over a closed surface of an arbitrary volume $\partial\mathbf{\Omega}$ of the electric flux density equals the integral of the electric charge density over the same volume $\mathbf{\Omega}$. The last Maxwell equation (2.4), *Gauss's law of magnetism* states that the integral over any arbitrary closed surface $\partial\mathbf{\Omega}$ of the magnetic flux density is zero.

For a full description of the fields, interaction with matter has to be described. Therefore, in Maxwell's equations auxiliary vector-quantities, namely the flux densities of the electric and magnetic field were introduced

$$\mathbf{B}(\mathbf{r},t) = \underbrace{\mu_0\,\mu_r}_{\mu}\mathbf{H}(\mathbf{r},t), \tag{2.5}$$

$$\mathbf{D}(\mathbf{r},t) = \underbrace{\varepsilon_0\,\varepsilon_r}_{\varepsilon}\mathbf{E}\left(\mathbf{r},t\right), \tag{2.6}$$

with the material-specific, *magnetic permeability* μ and *electric permittivity* ε. The magnetic permeability is the product of the *vacuum permeability* μ_0 and the *relative permeability* μ_r which is a specific material property. For the electric permittivity it holds, that it is the product of the *vacuum permittivity* ε_0 and the *relative permittivity* ε_r, which is a specific material property[2].

The electric current density $\mathbf{J}(\mathbf{r},t)$ is generally modeled by a superposition of three effects as

$$\mathbf{J}(\mathbf{r},t) = \mathbf{J}_{\mathrm{imp}}(\mathbf{r},t) + \underbrace{\mathbf{v}(\mathbf{r},t)\rho(\mathbf{r},t)}_{\mathbf{J}_{\mathrm{Beam}}} + \underbrace{\kappa\mathbf{E}\left(\mathbf{r},t\right)}_{\mathbf{J}_{\kappa}}, \tag{2.7}$$

with the externally imprinted excitation current $\mathbf{J}_{\mathrm{imp}}$, the current density of a charged particle beam $\mathbf{J}_{\mathrm{Beam}}$ traversing with the velocity $\mathbf{v}(\mathbf{r},t)$ and the *ohmic current density* due to the interaction of the electric field with electrically conducting matter. The so-called ohmic current density $\mathbf{J}_{\kappa}$ is proportional to the conductivity κ of the matter for a given electric field strength.

[2]The equations (2.5) and (2.6) assume that the media are homogeneous, isotropic, linear and respond to electric/magnetics fields without temporal delay. These assumptions are made throughout this entire thesis and hold for all shown applications with sufficient accuracy.

The set of the four equations (2.1)-(2.4) together with the material equations (2.5)-(2.6) and the equation (2.7) for the electric current form the basics of electrodynamics and give a macroscopic, mathematical description of electromagnetic effects in vacuum and matter[3]. In some cases, one is not interested in an integral statement, but rather in differential ones. In this case the *Stokes theorem* [20] can be used to transform (2.1) and (2.2) into their differential form

$$\nabla \times \mathbf{H}(\mathbf{r},t) = \mathbf{J}(\mathbf{r},t) + \frac{\partial}{\partial t}\mathbf{D}(\mathbf{r},t), \tag{2.8}$$

$$\nabla \times \mathbf{E}\,(\mathbf{r},t) = -\frac{\partial}{\partial t}\mathbf{B}(\mathbf{r},t), \tag{2.9}$$

with ∇ being the *Nabla operator*. The vector-product of the Nabla operator and a field-quantity is further denoted as the *curl* of said field-quantity, describing the *rotation* inside an infinitesimal small domain. The *Gauss's theorem* [20] can be used to transform (2.3) and (2.4) into their differential form

$$\nabla \cdot \mathbf{D}(\mathbf{r},t) = \rho(\mathbf{r},t), \tag{2.10}$$

$$\nabla \cdot \mathbf{B}(\mathbf{r},t) = 0, \tag{2.11}$$

with the dot product of the Nabla operator and a field-quantity being further denoted as the *divergence* of said field-quantity, describing the field-sources inside an infinitesimal small domain.

Furthermore, the force acting on a charged particle with the charge q moving with the velocity $\mathbf{v}$ due to electric and magnetic fields are described by the Lorentz Force $\mathbf{F}_\mathrm{L}$

$$\mathbf{F}_\mathrm{L}(\mathbf{r}) = q\left(\mathbf{E}\,(\mathbf{r},t) + \mathbf{v}(\mathbf{r}) \times \mathbf{B}(\mathbf{r},t)\right). \tag{2.12}$$

The equations (2.1) - (2.12) give a macroscopic, mathematical description of all electromagnetic effects investigated in this thesis.

2.1.1 Conservation of Energy

An important property of Maxwell's equations is the *conservation of energy*. Since the propagation of power in and out of SRF structures is a core topic of this thesis, it will be briefly summarized in this subsection. Therefore, the differential form of the induction law (2.9) is multiplied with the magnetic field strength $\mathbf{H}(\mathbf{r},t)$, the

[3]Macroscopic in the sense that no quantum effects are considered. In this case the quantum electrodynamics, proposed by Richard Feynman is more appropriate [19].

differential form of Ampère's law (2.8) is multiplied with the electric field strength $\mathbf{E}(\mathbf{r},t)$ and the two equations are subtracted from each other leading to

$$\begin{aligned}\mathbf{H}(\mathbf{r},t)\cdot(\nabla\times\mathbf{E}(\mathbf{r},t))-\mathbf{E}(\mathbf{r},t)\cdot(\nabla\times\mathbf{H}(\mathbf{r},t))=\\ -\underbrace{\mathbf{H}(\mathbf{r},t)\cdot\frac{\partial}{\partial t}\mu\mathbf{H}(\mathbf{r},t)}_{\frac{\partial}{\partial t}w_{\mathrm{m}}(\mathbf{r},t)}-\underbrace{\mathbf{E}(\mathbf{r},t)\cdot\frac{\partial}{\partial t}\varepsilon\mathbf{E}(\mathbf{r},t)}_{\frac{\partial}{\partial t}w_{\mathrm{e}}(\mathbf{r},t)}-\underbrace{\mathbf{E}(\mathbf{r},t)\cdot\mathbf{J}(\mathbf{r},t)}_{p_{\mathrm{loss}}(\mathbf{r},t)},\end{aligned}\tag{2.13}$$

with the temporal change of the energy density of the magnetic field $\frac{\partial}{\partial t}w_{\mathrm{m}}(\mathbf{r},t)$ and the temporal change of the energy density of the electric field $\frac{\partial}{\partial t}w_{\mathrm{e}}(\mathbf{r},t)$. Furthermore, the loss-density is defined as $p_{\mathrm{loss}}(\mathbf{r},t)$. The left hand-side of (2.13) can be further simplified using common vector calculus identities[4] leading to

$$p_{\mathrm{loss}}(\mathbf{r},t)+\nabla\cdot\underbrace{(\mathbf{E}(\mathbf{r},t)\times\mathbf{H}(\mathbf{r},t))}_{\mathbf{S}(\mathbf{r},t)}=-\frac{\partial}{\partial t}w_{\mathrm{m}}(\mathbf{r},t)-\frac{\partial}{\partial t}w_{\mathrm{e}}(\mathbf{r},t),\tag{2.14}$$

with the introduction of the *Poynting vector* $\mathbf{S}(\mathbf{r},t)$. Said vector comprises the flow of energy-density for each point in space. For now, equation (2.14) describes energy-densities while in practice, energies, instead of energy-densities are of interest. Hence, (2.14) is integrated over the computational domain and yields under the usage of Gauss's theorem and *Schwarz's theorem*[5] [20]

$$\begin{aligned}\underbrace{\iiint_{\mathbf{\Omega}}p_{\mathrm{loss}}(\mathbf{r},t)\,\mathrm{dV}}_{P_{\mathrm{int}}(t)}+\underbrace{\oiint_{\partial\mathbf{\Omega}}\mathbf{S}(\mathbf{r},t)\cdot\mathrm{d}\mathbf{A}}_{P_{\mathrm{ext}}(t)}=\\ -\frac{\partial}{\partial t}\underbrace{\iiint_{\mathbf{\Omega}}w_{\mathrm{e}}(\mathbf{r},t)\,\mathrm{dV}}_{W_{\mathrm{e}}(t)}-\frac{\partial}{\partial t}\underbrace{\iiint_{\mathbf{\Omega}}w_{\mathrm{m}}(\mathbf{r},t)\,\mathrm{dV}}_{W_{\mathrm{m}}(t)}.\end{aligned}\tag{2.15}$$

In other words, (2.15) states that a change in either the magnetic or electric field energy (right hand-side) i.e. $W_{\mathrm{m}}(t)$ and $W_{\mathrm{e}}(t)$ has to be accompanied by either a loss inside the domain or a flow of energy over the domain surface (left hand-side) such that the energy in the domain $\mathbf{\Omega}$ is conserved. The losses inside the domain $P_{\mathrm{int}}(t)$ are denoted as *internal* losses, caused by dielectric, ohmic or magnetic losses. The flow of energy $P_{\mathrm{ext}}(t)$ over the domain surface, specifically the normal component

[4] It holds that $\mathbf{F}_1(\mathbf{r},t)(\nabla\times\mathbf{F}_2(\mathbf{r},t))-\mathbf{F}_2(\mathbf{r},t)(\nabla\times\mathbf{F}_1(\mathbf{r},t))=\nabla\cdot(\mathbf{F}_1(\mathbf{r},t)\times\mathbf{F}_2(\mathbf{r},t))$[20].

[5] In some literature Schwarz's Theorem is also denoted as *Young's Theorem* or *symmetry of second derivatives*.

of the Poynting vector at the boundary, is further denoted as *external* losses[6]. The computation of such external losses is of special interest in this thesis.

2.1.2 Wave Equation

In RF engineering it is generally more interesting to find a more convenient notation than equations (2.8) - (2.11). When dealing with homogeneous media[7], it is therefore a standard approach to separate those equations, such that they contain only one field quantity. This can be done by taking the curl of equation (2.9). Further, replacing the magnetic flux density on the right-hand-side by equation (2.8) under the usage of Schwarz's theorem and the material relation (2.5), this leads to the well known *curl-curl-equation*

$$\nabla \times \nabla \times \mathbf{E}(\mathbf{r},t) = -\frac{\partial}{\partial t}\mu\left(\mathbf{J}(\mathbf{r},t) + \frac{\partial}{\partial t}\varepsilon\mathbf{E}(\mathbf{r},t)\right). \tag{2.16}$$

The left-hand-side of (2.16) can be simplified using basic vector identities[8], which leads to the *inhomogeneous wave equation of the electric field*

$$\mu\varepsilon\frac{\partial^2}{\partial t^2}\mathbf{E}(\mathbf{r},t) - \Delta\mathbf{E}(\mathbf{r},t) = -\mu\frac{\partial}{\partial t}\mathbf{J}(\mathbf{r},t) - \frac{1}{\varepsilon}\nabla\rho(\mathbf{r},t). \tag{2.17}$$

The vector-operator Δ is further denoted as the Laplace-operator[9]. For the magnetic field, choosing the same approach (i.e. taking the curl of (2.8) and plugging in (2.9)), one can derive the *inhomogeneous wave equation of the magnetic field*

$$\mu\varepsilon\frac{\partial^2}{\partial t^2}\mathbf{H}(\mathbf{r},t) - \Delta\mathbf{H}(\mathbf{r},t) = \nabla \times \mathbf{J}(\mathbf{r},t), \tag{2.18}$$

with the major difference that there are no magnetic charges, hence there is only one excitation term, compared to (2.17). With (2.17) and (2.18), two inhomogeneous, hyperbolic, partial differential vector equations are at hand to describe electromagnetic waves in homogeneous media and vacuum.

2.2 Guided Electromagnetic Waves

Opposing to their behavior in free space, the behavior of electromagnetic waves changes drastically in the vicinity of conducting structures which is discussed in

[6] It should be taken into account that the word *loss* is only correctly used if said term is negative, otherwise, energy flows into the domain, not out of it, assuming the standard usage of d$\mathbf{A}$ as pointing in outward direction relative to the surface.

[7] i.e. $\mu_r \neq f(\mathbf{r},t)$ and $\epsilon_r \neq f(\mathbf{r},t)$. For inhomogeneous media, the wave-equation becomes a so-called *Sturm-Liouville-Problem* [18].

[8] It holds that $\nabla \times \nabla \times \mathbf{F}(\mathbf{r},t) = \nabla(\nabla \cdot \mathbf{F}(\mathbf{r},t)) - \Delta\mathbf{F}(\mathbf{r},t)$[20].

[9] It generally holds that $\nabla \cdot (\nabla\phi) = \Delta\phi$

this section. An electromagnetic wave propagating through the enclosure of such conducting structures is generally referred to as a *guided wave*. For the sake of simplicity a common simplification is the assumption that the electrical conductivity of said structure is infinitely high, hence the surface losses are zero. Such a conductor is denoted as *perfect electric conducting* (PEC). For the electric and magnetic field it holds the boundary condition

$$\mathbf{n} \times \mathbf{E}\,(\mathbf{r}, t) = \mathbf{0} \text{ and } \mathbf{n} \cdot \mathbf{H}(\mathbf{r}, t) = 0 \text{ on } \partial\mathbf{\Omega}, \tag{2.19}$$

with an arbitrary vector $\mathbf{n}$ normal to the surface $\partial\mathbf{\Omega}$. In some cases a *perfect magnetic conducting* material (PMC) is chosen as boundary condition, for which holds

$$\mathbf{n} \cdot \mathbf{E}\,(\mathbf{r}, t) = 0 \text{ and } \mathbf{n} \times \mathbf{H}(\mathbf{r}, t) = \mathbf{0} \text{ on } \partial\mathbf{\Omega}. \tag{2.20}$$

Both boundary conditions (PEC and PMC) do not enable an energy exchange with the vicinity through the boundary surfaces[10].

A further simplification that is assumed in this thesis is that the investigated structures are fully evacuated, meaning that the losses caused by a dielectric or conducting material are neglected for now[11].

2.2.1 The Helmholtz Equation

To compute the occurring resonances, the inhomogeneous wave-equation (2.17) is reformulated by assuming that all currents $\mathbf{J}(\mathbf{r}, t)$ are zero, and that the region is free of electric charges (i.e. the structure is non-excited). Furthermore, due to the losslessness of the resonator, one can assume that all fields are harmonically oscillating or can be decomposed into a finite sum of harmonic oscillations. Under these given assumptions, (2.17) can be transformed into the so-called *Helmholtz-equation for the electric field*

$$\Delta\mathbf{E}_n(\mathbf{r}) + k_n^2\mathbf{E}_n(\mathbf{r}) = \mathbf{0}, \tag{2.21}$$

[10] Generally speaking, for none of the two boundary conditions a negative external energy flow is possible (see 2.15) since for either PEC or PMC one field component is normal, while the other one is tangential to the surface. Therefore, their vector-product (the Poynting-vector) can not in any case show outward of the structure, such that $\mathbf{S}(\mathbf{r}, t) \cdot \mathrm{d}\mathbf{A} = 0$ holds for both cases.

[11] Such materials can remain in the accelerator by accident, e.g. as a residual gas when the structure is evacuated. Since this is not a planned functionality of the structure it is neglected throughout the thesis. Another case would be the purposely introduction of some lossy material into the accelerator which is discussed later. There are actually few applications where the cavities are filled with hydrogen on purpose like [21] to accelerate muons, but this is a rare special case and is not interesting for this thesis.

with the electric field $\mathbf{E}_n(\mathbf{r})$ and wavenumber $k_n = \frac{2\pi}{\lambda_n}$ of the n-th solution. Analogously from (2.18) one can derive the *Helmholtz-equation for the magnetic field*

$$\Delta\mathbf{H}_n(\mathbf{r}) + k_n^2\mathbf{H}_n(\mathbf{r}) = \mathbf{0}. \tag{2.22}$$

The Helmholtz-equations (2.21) and (2.22) generally have infinitely many solution-pairs of angular wavenumber k_n and field-strength $\mathbf{E}_n(\mathbf{r})$. In any following example where a solution of any type of Helmholtz-equation is referenced, it is assumed that the solutions are sorted according to ascending angular wavenumber. For certain geometries it is possible that two or more field-patterns share the same angular wavenumber. These modes are further referred to as *degenerated modes*. It is important to notice that the computed field-strengths are only spatially dependent, but are static in time. The solutions of the Helmholtz-equations are denoted as *eigenmodes*, which are mutually orthogonal

$$\iiint_{\mathbf{\Omega}} \mathbf{E}_\nu(\mathbf{r}) \cdot \mathbf{E}_\mathrm{n}(\mathbf{r})\mathrm{dV} = \delta_{\nu,\mathrm{n}} 2\frac{W_\mathrm{e}}{\varepsilon}, \tag{2.23}$$

as well as for the magnetic field

$$\iiint_{\mathbf{\Omega}} \mathbf{H}_\nu(\mathbf{r}) \cdot \mathbf{H}_\mathrm{n}(\mathbf{r})\mathrm{dV} = \delta_{\nu,\mathrm{n}} 2\frac{W_\mathrm{h}}{\mu}, \tag{2.24}$$

with the Kronecker-delta $\delta_{\nu,\mathrm{n}}$[12]. The orthogonal solutions form a complete set of basis-functions. In lossless, closed cases, the angular wavenumber k_n is real-valued. These solutions of the Helmholtz-equation, can further be used to decompose electric and magnetic fields into weighted, mutually orthogonal fields, when solving the inhomogeneous wave equations (2.17) and (2.18), which is used in many cases throughout this thesis.

Furthermore, if the investigated waveguide does not change its cross section in longitudinal direction, it is possible to decompose the spatially dependent electric field $\mathbf{E}(\mathbf{r})$ (it was earlier assumed that the field is harmonically oscillating in time) into a product of two functions, i.e. $\mathbf{E}(\mathbf{r}) = \mathbf{E}_\mathrm{t}(\mathbf{r}_\mathrm{t}) + \mathbf{E}_\mathrm{z}(z)$. The spatial homogeneity in longitudinal direction of the waveguide allows for the decomposition of the Nabla operator to $\nabla = \nabla_\mathrm{t} + \nabla_\mathrm{z}$, with the transverse Nabla operator ∇_t and the longitudinal Nabla operator ∇_z, and thus the decomposition of the Helmholtz-equations (2.17) and (2.18) into a transversal and a longitudinal part[13] as

$$\Delta_\mathrm{t}\mathbf{E}_{\mathrm{t,n}}(\mathbf{r}_\mathrm{t}) + k_{\mathrm{t,n}}^2\mathbf{E}_{\mathrm{t,n}}(\mathbf{r}_\mathrm{t}) = \mathbf{0}, \tag{2.25}$$

[12] The Kronecker-delta is a function for which holds: $\delta_{ij} = \begin{cases} 0 & \text{if } i \neq j, \\ 1 & \text{if } i = j. \end{cases}$

[13] The decomposition is only explicitly shown for the electric field, but holds for the magnetic field in full analogy.

$$\Delta_{\mathrm{z}}\mathrm{E}_{\mathrm{z,n}}(z) + k_{\mathrm{z,n}}^2\mathrm{E}_{\mathrm{z,n}}(z) = \mathbf{0}. \tag{2.26}$$

The equations (2.25) and (2.26) are coupled by the angular wavenumber, as it holds that $k_{\mathrm{n}}^2 = k_{\mathrm{z,n}}^2 + k_{\mathrm{t,n}}^2$. The separation is interesting because the solution for the transverse Helmholtz-equation (2.25) is the same for both a waveguide that is closed at both longitudinal ends or infinitely long in longitudinal direction, since the transverse domain remains the same for both boundary conditions.

In the investigated waveguide (without change of cross section in longitudinal direction), for every field $\mathbf{E}(\mathbf{r},t)$ and $\mathbf{H}(\mathbf{r},t)$ can be assumed that it can be decomposed as a sum of infinitely many mutually orthogonal functions $\mathbf{E}_{\mathrm{m}}(\mathbf{r},t)$ and $\mathbf{H}_{\mathrm{m}}(\mathbf{r},t)$ as

$$\mathbf{E}(\mathbf{r},t) = \sum_{m=1}^{\infty}\left(\underbrace{\mathbf{L}_{\mathrm{t,m}}(\mathbf{r}_{\mathrm{t}})v_{\mathrm{m}}(z,t)}_{\mathbf{E}_{\mathrm{t,m}}(\mathbf{r},t)} + \mathbf{E}_{\mathrm{z,m}}(\mathbf{r},t)\right), \tag{2.27}$$

$$\mathbf{H}(\mathbf{r},t) = \sum_{m=1}^{\infty}\left(\underbrace{\mathbf{n}_{\mathrm{z}} \times \mathbf{L}_{\mathrm{t,m}}(\mathbf{r}_{\mathrm{t}})i_{\mathrm{m}}(z,t)}_{\mathbf{H}_{\mathrm{t,m}}(\mathbf{r},t)} + \mathbf{H}_{\mathrm{z,m}}(\mathbf{r},t)\right), \tag{2.28}$$

where the field strength of each m-th function is decomposed again into the sum of a purely transversal part and a longitudinal part. The 2D field distributions $\mathbf{L}_{\mathrm{t,m}}(\mathbf{r}_{\mathrm{t}})$ are the solutions of the transverse 2D Helmholtz equation of the electric field (2.25) with a PEC boundary condition and normed with respect to the electric field energy. It holds that

$$\mathbf{L}_{\mathrm{t,m}}(\mathbf{r}_{\mathrm{t}}) = \frac{\mathbf{E}_{\mathrm{t,m}}(\mathbf{r}_{\mathrm{t}})}{\sqrt{W_{\mathrm{e,m}}}}, \tag{2.29}$$

with the electric energy $W_{\mathrm{e,m}}$ of the m-th solution of (2.25). The weighting coefficient of $\mathbf{L}_{\mathrm{t,m}}(\mathbf{r}_{\mathrm{t}})$, $v_{\mathrm{m}}(z,t)$ is further denoted as *modal voltage*, while the weighting coefficient $i_{\mathrm{m}}(z,t)$ in (2.28) is further denoted as *modal current* of their respective 2D modes.

The transverse Helmholtz-equation (2.25) has three different sets of solutions. Firstly, there are solutions for which the longitudinal electric field vanishes. They are further referred to as *transverse electric* (TE) modes, it holds that $\mathrm{E}_{\mathrm{z,m}}(\mathbf{r},t) = 0$. Secondly, there are solutions for which the longitudinal magnetic field vanishes. They are further referred to as *transverse magnetic* (TM) modes, it holds that $\mathrm{H}_{\mathrm{z,m}}(\mathbf{r},t) = 0$. For both cases, TE and TM modes, the angular wavenumber is nonzero and there are generally infinitely many solutions of both types. In the third case, the field has neither an electric, nor a magnetic field strength in longitudinal direction. These solutions are referred to as *transverse electric and magnetic* (TEM) modes, it holds that $\mathrm{E}_{\mathrm{z,m}}(\mathbf{r},t) = 0$ and $\mathrm{H}_{\mathrm{z,m}}(\mathbf{r},t) = 0$. In the TEM case, the angular-wavenumber

is zero and there is a fixed number of solutions equal to the number of electrically disconnected conductors.

2.2.2 Electromagnetic Fields in Closed, Lossless Structures

A standard task in SRF theory, is the determination of the electromagnetic resonances, i.e. the eigenmodes in a closed, non-excited and lossless structure. Though such a case has no direct practical relevance, the concept is useful in that sense, that many applicational cases can be derived from this closed structure. For example the excitation from an antenna, a particle beam or the propagation of energy out of the structure can all be determined by a sum of weighted, lossless resonances.

Therefore, the electric field is decomposed into a set of N_{3D} mutually orthogonal field-patterns $\tilde{\mathbf{E}}_n(\mathbf{r})$ and their time-dependent weighting function $x_n(t)$

$$\mathbf{E}\left(\mathbf{r},t\right) \approx \sum_{n=1}^{N_{3D}} \tilde{\mathbf{E}}_{\mathrm{n}}(\mathbf{r}) x_{\mathrm{n}}(t), \tag{2.30}$$

with $N_{3D} \to \infty$. Historically, the eigendecomposition originates from Fourier-analysis [22]. The solutions $\tilde{\mathbf{E}}_{\mathrm{n}}(\mathbf{r})$ are the solution of the Helmholtz-equation (2.21). The same decomposition can be performed for the magnetic field.

In practice, the Helmholtz-equation (2.21) is often solved numerically by employing a suiting discretization technique. The magnetic field (if needed) is then computed from the Maxwell's equations.

2.2.3 Propagation of Guided, Electromagnetic Waves

Of special interest in RF engineering is the question under which circumstances electromagnetic waves propagate through a waveguide, which is discussed further in this subsection. The equation (2.26) can be solved generally by the sum of two waves that propagate in $+z$ and $-z$ direction as

$$\mathrm{E_z}(z) = \mathrm{E_z^+}(z) e^{j k_{\mathrm{z}} z} + \mathrm{E_z^-}(z) e^{-j k_{\mathrm{z}} z}. \tag{2.31}$$

From (2.31) one can replace the angular wavenumber in z direction with $k_{\mathrm{z}} = \sqrt{k^2 - k_{\mathrm{t}}^2}$.[14] It can be seen that one has to differentiate two cases: Firstly, if the exponent $j k_{\mathrm{z}} z$ is complex-valued (with the imaginary unit j), i.e. if $k > k_{\mathrm{t}}$, the wave is *propagating* in z-direction. Secondly, if the exponent $j k_z z$ is real-valued (and negative), i.e. if $k < k_{\mathrm{t}}$, the wave *decays exponentially* in z-direction. In this case the wave is also referred to as *evanescent*. The wavenumber above which the wave starts

[14] The dedicated reader will notice that there are two possible solutions for the relation $k_{\mathrm{z}} = \sqrt{k^2 - k_{\mathrm{t}}^2}$ (since it is an equation of second degree).

propagating is referred to as the *cutoff wavenumber*. For the n-th cutoff angular frequency $\omega_{\mathrm{c0},n}$ it holds

$$\omega_{\mathrm{c0,n}} = 2\pi f_{\mathrm{c0,n}} = \frac{k_{\mathrm{t,m}}}{\sqrt{\mu\varepsilon}}. \tag{2.32}$$

It should be noted that the cutoff frequency $f_{\mathrm{c0},n}$ depends solely on the transversal shape of the waveguide, i.e. on the solution of the transversal Helmholtz-equation (2.25).

2.2.4 Waveguide Ports

The Sections 2.2.2 and 2.2.3 describe a closed (or infinitely long), lossless waveguide. For application examples one needs to be able to mathematically describe the exchange of energy of that system with its surroundings as in (2.15). This might be an external excitation or the dissipation or propagation of energy out of the system. The problem of an electromagnetically excited waveguide is solved in accelerator physics using a so-called *field equivalence principle*. The basic idea is to replace the problem at hand by an equivalent problem (in that sense that the solution should remain the same in the region of interest), for which the solution is easier to compute. This technique is commonly used for problems where the computational domain can be decomposed into two domains where one domain $\mathbf{\Omega}_1$ contains the sources, and the other $\mathbf{\Omega}_2$ contains the device under test and is sufficiently far away from the sources. The solution of the field-problem is only of relevance in $\mathbf{\Omega}_2$. Therefore, the sources in $\mathbf{\Omega}_1$ are replaced by *virtual sources* on the boundary of $\mathbf{\Omega}_2$ in a way that the resulting field will be the same. In accelerator physics, the cavity is excited by an antenna, relatively far away from the cavity. Therefore, the so-called *Schelkunoff's Field Equivalence Theorem* [23], which originates from *Green's Integral* [18], is applicable[15]. Here the structure is excited by incident (or scattered) electromagnetic waves, originating from space, infinitely far away $\mathbf{\Omega}_1$. These sources are replaced by either magnetic currents (for PEC boundary at the waveguide) or electric currents (for PMC boundary at the waveguide) on the surface of $\mathbf{\Omega}_2$. The common surfaces of $\mathbf{\Omega}_1$ and $\mathbf{\Omega}_2$ are denoted as *waveguide ports* and allow the exchange of energy of the structure with the surroundings. Throughout this thesis, the formulation using electric currents and therefore PMC boundary conditions at the waveguide ports is chosen[16].

In the following an arbitrary waveguide port is described with the surface $\mathbf{\Gamma}_{\mathrm{Prt}}$, a vector $\mathbf{n}_{\mathrm{Prt}}$ normal to said surface, the boundary of the port surface $\partial\mathbf{\Gamma}_{\mathrm{Prt}}$ and a vector normal to the port boundary $\mathbf{n}_{\partial\mathbf{\Gamma}_{\mathrm{Prt}}}$ as highlighted in Fig. 2.1.

[15] This field equivalence principle is a generalization of *Love's Field Equivalence Theorem*.

[16] The choice of electric, virtual currents over magnetic, virtual currents is theoretically exchangeable, however for the tasks at hand in this thesis it is more convenient to use an impedance formulation instead of an admittance formulation.

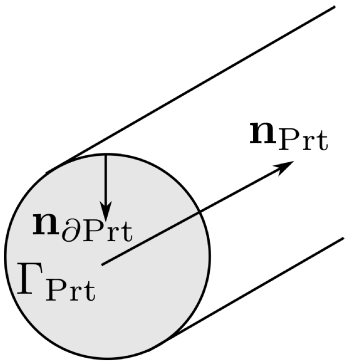

Abbildung 2.1: For arbitrary waveguide ports with the surface $\mathbf{\Gamma}_{\mathrm{Prt}}$, a vector normal to its surface $\mathbf{n}_{\mathrm{Prt}}$ as well as a vector normal to its boundary $\mathbf{n}_{\partial\mathbf{\Gamma}_{\mathrm{Prt}}}$ is defined.

The power $P(t)$ through each waveguide-port can be computed by the transverse (regarding the port surface) electric and magnetic fields inside the port-surface $\mathbf{E}_{\mathrm{t,Prt}}(\mathbf{r}_{\mathrm{t}}, t)$ and $\mathbf{H}_{\mathrm{t,Prt}}(\mathbf{r}_{\mathrm{t}}, t)$ as

$$P(t) = \iint_{\mathbf{\Gamma}_{\mathrm{Prt}}} \mathbf{E}_{\mathrm{t,Prt}}(\mathbf{r}_{\mathrm{t}}, t) \times \mathbf{H}_{\mathrm{t,Prt}}(\mathbf{r}_{\mathrm{t}}, t) \cdot \mathbf{n}_{\mathrm{Prt}} \mathrm{d}\mathbf{A}, \tag{2.33}$$

In a further step, an orthogonal decomposition of all fields inside the port surface is conducted. Therefore, the electric and magnetic fields in (2.33) can be expressed as a weighted superposition of a complete set of orthonormal functions $\mathbf{L}_{\mathrm{t,m}}(\mathbf{r}_{\mathrm{t}})$ which exist solely inside the port-surface and are weighted with time-dependent weighting factors $v_m(t)$ and $i_m(t)$, respectively, as introduced previously in (2.27) and (2.28)

$$\mathbf{E}_{\mathrm{t,Prt}}(\mathbf{r}_t, t) = \sum_{m=1}^{\infty} \mathbf{L}_{\mathrm{t,m}}(\mathbf{r}_{\mathrm{t}})\, v_m(t), \tag{2.34}$$

$$\mathbf{H}_{\mathrm{t,Prt}}(\mathbf{r}_t, t) = \sum_{m=1}^{\infty} \mathbf{n}_{\mathrm{Prt}} \times \mathbf{L}_{\mathrm{t,m}}(\mathbf{r}_{\mathrm{t}})\, i_m(t). \tag{2.35}$$

Plugging the decomposition of the transverse field strengths in (2.34) and (2.35) into (2.33) leads to

$$P(t) = \sum_{m=1}^{\infty} v_m(t) i_m(t). \tag{2.36}$$

Any incident electromagnetic wave from Ω_1, can now be modeled by imprinting a modal current at the port surface $\mathbf{\Gamma}_{\mathrm{Prt}}$, which leads to a transverse magnetic field. These transverse magnetic fields $\mathbf{H}_{t,m}(\mathbf{r}_t, t)$ are chosen according to Schelkunoff's Field Equivalence Theorem as

$$\mathbf{J}_{\mathrm{Prt},m}(\mathbf{r}, t) = \mathbf{n}_z \times \mathbf{H}_{t,m}(\mathbf{r}_t, t)\, \delta(z) = -\mathbf{L}_{\mathrm{t,m}}(\mathbf{r}_{\mathrm{t}}) i_m(t). \tag{2.37}$$

The 2D field patterns $\mathbf{L}_{\mathrm{t,m}}(\mathbf{r}_\mathrm{t})$ are solutions of the Helmholtz-equation (2.25) in the port surface and are zero everywhere else.

2.2.5 Wave Impedances

The complex-valued *electromagnetic wave impedance* is defined as the ratio of the transverse components[17] of electric and magnetic fields of an electromagnetic wave (in frequency domain)

$$Z_m(j\omega) = \frac{\mathbf{E}_{t,m}(\mathbf{r})}{\mathbf{H}_{t,m}(\mathbf{r})} = \frac{v_m(j\omega)}{i_m(j\omega)}. \tag{2.38}$$

The wave impedance is especially interesting when dealing with modal voltages and currents, as introduced in (2.27) and (2.28). The ratio of the m-th modal voltage and current can be described as the wave impedance of the m-th 2D eigenmode. Following [24], the wave impedance depends on the mode type, the frequency (of the wave) and the cutoff frequency. For TM modes it holds that

$$Z_{\mathrm{TM},n} = \mathrm{Z}_0 \frac{\sqrt{(j\omega)^2 + \omega_{co}^2}}{j\omega}, \tag{2.39}$$

with the impedance in free space Z_0 defined as

$$Z_0 = \sqrt{\frac{\mu_0}{\varepsilon_0}}. \tag{2.40}$$

For TE modes it holds that

$$Z_{\mathrm{TE},n} = \mathrm{Z}_0 \frac{j\omega}{\sqrt{(j\omega)^2 + \omega_{co}^2}}. \tag{2.41}$$

For both cases, TE and TM, the wave impedance is real-valued above the cutoff frequency, and complex-valued below the cutoff frequency. In case of TEM modes (where the cutoff frequency is zero), the wave impedance is equal to the free space impedance

$$Z_{\mathrm{TEM},n} = \mathrm{Z}_0. \tag{2.42}$$

The wave impedance can not be given analytically in all cases, for example when losses occur in the 2D port plane. These cases are not considered in this thesis although they are of practical relevance in rare cases [25]. Also for this case, the expansion of the systems energy-coupling in 2D modes might not make sense anymore, since they might not be mutually orthogonal.

[17] In this case transverse refers to the direction which is orthogonal to the waves direction of propagation.

2.2.6 Secondary Quantities for Lossless SRF Cavities

As mentioned earlier, the main topic of this thesis is the computation of electromagnetic fields in RF resonators for particle accelerators. In this context, it is common to compute several *secondary field quantities* from the computed electromagnetic fields. The quantities are commonly used for further computations like estimations of beam instabilities. In the following some standard, secondary quantities are introduced and further explained as shown in [1]. Both quantities try to estimate the behavior of a charged particle bunch in interaction with the earlier computed electromagnetic fields.

The interaction of the particle beam with the electric field of the n-th eigenmode $E_n(x_0, y_0, z)$ is described by the effective voltage acting on a particle $V_{\text{Particle},n}$

$$V_{\text{Particle},n} = \left| \int_0^L E_n(x_0, y_0, z) e^{j\omega_n \frac{z}{c_0}} \, \mathrm{dz} \right|, \tag{2.43}$$

with the length L of the investigated resonator, and the angular frequency of the n-th eigenmode ω_n. This gives a measure of the mean voltage seen by a particle. From this mean voltage, it is advantageous to define a longitudinal, geometric impedance which is material-independent[18]. This measure is further denoted as r/Q and defined by

$$(r/Q)_n = \frac{V^2_{\text{Particle},n}}{\omega_n W_{\text{stored},n}}. \tag{2.44}$$

One usually wants to damp modes for which the product of r/Q and the later introduced external quality factor exceeds a certain value. By design, the mode with the highest r/Q should be the $\pi-$mode.

Another quantity of interest is the estimation of losses in SRF cavities. This is discussed later in this thesis in Chapter 4.

[18] There are many different definitions of r/Q in the literature. In some literature, the oscillation of the electric field is not taken into account as in [3]. Furthermore, it is quite common to define different formulas depending on the indices of a modes multipole expansion (i.e. the formula for r/Q is different for a dipole and a monopole mode). In this thesis the distinction between multipoles is not made for r/Q since the multipole expansion is not possible when dealing with modes that can traverse out of the cavity or through multiple cavities. In theses cases it can happen that several different multipole modes couple and are not distinguishable anymore.

2.3 Discrete Formulation Using the Finite Integration Technique

Maxwell's equations, as described in Chapter 2.1, form a boundary value problem for which it is uniquely determined how the system evolves with respect to time if the boundary conditions and the current state of the system is known. A closed, analytical solution is solely available if one can find a coordinate system that is aligned with the boundary [26], which is rarely possible for arbitrarily shaped real-life applications. Therefore, it is a common practice to employ numerical techniques for the solution of Maxwell's equations. The most commonly applied techniques for electromagnetic fields are the Finite-Element-Method (FEM) [27], Boundary Element Method (BEM), Finite Differences (FD) [27] and the Finite Integration Technique (FIT) [28], [29]. Throughout this thesis FIT, (if not stated explicitly different) was used for the numerical discretization of all shown electromagnetic field problems. Therefore, in this section, a short summary of the technique is presented. Since FIT is not an essential part of this thesis and there are many excellent pieces of literature on this topic like [30] or [31] it is described very briefly.

The Finite Integration Technique is a volume-based discretization scheme that was developed by T. Weiland in 1977 [28], [29]. Based on preliminary studies about of staggered grid Finite Difference Time Domain (FDTD) by Yee et.al. [32], it was a generalization of the dual grid principle for the frequency domain. Later it was generalized for many applications like wakefields [33], eddy-currents [34] and elastodynamics [35] to name only a few.

The basic principle is to decompose the computational domain in several simplistic subdomains, e.g. hexahedrons or tetrahedrons (in 3D) or rectangles and triangles (in 2D). For these subdomains, the solution of Maxwell's equations is known approximately, given that the boundary conditions and the initial fields are known. Furthermore, the correlation between the field strengths from adjacent cells is known analytically (by continuity constraints) and thus, a system of equations of the entire computational domain can be formulated which will be further explained in the following. It should be noted that the theory behind FIT is very complex and only the basic concepts that are needed to explain the notation used in this thesis are reprised. The notations used in this chapter rely heavily on previous literature like [29] and [36] to avoid confusion.

The first step of the discretization is a non-overlapping decomposition of the computational domain by means of a mesh $\mathtt{G}$ with similar, simplistic elements[19] and $\mathtt{I}$, $\mathtt{J}$ and $\mathtt{K}$ nodes in $\mathbf{u}$, $\mathbf{v}$ and $\mathbf{w}$ direction respectively and a number of nodes $N_p = \mathtt{I}\cdot\mathtt{J}\cdot\mathtt{K}$. In order to avoid confusion, the matrices associated with the FIT discretization are

[19] The topological and geometrical dimension of said mesh is obviously determined by the investigated structure.

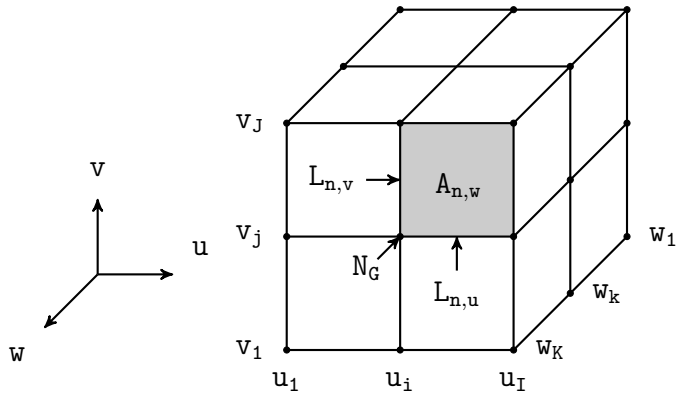

Abbildung 2.2: This picture shows an extract of a hexahedral grid $\mathtt{G}$ with the n-th grid-node $\mathtt{N_G}$ and its associated cell volume $\mathtt{V_n}$, cell-surfaces $\mathtt{A_{n,u}}$, $\mathtt{A_{n,v}}$ and $\mathtt{A_{n,w}}$ and three edges lengths $\mathtt{L_{n,u}}$, $\mathtt{L_{n,v}}$ and $\mathtt{L_{n,w}}$ (only the visible instances are plotted).

presented in a different font, e.g. $\mathtt{G}$. In this thesis, solely hexahedral meshes are used for FIT[20]. For the i-th node in **u** direction, the j-th node in **v** direction and k-th node in **w** direction is numbered as

$$n(i,j,k) = i + (j-1)\mathtt{I} + (k-1)\mathtt{IJ}, \tag{2.45}$$

which is referred to as *lexicographical indexing*. In the following it is referred to an example mesh as shown in Fig. 2.2. Here, the $\mathtt{n}$-th grid-node $\mathtt{N_G}$ is associated with a cell-volume $\mathtt{V_n}$, three cell-surfaces $\mathtt{A_{n,u}}$, $\mathtt{A_{n,v}}$ and $\mathtt{A_{n,w}}$ and three edges lengths $\mathtt{L_{n,u}}$, $\mathtt{L_{n,v}}$ and $\mathtt{L_{n,w}}$. The numbering of the vertices is further highlighted in Fig. 2.2.

Furthermore, a second grid $\tilde{\mathtt{G}}$ (the so-called *secondary grid* or *dual grid*) is introduced, whose nodes are located at the midpoints of the cells of the primary grid. The dual grid can be topologically interpreted as a dual graph of the primary graph (certain properties follow from that, such as the uniqueness of the dual grid [37]). The relationship between the primary grid $\mathtt{G}$ and dual grid $\tilde{\mathtt{G}}$ is highlighted in Fig. 2.3. All quantities being assembled from the dual grid are denoted with a tilde above them as in $\tilde{\mathtt{G}}$.

In order to show the efficiency of the latter described approach in reformulating complex PDEs in linear operators, in the following it is explained how the integral form of Maxwell's equations (2.1)-(2.4) can be discretized using FIT. Starting with the integral law of induction (2.2), the electric voltage over an edge $\widehat{\mathbf{e}}_u(i,j,k)$ is defined as

$$\widehat{\mathbf{e}}_u(i,j,k) = \int_{L_\mathrm{u}(i,j,k)} \mathbf{E}\,(\mathbf{r},t) \cdot \mathrm{d}\mathbf{s}, \tag{2.46}$$

[20] In some cases, the usage of tetrahedrons can lead to superior convergence, but unfortunately there is no software, commercial or open-source, which employs FIT with tetrahedrons. Therefore, the implementation in this thesis relies on hexahedrons which is discussed further in Chapter 3.2.

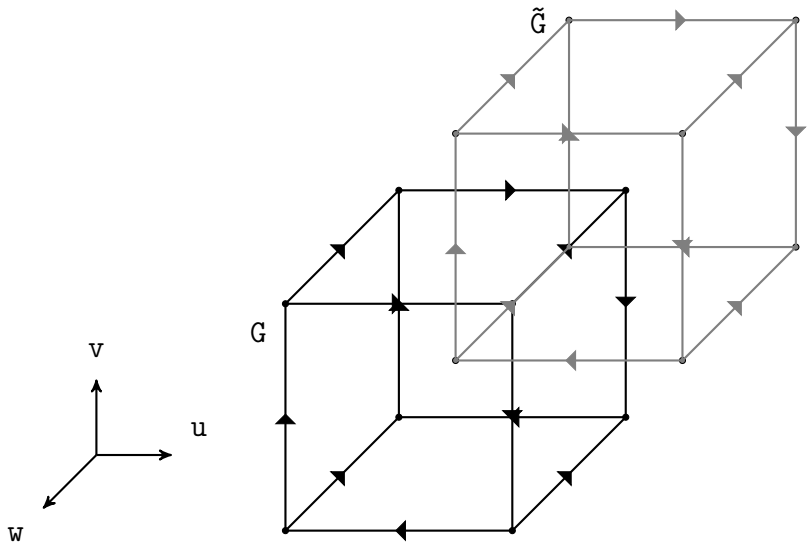

Abbildung 2.3: This picture highlights the correlation between the primary grid G and the dual grid G̃ for two adjacent cells. The nodes of the dual grid are located at the midpoints of the cells of the primary grid. Thus, the midpoints of the edges of the dual grid are located in the middle of the primary grids surfaces and vice versa. The idea is adapted from [32].

with the bow indicating that it results from a one-dimensional integral. This is referred to as a so-called *integral-state quantity*. Furthermore the magnetic flux through a surface $A_p(i,j,k)$ is defined as

$$\widetilde{\widehat{b}}_w(i,j,k) = \iint_{A_\mathrm{u}(i,j,k)} \mathbf{B}(\mathbf{r},t) \cdot \mathrm{d}\mathbf{A}, \tag{2.47}$$

with the two bows indicating that it results from a two-dimensional integration. Using (2.46) and (2.47) the integral induction law (2.2) can be expressed inside a closed surface $A_\mathrm{u}(i,j,k)$ without simplifications[21] as

$$\widehat{\mathbf{e}}_u(i,j,k) + \widehat{\mathbf{e}}_v(i+1,j,k) - \widehat{\mathbf{e}}_u(i,j+1,k) - \widehat{\mathbf{e}}_v(i,j,k) = -\frac{\mathrm{d}}{\mathrm{d}t}\widetilde{\widehat{b}}_w(i,j,k), \tag{2.48}$$

which is further highlighted in Fig. 2.4.

The equation (2.48) has to be assembled not only for one surface but on the entire mesh G. From (2.48) one can see that this can be done separately for all three spatial directions by a matrix that contains 1 and -1 twice in each row, with the rest being zero. One can define the auxiliary matrices P as

[21] Up until this point no simplifications to Maxwell's integral equations were introduced, such that the solution is still free of approximations.

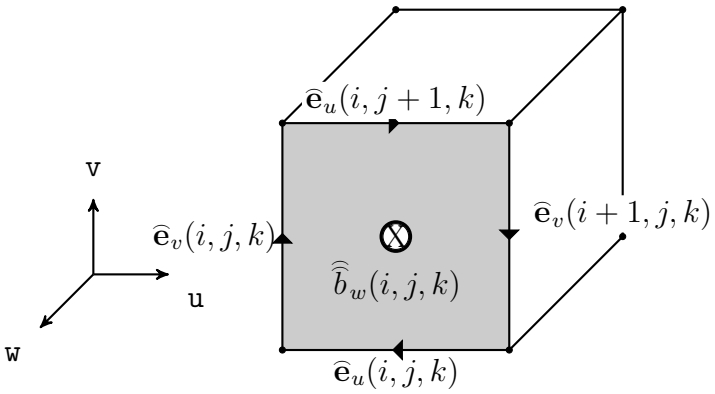

Abbildung 2.4: This picture emphasizes the discretization of the induction law (2.2) using FIT as in (2.48). The induction law states that the magnetic flux density through the surface $\mathtt{A}_{\mathtt{n},\mathtt{w}}$ is equal to the sum over all integrated electric field strengths along the enclosing grid-edges.

$$\left[\mathtt{P}_{u\|v\|w}\right]_{p,q} = \begin{cases} -1 \text{ for } p = q \\ 1 \text{ for } p = q + r \\ 0 \text{ else,} \end{cases} \tag{2.49}$$

with the notation indicating that it is either $\mathtt{P}_u$ with $r = 1$, $\mathtt{P}_v$ with $r = I$ or $\mathtt{P}_w$ with $r = IJ$. If the vectors $\widehat{\mathbf{e}}$ and $\widehat{\bar{b}}$ are sorted first in $\mathbf{u}$, then in $\mathbf{v}$ and then in $\mathbf{w}$ direction, the resulting matrix $\mathtt{C}$ is banded and sparse with the block structure

$$\mathtt{C} = \begin{pmatrix} 0 & -\mathtt{P}_w & \mathtt{P}_v \\ \mathtt{P}_w & 0 & -\mathtt{P}_u \\ -\mathtt{P}_v & \mathtt{P}_u & 0 \end{pmatrix}. \tag{2.50}$$

The topological operator $\mathtt{C}$ is further denoted as the *discretized curl operator*. At this point, the first approximation is introduced by expressing the integral-state quantities as a sampled variable in the middle of their geometric facet (e.g. the middle of an edge, a surface or volume) multiplied by the size of their geometric facet they are defined on (e.g. the length of an edge, the size of a surface or a volume), which leads to the so-called *sample state quantities*. As an example the electric voltage over an edge $\bar{\mathbf{e}}_u(i,j,k)$ is approximated by

$$\widehat{\mathbf{e}} \approx \mathtt{D}_S \mathbf{e}, \tag{2.51}$$

with $\mathbf{e}$ being the sample state electric field. This approximation is made accordingly for all other integral-state variables where the field strengths $\widehat{\mathbf{e}}$, $\widehat{\mathbf{h}}$ are approximated at edges, the flux densities $\widehat{\bar{b}}$, $\widehat{\bar{d}}$ and $\widehat{\bar{j}}$ are approximated at the middle of the surfaces and the charge density $\widehat{\bar{\rho}}$ is approximated at the middle of a cell volume. This way, using the definition of the discretized curl operator (2.50) and the sample-state

variables as well as the induction law for a single cell-surface (2.48), the *discretized induction law using sample state variables* can be formulated as

$$\mathtt{C}\mathtt{D}_S\mathbf{e} \approx -\frac{\mathrm{d}}{\mathrm{d}t}\mathtt{D}_A\mathbf{b}. \tag{2.52}$$

The same derivations as for (2.52) can be done for the integral form of Ampère's law (2.1) which leads to the *discretized Ampère's law using sample state variables*

$$\tilde{\mathtt{C}}\tilde{\mathtt{D}}_S\mathbf{h} \approx \tilde{\mathtt{D}}_A\left(\frac{\mathrm{d}}{\mathrm{d}t}\mathbf{d} + \mathbf{j}\right). \tag{2.53}$$

The second set of equations deals with surface integrals of the flux densities (2.3) and (2.4), explanatory, the Gauss's law of electric fields is explained in the following. It holds that

$$\widehat{\widetilde{d}}_u(i,j,k) + \widehat{\widetilde{d}}_v(i+1,j,k) - \widehat{\widetilde{d}}_u(i,j+1,k) - \widehat{\widetilde{d}}_v(i,j,k) = \widehat{\widehat{\widetilde{\rho}}}(i,j,k), \tag{2.54}$$

through any arbitrary cell of the dual grid $\tilde{\mathtt{G}}$, normal to $\mathbf{w}$. Again, the integral state variables are replaced by sample state variables by introducing the simplification, that the electric flux through the surfaces of the dual-grid are replaced by the electric flux density at the midpoint of the surface, multiplied by the surface area and the electric charges inside the cell are replaced by the electric charge density at the midpoint of the cell-volume multiplied by the cell-volume. Comprising this equation for all dual-grid cells leads to

$$\tilde{\mathtt{S}}\tilde{\mathtt{D}}_A\mathbf{d} \approx \tilde{\mathtt{D}}_V\rho, \tag{2.55}$$

with $\tilde{\mathtt{S}}$, being the *discretized divergence operator* of the dual grid. Analogously, the same derivation can be done for the integral Gauss's law of magnetic fields (2.4), which leads to

$$\mathtt{S}\mathtt{D}_A\mathbf{b} \approx \mathbf{0}. \tag{2.56}$$

The equations (2.52), (2.53), (2.55) and (2.56) comprise the discrete formulation of the integral Maxwell's equations using FIT.

An interesting property of the discrete FIT operators is that many properties that their continuous equivalent operators possess, remain throughout the discretization, which is generally not the case when using a FEM discretization. In the continuous case, it holds that the divergence of a curl of any arbitrary vector-field equals zero, while in the discretized FIT case it holds that

$$\mathtt{S}\mathtt{C} = \tilde{\mathtt{S}}\tilde{\mathtt{C}} = \mathbf{0} \;\text{ equivalent to }\; \nabla\cdot\nabla\times = 0. \tag{2.57}$$

Furthermore, it holds that the curl of the gradient of any arbitrary scalar-field is zero

$$\mathtt{C}\tilde{\mathtt{S}}^{\mathrm{T}} = \tilde{\mathtt{C}}\tilde{\tilde{\mathtt{S}}}^{\mathrm{T}} = \mathbf{0} \text{ equivalent to } \nabla \times \nabla = 0. \tag{2.58}$$

The discussed Maxwell's Grid Equations (MGE) (2.52), (2.53), (2.55) and (2.56) are used in this thesis to discretize all investigated physical phenomena. The specific theory and implementation is reprised in Chapter 3.2. As stated in Chapter 2.1, for a full description of the investigated effects, one additionally needs the material equations to describe the relation between the field strengths and the flux density of the respected fields. In FIT the material properties are averaged over each cell and comprised into matrix-form[22]. The permeability, the permittivity and the conductivity form diagonal matrices $\mathtt{D}_\mu$, $\mathtt{D}_\epsilon$ and $\mathtt{D}_\kappa$ respectively, which leads to the *discretized material equations*

$$\widehat{\widehat{d}} \approx \mathtt{M}_\epsilon \widehat{\mathbf{e}} \text{ with } \mathtt{M}_\epsilon \approx \tilde{\mathtt{D}}_A \mathtt{D}_\epsilon \mathtt{D}_{\tilde{S}}^{-1}, \tag{2.59}$$

$$\widehat{\widehat{b}} \approx \mathtt{M}_\mu \widehat{\mathbf{h}} \text{ with } \mathtt{M}_\mu \approx \tilde{\mathtt{D}}_A \mathtt{D}_\mu \mathtt{D}_{\tilde{S}}^{-1}, \tag{2.60}$$

$$\widehat{\widehat{j}} \approx \mathtt{M}_\kappa \widehat{\mathbf{e}} \text{ with } \mathtt{M}_\kappa \approx \mathtt{D}_A \mathtt{D}_\kappa \tilde{\mathtt{D}}_{\tilde{S}}^{-1}. \tag{2.61}$$

In combination with the MGE, the discretized material equations are sufficient for the numerical discretization in this thesis. The choice of FIT over the theoretically more flexible FEM[23] was met due to the availability of FIT in a powerful commercial software CST Microwave Studio ® (CST MWS) [38][24]. Furthermore, FIT has several advantages regarding the simplicity of an implementation e.g. due to the physical consistency (see (2.57) and (2.58)) of the matrix operators.

2.4 System Description of SRF Structures

An important aspect of this thesis is the description of second-order, partial differential equations by using a simplified model, which describes the electromagnetic behavior using a system of *ordinary differential equations* (further denoted as ODE) [39]. This chapter aims for the introduction of some basic concepts of this methodology, while the specific application of it for the state-space concatenation method and FIT is explained in Chapters 3.1.2 and 3.2.2, respectively.

[22] Obviously, the averaging of the material properties leads to an approximation. However, for this thesis it is rather irrelevant, since only homogeneous media are investigated.

[23] FEM is more flexible due to the variability of mesh-type as well as order of ansatz functions, which can be chosen according to the problem at hand.

[24] For convenience, the ® symbol indicating a registered trademark symbol is omitted from hereon for CST MWS.

2.4.1 State-Space Models

The goal of this description is to obtain a general vector of outputs of a system (in this case a set of modal voltages $\mathbf{v}_\mathrm{g}(t)$) as reaction to a general vector of inputs (in this case a set of modal currents $\mathbf{i}_\mathrm{g}(t)$) by two systems of ODEs and a vector of inner states $\mathbf{x}_\mathrm{g}(t)$. Such a description is denoted as State-Space Model (SSM) in the literature. The first system of ODEs, the so-called *state-equation*, links the inputs to the inner states of the system and describes its dynamic behavior by

$$\frac{\mathrm{d}}{\mathrm{d}t}\mathbf{x}_\mathrm{g}(t) = \mathbf{A}_\mathrm{g}\mathbf{x}_\mathrm{g}(t) + \mathbf{B}_\mathrm{g}\mathbf{i}_\mathrm{g}(t), \tag{2.62}$$

with the general state-matrix $\mathbf{A}_\mathrm{g}$ and the input-matrix $\mathbf{B}_\mathrm{g}$. The inner-states can influence the outputs by the *output-equation* as

$$\mathbf{v}_\mathrm{g}(t) = \mathbf{C}_\mathrm{g}\mathbf{x}_\mathrm{g}(t) + \mathbf{D}_\mathrm{g}\mathbf{i}_\mathrm{g}(t), \tag{2.63}$$

with the *output-matrix* $\mathbf{C}_\mathrm{g}$ and the *feedthrough-matrix* $\mathbf{D}_\mathrm{g}$. For further convenience, the state-space model is chosen to be symmetric which means that the output matrix is the transpose of the input matrix, i.e. $\mathbf{C}_\mathrm{g} = \mathbf{B}_\mathrm{g}^\mathrm{T}$. For lossless, charge-free and time invariant RF systems, it is generally possible to find a state-space model such that the matrices $\mathbf{A}_\mathrm{g}, \mathbf{B}_\mathrm{g}$, $\mathbf{C}_\mathrm{g}$ and $\mathbf{D}_\mathrm{g}$ are constant, hence not time dependent [40]. For frequency-domain investigations it is more convenient to transform the equations (2.62) and (2.63) into the frequency domain which leads to

$$s\mathbf{x}_\mathrm{g}(s) = \mathbf{A}_\mathrm{g}\mathbf{x}_\mathrm{g}(s) + \mathbf{B}_\mathrm{g}\mathbf{i}_\mathrm{g}(s), \tag{2.64}$$

$$\mathbf{v}_\mathrm{g}(s) = \mathbf{C}_\mathrm{g}\mathbf{x}_\mathrm{g}(s) + \mathbf{D}_\mathrm{g}\mathbf{i}_\mathrm{g}(s), \tag{2.65}$$

with the complex frequency parameter s which originates from the Laplace transform. Of special interest is the transmission function of this system. In the case of an impedance formulation as (2.62) and (2.63), the transmission function would comprise the impedance parameters as

$$\mathbf{Z}_\mathrm{g}(s) = \mathbf{C}_\mathrm{g}\left(s\mathbf{I} - \mathbf{A}_\mathrm{g}\right)^{-1}\mathbf{B}_\mathrm{g} + \mathbf{D}_\mathrm{g}. \tag{2.66}$$

Furthermore, in case of a scattering formulation, the transmission functions would comprise the scattering parameters.

2.4.2 Model-Order Reduction by Projection

The initial system (2.64) and (2.65) can be comprised as

$$\mathbf{M}_\mathrm{g,full} = \left[\begin{array}{c|c} \mathbf{A}_\mathrm{g} & \mathbf{B}_\mathrm{g} \\ \hline \mathbf{C}_\mathrm{g} & \mathbf{D}_\mathrm{g} \end{array}\right] \in \mathbb{R}^{(n+p)\times(n+m)} \tag{2.67}$$

with n being the number of internal states, p being the number of inputs and m being the number of outputs. However, as stated earlier, such a description generally requires a comparably large number of DOFs for a sufficiently accurate description (i.e. a large n). For problems investigated in this thesis several Mio. DOFs are necessary for a sufficiently accurate representation of the underlying PDEs. In order to heavily reduce the computational demand, a model-order reduction by symmetric projection is a commonly applied technique. In this case a general projection matrix $\mathbf{W}_\mathrm{g}$ with $\mathbf{W}_\mathrm{g} \in \mathbb{R}^{k\times n}$ can be constructed such that

$$\mathbf{x}_\mathrm{g}(s) = \mathbf{W}_\mathrm{g}^{-1}\mathbf{x}_\mathrm{g,red}(s). \tag{2.68}$$

In this case, the resulting reduced state-space system can be comprised as

$$s\mathbf{x}_\mathrm{g,red}(s) = \underbrace{\mathbf{W}_\mathrm{g}\mathbf{A}_\mathrm{g}\mathbf{W}_\mathrm{g}^{-1}}_{\mathbf{A}_\mathrm{g,red}}\mathbf{x}_\mathrm{g,red}(s) + \underbrace{\mathbf{W}_\mathrm{g}\mathbf{B}_\mathrm{g}}_{\mathbf{B}_\mathrm{g,red}}\mathbf{i}_\mathrm{g}(s), \tag{2.69}$$

$$\mathbf{v}_\mathrm{g,red}(s) = \underbrace{\mathbf{B}_\mathrm{g}^\mathrm{T}\mathbf{W}_\mathrm{g}^{-1}}_{\mathbf{C}_\mathrm{g,red}}\mathbf{x}_\mathrm{g,red}(s) + \underbrace{\mathbf{D}_\mathrm{g}}_{\mathbf{D}_\mathrm{g,red}}\mathbf{i}_\mathrm{g}(s), \tag{2.70}$$

with the comprised system representation

$$\mathbf{M}_\mathrm{g,red} = \left[\begin{array}{c|c} \mathbf{W}_\mathrm{g}\mathbf{A}_\mathrm{g}\mathbf{W}_\mathrm{g}^{-1} & \mathbf{W}_\mathrm{g}\mathbf{B}_\mathrm{g} \\ \hline \mathbf{B}_\mathrm{g}^\mathrm{T}\mathbf{W}_\mathrm{g}^{-1} & \mathbf{D}_\mathrm{g} \end{array}\right] \in \mathbb{R}^{(k+p)\times(k+m)}. \tag{2.71}$$

For the construction of the projection matrix it should hold that the new system $\mathbf{M}_\mathrm{g,red}$ is orders of magnitude smaller than the initial system $\mathbf{M}_\mathrm{g,full}$, i.e. $k \ll n$. According to [41], for the construction of the projection matrix it should hold that

- the approximation error is small,
- the systems properties are preserved like stability, passivity etc.,
- the procedure is computationally stable and efficient.

There are generally many ways to construct said projection matrix $\mathbf{W}_\mathrm{g}$. All of the latter demanded properties are given for so-called *Corrected Modal Expansion* (further denoted as CME) [40] which is used throughout this thesis and is further discussed in Chapter 3.1.3.

3 The State-Space Concatenation Scheme

As introduced in Chapter 1.2, the main topic of this thesis is the numerical simulation of electromagnetic fields in long and complex SRF structures. Therefore, generally comparably large numbers of Degrees of Freedom (DOFs), i.e. several millions, are required for a sufficiently accurate computation of the electromagnetic fields. In order to overcome this problem, the so called State-Space Concatenation scheme (SSC) was proposed in [7] and further improved in [8]. SSC is a combination of domain decomposition and model-order reduction techniques in order to solve Maxwell's equations for large, complex, lossless SRF structures and is used for this purpose throughout the thesis. In SSC, firstly, the structure is subdivided into N_{seg} non-overlapping subdomains. For each of these N_{seg} subdomains the RF properties are comprised using a state-space model $\mathbf{M}_{\text{full,n}}$ (as introduced in (2.67)) which can originate either from analytical considerations or from a numerical discretization of Maxwell's equations on the subdomain. Furthermore, due to the size of $\mathbf{M}_{\text{full,n}}$ it is advantageous to reduce the order. This is done for each model separately by employing a *corrected modal expansion* (CME) which drastically reduces the order and obtains the n-th reduced model $\mathbf{M}_{\text{red,n}}$. As final step, all N_{seg} reduced models $\mathbf{M}_{\text{red,n}}$ are concatenated such that the reduced model of the full structure $\mathbf{M}_{\text{conc}}$ is obtained. For this model $\mathbf{M}_{\text{conc}}$ one can reduce the order even further by employing a MOR by CME once again, resulting in the final model $\mathbf{M}_{\text{conc,red}}$ which comprises the relevant RF properties of the full structure in the given frequency domain. These latter described steps are highlighted in Fig. 3.1.

A task of this thesis was to efficiently implement the theoretically described method, as well as automate it for arbitrary structures. Furthermore, in Chapter 4, the method is generalized such that it allows for the computation of certain losses. This chapter is organized as follows. Firstly, the theoretical basis of SSC is discussed, with the domain-decomposition, the derivation of the non-reduced SSM, the MOR by CME and the concatenation. Secondly, the implementation and automation are discussed in detail. Finally, an analytically solvable example is shown and the method is theoretically compared to other methods that reduce the model order and are used in accelerator physics.

3.1 Theoretical Basis of SSC

In this section, the theoretical basics of SSC are outlined. For a detailed explanation it is referred to the appropriate literature [8] and [40]. The steps are discussed in

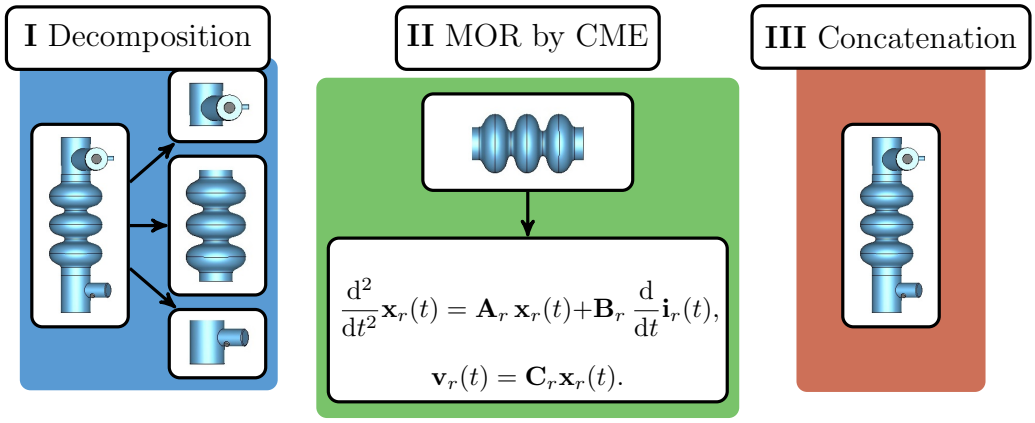

Abbildung 3.1: This picture shows the three different steps of SSC on the example of a 3-cell cavity with couplers. In the first step (highlighted in blue) the structure is decomposed into several substructures. Then for each substructure, a MOR is employed (highlighted in green) and as a last step, the models of the substructures are concatenated to SSM of the initial structure (highlighted in red). The picture is taken from [14].

the order in which they are required to be performed, i.e. firstly the domain decomposition, then the assembly of the non-reduced SSMs and finally the concatenation of all SSMs.

3.1.1 Domain Decomposition

In the first step of SSC, the domain in which the electromagnetic fields are to be computed, is decomposed into N_{seg} non-overlapping subdomains. In a subsequent MOR, every structure is treated separately, with the cutting planes turned into waveguide ports. The decomposition is theoretically arbitrary in the number of subdomains. The location of the cutting planes, separating the subdomains, has to be in a domain with constant cross section along the cutting plane. In practice, both parameters, the location as well as the number of cutting planes, have to be chosen such that the computational time for the entire computation is minimal. Their effect on the computational time is briefly discussed in this subsection. As one extreme one could not decompose the structure at all (i.e. $N_{\mathrm{seg}} = 1$), in which the subsequent MOR would require a comparably high computational time. The other extreme would be the decomposition into a large number of subdomains (i.e. $N_{\mathrm{seg}} \to \infty$), in which case the required number of 2D port-modes would get impractically high. In the following, this is explained more in-depth.

Firstly, the MOR by CME scales roughly linearly with the number of 2D modes at the waveguide ports (this becomes clear in Chapter 3.1.3), thus it would be advantageous to keep this number sufficiently small, by positioning the cutting planes accordingly. If the cutting planes (thus the waveguide ports in the MOR)

were infinitely far away from each other, only 2D modes which are able to propagate in the chosen frequency domain have to be taken into account for an accurate representation. If now the cutting planes were closer together (e.g. by a different choice of decomposition), there is a finite number of additional, evanescent 2D modes that (even though they are damped) could traverse through the structure and still have non-negligible energy after covering the distance between the two ports. Thus the number of 2D modes that have to be taken into account at both ports increases if the distance between two cutting planes decreases. Therefore, taking the scaling of the MOR into account, one tries to position the cutting planes such that their distance to each other is maximal.

Unfortunately, maximizing the distance between two cutting planes also increases the domain between them. Generally, for more complex domains that means that a discretization of Maxwell's equations in said domain requires more DOFs, thus increasing the computational time of the MOR. Furthermore, since repeating substructures should be treated only once, the computational time can be drastically reduced by decomposing the domain into several repeating subdomains. Also a decomposition into subdomains that can be treated analytically is advantageous. All of these points have to be taken into account to find a decomposition that allows for fast computations. In practice this is (currently) done by experience.

3.1.2 Non-reduced State-Space Impedance Model of Segments

For each of the N_{seg} subdomains originating from the domain decomposition, one has to assemble the non-reduced SSM derived from the discretization of Maxwell's equation in the subdomain. In this subsection, the non-reduced system is formulated, closely following [8] and [40]. For further convenience an alternative, compact notation of Maxwell's equations (2.8) and (2.9) in lossless, charge-free waveguides with homogeneous materials is introduced as

$$\frac{\mathrm{d}}{\mathrm{d}t}\begin{pmatrix}\mathbf{E}(\mathbf{r},t)\\ \mathbf{H}(\mathbf{r},t)\end{pmatrix}=\begin{pmatrix}0 & \varepsilon^{-1}\nabla\times\\ -\mu^{-1}\nabla\times & 0\end{pmatrix}\begin{pmatrix}\mathbf{E}(\mathbf{r},t)\\ \mathbf{H}(\mathbf{r},t)\end{pmatrix}-\begin{pmatrix}\varepsilon^{-1}\\ 0\end{pmatrix}\mathbf{J}(\mathbf{r},t). \tag{3.1}$$

The vector of unknowns $(\mathbf{E}(\mathbf{r},t),\mathbf{H}(\mathbf{r},t))^{\mathrm{T}}$ is transformed in such a way that all comprised quantities have the same unit. Therefore, the normed electric field strength $\bar{\mathbf{E}}(\mathbf{r},t)=\varepsilon^{\frac{1}{2}}\mathbf{E}(\mathbf{r},t)$ and the normed magnetic field strength $\bar{\mathbf{H}}(\mathbf{r},t)=\mu^{\frac{1}{2}}\mathbf{H}(\mathbf{r},t)$ are introduced leading to

$$\frac{\mathrm{d}}{\mathrm{d}t}\begin{pmatrix}\bar{\mathbf{E}}(\mathbf{r},t)\\ \bar{\mathbf{H}}(\mathbf{r},t)\end{pmatrix}=\begin{pmatrix}0 & \varepsilon^{-\frac{1}{2}}\mu^{-\frac{1}{2}}\nabla\times\\ -\varepsilon^{-\frac{1}{2}}\mu^{-\frac{1}{2}}\nabla\times & 0\end{pmatrix}\begin{pmatrix}\bar{\mathbf{E}}(\mathbf{r},t)\\ \bar{\mathbf{H}}(\mathbf{r},t)\end{pmatrix}-\begin{pmatrix}\varepsilon^{-\frac{1}{2}}\\ 0\end{pmatrix}\mathbf{J}(\mathbf{r},t), \tag{3.2}$$

with the unit of the unknown quantities as $\sqrt{\frac{VAs}{m^3}}$. It is further advantageous to reformulate the system under the usage of (2.9), in such a way that the normalised magnetic field strength is eliminated, which leads to

$$\frac{\mathrm{d}^2}{\mathrm{d}t^2}\bar{\mathbf{E}}\left(\mathbf{r},t\right) = -\varepsilon^{-1}\mu^{-1}\nabla\times\nabla\times\bar{\mathbf{E}}\left(\mathbf{r},t\right) - \varepsilon^{-\frac{1}{2}}\mathbf{J}(\mathbf{r},t). \tag{3.3}$$

Recalling the initial assumptions for the waveguide that it is free of charge and evacuated (i.e. the conductivity is 0), the current density $\mathbf{J}(\mathbf{r},t)$ in (3.2) can be simplified as $\mathbf{J}(\mathbf{r},t) = \mathbf{J}_{\mathrm{imp}}(\mathbf{r},t)$ according to (2.7). The imprinted current density $\mathbf{J}_{\mathrm{imp}}(\mathbf{r},t)$ can be expressed as a sum of all imprinted current densities at all waveguide ports and their respective 2D modes, weighted with the mode's modal current $\mathbf{i}_{\mathrm{m}}(t)$ (see Chapter 2.2.4)

$$\mathbf{J}_{\mathrm{imp}}(\mathbf{r},t) = \sum_{m=1}^{M_{\mathrm{2D}}} \mathbf{J}_{\mathrm{imp,m}}(\mathbf{r})\mathrm{i}_{\mathrm{m}}(t), \tag{3.4}$$

with the total number of 2D modes M_{2D}. Furthermore the imprinted current density at the waveguides can be rephrased according to (2.37), which leads to

$$\frac{\mathrm{d}^2}{\mathrm{d}t^2}\bar{\mathbf{E}}\left(\mathbf{r},t\right) = -\varepsilon^{-1}\mu^{-1}\nabla\times\nabla\times\bar{\mathbf{E}}\left(\mathbf{r},t\right) + \varepsilon^{-\frac{1}{2}}\sum_{m=1}^{M_{\mathrm{2D}}}\mathbf{L}_{\mathrm{t,m}}(\mathbf{r}_{\mathrm{t}})\mathrm{i}_{\mathrm{m}}(t), \tag{3.5}$$

with the scalar $\mathrm{i}_{\mathrm{m}}(t)$ being the m-th modal current. The modal voltage as introduced in (2.27) can be comprised as

$$\mathbf{v}(t) = \varepsilon^{-\frac{1}{2}}\sum_{m=1}^{M_{\mathrm{2D}}}\iint_{\mathbf{\Gamma}_{\mathrm{Prt}}}\mathbf{L}_{\mathrm{t,m}}(\mathbf{r})\cdot\bar{\mathbf{E}}\left(\mathbf{r},t\right)\partial\mathbf{\Gamma}_{\mathrm{Prt}}. \tag{3.6}$$

As mentioned in subsection 2.2.4, one has to apply PMC boundary conditions at all waveguide ports. The system (3.5) and (3.6) resembles a state-space system (as in e.g. (2.64) and (2.65)), with the state-space matrices being operators instead of matrices. This system serves as a theoretical basis for further considerations. In practice, it is discretized using an appropriate technique, such as FIT or FEM.

3.1.3 Model-Order Reduction by Projection

To increase the efficiency of the concatenation it is advantageous to reduce the models of all segments in order. For the MOR used in SSC, a CME is used, as introduced in [8] and [40], with the basic idea being outlined in the following.

The corrected modal expansion can be divided into three steps. Firstly, an incomplete eigendecomposition of the system matrix of the non-reduced SSM $\mathbf{A}_{\mathrm{full,n}}$ is computed, by computing all eigenmodes in the frequency domain of interest. The

subindex n to indicate the n-th segment is neglected in the following for the sake of simplicity of the notation. In a second step this eigendecomposition is improved in accuracy by expanding the orthogonal basis with some few additional vectors that arise from an orthogonal decomposition of the systems' response to a frequency-excitation at the waveguide ports. Thirdly, the system matrix arising from the first two steps is diagonalized by a direct and complete eigendecomposition.

Firstly an eigendecomposition of the system matrix is employed. One can decompose any square matrix $\mathbf{A}$ with N_{DOF} linearly independent eigenvectors as $\mathbf{A} = \mathbf{Q}\mathbf{\Lambda}\mathbf{Q}^{\mathrm{T}}$, with $\mathbf{Q}$ being a square matrix whose n-th column contains the n-th eigenvector of $\mathbf{A}$ and $\mathbf{\Lambda}$ which contains the eigenvalues on the diagonal. For the systems investigated in this thesis, a complete orthogonal decomposition is impractical due to the size of the matrix[1]. Therefore, an incomplete eigendecomposition of the system matrix is employed where only a small number $N_{3\mathrm{D}}$ of relevant eigenvectors and eigenvalues are determined. With the matrix $\mathbf{Q}_{\mathrm{inc}}$, containing only a few relevant eigenvectors, the state-vector can be projected to a suitable subspace as $\mathbf{x}_{\mathrm{red}} = \mathbf{Q}_{\mathrm{inc}}^{\mathrm{T}}\,\mathbf{x}_{\mathrm{full}}$ which leads to

$$\mathbf{A}_{\mathrm{red,e}} = \mathbf{Q}_{\mathrm{inc}}^{\mathrm{T}}\mathbf{A}_{\mathrm{full}}\mathbf{Q}_{\mathrm{inc}}, \tag{3.7}$$

where $\mathbf{Q}_{\mathrm{inc}}$ has the size $\mathbf{Q}_{\mathrm{inc}} \in \mathbb{R}^{N_{\mathrm{DOF}} \times N_{3\mathrm{D}}}$, with $N_{3\mathrm{D}} \ll N_{\mathrm{DOF}}$, thus drastically decreasing the order of $\mathbf{A}_{\mathrm{full}} \in \mathbb{R}^{N_{\mathrm{DOF}} \times N_{\mathrm{DOF}}}$ to $\mathbf{A}_{\mathrm{red,e}} \in \mathbb{R}^{N_{3\mathrm{D}} \times N_{3\mathrm{D}}}$ and the input-matrix as

$$\mathbf{B}_{\mathrm{red,e}} = \mathbf{Q}_{\mathrm{inc}}^{\mathrm{T}}\mathbf{B}_{\mathrm{full}}, \tag{3.8}$$

with $\mathbf{B}_{\mathrm{red,e}} \in \mathbb{R}^{N_{\mathrm{DOF}} \times M_{2\mathrm{D}}}$. A SSM employing this reduction is rather impractical since $N_{3\mathrm{D}}$ has to be comparably high to reach a sufficient accuracy in the RF parameters due to the poor convergence order of such partial eigendecomposition. In practice, $N_{3\mathrm{D}}$ is chosen to be roughly equal to the number of 3D modes in the frequency domain of interest. To account for the modes above said spectrum, one could simply increase $N_{3\mathrm{D}}$, which (in most cases) is computationally not feasible. Instead, an additional set of eigenfunctions is introduced by the computation of so-called *snapshots*, which is outlined in the following.

The eigenvectors of the initial, incomplete eigendecomposition are comprised in the matrix $\mathbf{X}_{\mathrm{inc}}$ as

$$\mathbf{X}_{\mathrm{inc}} = [\mathbf{x}_{\mathrm{inc},1},\, \mathbf{x}_{\mathrm{inc},2},\, \ldots,\, \mathbf{x}_{\mathrm{inc},N_{3\mathrm{D}}}] \tag{3.9}$$

In the next step, the system response (i.e. the inner state $\mathbf{x}_{\mathrm{sn},i}$) of the Fourier-transformed, non-reduced SSM is computed for various frequency excitations as

[1] In case of a system that is obtained in an analytical manner it is impractical since there are infinitely many eigenmodes to the $\nabla \times \nabla \times$ operator in (3.5).

$$\mathbf{x}_{\mathrm{sn},i} = (-\omega_i^2 \mathbf{I} - \mathbf{A}_{\mathrm{full}})^{-1} \mathbf{B}_{\mathrm{full}}\, j\omega_i, \tag{3.10}$$

and said inner states $\mathbf{x}_{\mathrm{sn},i}$ are comprised in the matrix $\mathbf{X}_{\mathrm{sn}}$ as

$$\mathbf{X}_{\mathrm{sn}} = [\mathbf{x}_{\mathrm{sn},1},\, \mathbf{x}_{\mathrm{sn},2},\, \ldots,\, \mathbf{x}_{\mathrm{sn},n}] \tag{3.11}$$

In the following a *singular value decomposition* (SVD)[2] of a block matrix holding $\mathbf{X}_{\mathrm{inc}}$ and $\mathbf{X}_{\mathrm{sn}}$ is performed

$$\mathbf{U}\mathbf{\Sigma}\mathbf{R}^{\mathrm{T}} = [\mathbf{X}_{\mathrm{inc}}\,,\, \mathbf{X}_{\mathrm{sn}}] \tag{3.12}$$

This is repeated iteratively while placing new snapshots. The snapshots are placed with equal spacing[3] over the frequency domain. If the minimal singular value of the SVD in (3.12), drops below a certain accuracy the procedure is stopped.

It should be noted that there are more advanced schemes available for the MOR. Especially the computation of the eigenmodes of the system matrix in (3.9) seems unnecessary since in principle it would be sufficient to solely use snapshots and derive the orthogonal basis solely from the systems response to excitations. It is however possible that there are modes in the structure that do not couple to the boundary (i.e. to the waveguide ports) but can couple to the beam. Such modes could not be found by snapshots but only by computing the eigendecomposition of the system matrix directly. Even though such modes were not observed in any practical example, the eigendecomposition of the system matrix is computed directly as a precaution. The latter described procedure is used to project the inner states to the space from the CME with $\mathbf{x}_{\mathrm{cme}}(t) = \mathbf{U}^{\mathrm{T}}\mathbf{x}_{\mathrm{red,e}}$, which leads to the SSM

$$\frac{\mathrm{d}^2}{\mathrm{d}t^2}\mathbf{x}_{\mathrm{cme}}(t) = \mathbf{U}^{\mathrm{T}}\mathbf{A}_{\mathrm{red,e}}\mathbf{U}\mathbf{x}_{\mathrm{cme}}(t) + \mathbf{U}^{\mathrm{T}}\mathbf{B}_{\mathrm{red,e}}\frac{\mathrm{d}}{\mathrm{d}t}\mathbf{i}(t), \tag{3.13}$$

$$\mathbf{v}(t) = \mathbf{B}_{\mathrm{red,e}}^{\mathrm{T}}\mathbf{U}\mathbf{x}_{\mathrm{cme}}(t). \tag{3.14}$$

As final step, the state-matrix is diagonalized by employing a complete eigendecomposition by $\mathbf{A}_{\mathrm{cme}} = \mathbf{Q}_{\mathrm{cme}}\mathbf{\Lambda}_{\mathrm{cme}}\mathbf{Q}_{\mathrm{cme}}^{\mathrm{T}}$ which leads to the final SSM as

$$\frac{\mathrm{d}^2}{\mathrm{d}t^2}\mathbf{x}_{\mathrm{cme,diag}}(t) = \mathbf{\Lambda}_{\mathrm{cme}}\mathbf{x}_{\mathrm{cme,diag}}(t) + \mathbf{Q}_{\mathrm{cme}}^{\mathrm{T}}\mathbf{B}_{\mathrm{cme}}\frac{\mathrm{d}}{\mathrm{d}t}\mathbf{i}(t), \tag{3.15}$$

[2] SVD is a generalization of eigendecomposition of rectangular matrices. Geometrically, this can be understood as a decomposition of an arbitrary transformation into a rotation, a scaling and another rotation. For this specific application, an economic size SVD is faster since the number of DOFs is orders of magnitude larger than the number of snapshots.

[3] In the future it might be advantageous to find schemes that have an optimal spacing of the snapshots in the frequency range. For example a so-called *greedy* placing, which places a new snapshot at the frequency with the biggest deviation between reduced and full model, is possible. The problem is that the identification of the frequency with the biggest deviation is computationally very expensive. This could be overcome with an error estimator which is currently not present.

$$\mathbf{v}(t) = \mathbf{B}_{\text{cme}}^{\text{T}} \mathbf{Q}_{\text{cme}} \mathbf{x}_{\text{cme,diag}}(t). \tag{3.16}$$

The MOR can now be comprised in one projection operation, that projects the state-vector of the full space to the reduced subspace as $\mathbf{x}_{\text{cme,diag}} = \mathbf{W}_{\text{full}}^{\text{T}} \mathbf{x}_{\text{full}}$ with the projection operator as

$$\mathbf{W}_{\text{full}} = \mathbf{U}\mathbf{Q}_{\text{cme}}. \tag{3.17}$$

Due to the symmetry of all projection operators that are used for the MOR, the resulting reduced system is both stable and passive [40]. The MOR is comprised in Algorithm 1.

Algorithm 1 Model Order Reduction by Corrected Modal Expansion

Require: Non-reduced state-space system $\mathbf{M}_{\text{full,n}}$, desired accuracy θ
1: Compute incomplete eigendecomposition of system matrix as in (3.8)
2: **while** r $> \theta$ **do**
3: Determine snapshots as $(-\omega_i^2 \mathbf{I} - \mathbf{A}_{\text{full}})^{-1} \mathbf{B}_{\text{full}} j\omega_i$
4: Determine new reduced basis after (3.12), (3.13) and (3.14)
5: Determine accuracy r as minimal singular value in (3.12)
6: **end while**
7: Diagonalize System Matrix with state transformation $\mathbf{x}_{\text{cme,diag}} = \mathbf{Q}_{\text{cme}}^{\text{T}} \mathbf{x}_{\text{cme}}$

3.1.4 Concatenation of Impedance Models

Once the reduced order SSMs for all substructures are obtained, they are concatenated to obtain the second order SSM of the full investigated structure. In the following it is shown how the concatenation works in detail, for second order state-space systems, closely following [8] and [42]. However, the derivations are nearly the same for first-order systems. In a first step, the reduced state matrices of all N_{seg} segments are comprised in the block-diagonal matrix $\mathbf{A}_{\text{b}}$

$$\mathbf{A}_{\text{b}} = \text{diag}(\mathbf{A}_{\text{red},1}, \mathbf{A}_{\text{red},2}, \ldots, \mathbf{A}_{\text{red},N_{\text{seg}}}), \tag{3.18}$$

and the reduced input matrices of all N_{seg} segments are comprised in the block-diagonal matrix $\mathbf{B}_{\text{b}}$

$$\mathbf{B}_{\text{b}} = \text{diag}(\mathbf{B}_{\text{red},1}, \mathbf{B}_{\text{red},2}, \ldots, \mathbf{B}_{\text{red},N_{\text{seg}}}). \tag{3.19}$$

In order to get a description of the full, concatenated structure, some states from (3.18) and (3.19) have to be eliminated. Therefore, following [42], the canonically[4]

[4]The word "canonicalïs used here rather for historical reasons, since it was initially mentioned in [42] in the same context. The ordering of the currents and voltages is arbitrary.

ordered modal voltages $\mathbf{v}_{\mathrm{can}}(t)$ and currents $\mathbf{i}_{\mathrm{can}}(t)$, have to be brought in a sorted state $\mathbf{v}_{\mathrm{sort}}(t)$ and $\mathbf{i}_{\mathrm{sort}}(t)$, which results in the same ordering of the state vector. This is done by separating the internal modal voltages $\mathbf{v}_{\mathrm{int}}(t)$ and currents $\mathbf{i}_{\mathrm{int}}(t)$ (i.e. modal voltages and corresponding to ports on cutting planes) from the external modal voltages $\mathbf{v}_{\mathrm{ext}}(t)$ and currents $\mathbf{i}_{\mathrm{ext}}(t)$ (i.e. modal voltages and corresponding to waveguide ports of the full structure) with the help of a permutation matrix[5] $\mathbf{P}_{\mathrm{s}}$

$$\mathbf{i}_{\mathrm{sort}}(t) = \begin{pmatrix} \mathbf{i}_{\mathrm{int}}(t) \\ \mathbf{i}_{\mathrm{ext}}(t) \end{pmatrix} = \mathbf{P}_{\mathrm{s}}^{\mathrm{T}}\, \mathbf{i}_{\mathrm{can}}(t), \tag{3.20}$$

$$\mathbf{v}_{\mathrm{sort}}(t) = \begin{pmatrix} \mathbf{v}_{\mathrm{int}}(t) \\ \mathbf{v}_{\mathrm{ext}}(t) \end{pmatrix} = \mathbf{P}_{\mathrm{s}}^{\mathrm{T}}\, \mathbf{v}_{\mathrm{can}}(t). \tag{3.21}$$

The described permutation matrix $\mathbf{P}_{\mathrm{s}}$ has one coefficient equal to one in each row and column, while the rest of the matrix is zero. It is important to mention that, for later convenience the permutation matrix also sorts the internal currents and voltages in a way that for each internal terminal, the connected internal terminal from the next segments is directly below it, in the sorted order. Applying this permutation to the state-space system of the concatenated structure gives

$$\frac{\mathrm{d}^2}{\mathrm{d}t^2}\mathbf{x}_{\mathrm{b}}(t) = \mathbf{A}_{\mathrm{b}}\mathbf{x}_{\mathrm{b}}(t) + \underbrace{\mathbf{B}_{\mathrm{b}}\,\mathbf{P}_{\mathrm{s}}}_{\bar{\mathbf{B}}_{\mathrm{b}}} \frac{\mathrm{d}}{\mathrm{d}t}\mathbf{i}_{\mathrm{sort}}(t), \tag{3.22}$$

$$\mathbf{v}_{\mathrm{sort}}(t) = \underbrace{\mathbf{P}_{\mathrm{s}}^{\mathrm{T}}\,\mathbf{B}_{\mathrm{b}}^{\mathrm{T}}}_{\bar{\mathbf{B}}_{\mathrm{b}}^{\mathrm{T}}}\mathbf{x}_{\mathrm{b}}(t), \tag{3.23}$$

with the bar on $\bar{\mathbf{B}}_{\mathrm{b}}$ indicating the sorted input matrix which can be split up further using (3.20) and (3.21) to

$$\bar{\mathbf{B}}_{\mathrm{b}} = \left(\bar{\mathbf{B}}_{\mathrm{b},1}\ \bar{\mathbf{B}}_{\mathrm{b},2}\right). \tag{3.24}$$

This separation of the input matrix to a part that acts on the internal states $\bar{\mathbf{B}}_{\mathrm{b},1}$ and a part that acts on the external states $\bar{\mathbf{B}}_{\mathrm{b},2}$ is used to reformulate (3.22) and (3.23) as

$$\frac{\mathrm{d}^2}{\mathrm{d}t^2}\mathbf{x}_{\mathrm{b}}(t) = \mathbf{A}_{\mathrm{b}}\mathbf{x}_{\mathrm{b}}(t) + \bar{\mathbf{B}}_{\mathrm{b},1}\frac{\mathrm{d}}{\mathrm{d}t}\mathbf{i}_{\mathrm{int}}(t) + \bar{\mathbf{B}}_{\mathrm{b},2}\frac{\mathrm{d}}{\mathrm{d}t}\mathbf{i}_{\mathrm{ext}}(t), \tag{3.25}$$

$$\mathbf{v}_{\mathrm{int}}(t) = \bar{\mathbf{B}}_{\mathrm{b},1}^{\mathrm{T}}\mathbf{x}_{\mathrm{b}}(t), \tag{3.26}$$

$$\mathbf{v}_{\mathrm{ext}}(t) = \bar{\mathbf{B}}_{\mathrm{b},2}^{\mathrm{T}}\mathbf{x}_{\mathrm{b}}(t). \tag{3.27}$$

[5] The original literature [8] refers to the permutation matrix simply as $\mathbf{P}$ instead of $\mathbf{P}_{\mathrm{s}}$.

The internal currents in (3.25) are linearly dependent for concatenated segments[6] by Kirchhoff's current law. It states that at each node, the sum of all currents is zero. Hence if a current flows out of an internal port, it has to flow into the connected internal port of the attached segment, making these two states linearly dependent. In order to remove those states the matrix $\mathbf{F}$ is defined as a block-diagonal of $(1, -1)^{\mathrm{T}}$

$$\mathbf{F} = \operatorname{diag}\left(\begin{pmatrix} 1 \\ -1 \end{pmatrix}, \ldots, \begin{pmatrix} 1 \\ -1 \end{pmatrix}\right). \tag{3.28}$$

If not for the earlier mentioned sorting of the internal state such that linearly dependent currents are located in adjacent columns, this matrix would not be block diagonal. The matrix $\mathbf{F}$ is further used to remove those linearly dependent states of the internal current vector with

$$\mathbf{i}_{\mathrm{int}}(t) = \mathbf{F}\,\hat{\mathbf{i}}_{\mathrm{int}}(t). \tag{3.29}$$

In this case the hat from $\hat{\mathbf{i}}_{\mathrm{int}}(t)$ indicates the redundancy-free current vector. For the internal voltages, Kirchhoff's voltage law applies, which states that the sum of voltages over a closed loop is zero. Hence the modal voltage on connected, internal terminals has to be equal. Using the matrix $\mathbf{F}$ this results in

$$\mathbf{F}^{\mathrm{T}}\mathbf{v}_{\mathrm{int}}(t) = \mathbf{F}^{\mathrm{T}}\bar{\mathbf{B}}_{\mathrm{b},1}^{\mathrm{T}}\mathbf{x}_{\mathrm{r}}(t) = \mathbf{0}. \tag{3.30}$$

Now (3.25) is multiplied by $\mathbf{F}^{\mathrm{T}}\bar{\mathbf{B}}_{\mathrm{b},1}^{\mathrm{T}}$ from the left-hand side under consideration of (3.29)

$$\begin{aligned} \frac{\mathrm{d}^2}{\mathrm{d}t^2}\underbrace{\mathbf{F}^{\mathrm{T}}\bar{\mathbf{B}}_{\mathrm{b},1}^{\mathrm{T}}\mathbf{x}_{\mathrm{b}}(t)}_{\mathbf{0}} = \mathbf{0} &= \mathbf{F}^{\mathrm{T}}\bar{\mathbf{B}}_{\mathrm{b},1}^{\mathrm{T}}\mathbf{A}_{\mathrm{b}}\mathbf{x}_{\mathrm{b}}(t) \\ &\quad + \mathbf{F}^{\mathrm{T}}\bar{\mathbf{B}}_{\mathrm{b},1}^{\mathrm{T}}\bar{\mathbf{B}}_{\mathrm{b},1}\,\mathbf{F}\frac{\mathrm{d}}{\mathrm{d}t}\hat{\mathbf{i}}_{\mathrm{int}}(t) + \mathbf{F}^{\mathrm{T}}\bar{\mathbf{B}}_{\mathrm{b},1}^{\mathrm{T}}\bar{\mathbf{B}}_{\mathrm{b},2}\,\mathbf{F}\frac{\mathrm{d}}{\mathrm{d}t}\mathbf{i}_{\mathrm{ext}}(t). \end{aligned} \tag{3.31}$$

In order to replace the internal currents in (3.25), (3.31) is resolved for $\frac{\mathrm{d}}{\mathrm{d}t}\hat{\mathbf{i}}_{\mathrm{int}}(t)$ which gives

$$\begin{aligned} \frac{\mathrm{d}}{\mathrm{d}t}\mathbf{i}_{\mathrm{int}}(t) = &- \left[\mathbf{F}^{\mathrm{T}}\bar{\mathbf{B}}_{\mathrm{b},1}^{\mathrm{T}}\bar{\mathbf{B}}_{\mathrm{b},1}\,\mathbf{F}\right]^{-1}\mathbf{F}^{\mathrm{T}}\bar{\mathbf{B}}_{\mathrm{b},1}^{\mathrm{T}}\mathbf{A}_{\mathrm{b}}\mathbf{x}_{\mathrm{b}}(t) \\ &- \left[\mathbf{F}^{\mathrm{T}}\bar{\mathbf{B}}_{\mathrm{b},1}^{\mathrm{T}}\bar{\mathbf{B}}_{\mathrm{b},1}\,\mathbf{F}\right]^{-1}\mathbf{F}^{\mathrm{T}}\bar{\mathbf{B}}_{\mathrm{b},1}^{\mathrm{T}}\bar{\mathbf{B}}_{\mathrm{b},2}\,\mathbf{F}\frac{\mathrm{d}}{\mathrm{d}t}\mathbf{i}_{\mathrm{ext}}(t). \end{aligned} \tag{3.32}$$

[6] This assumes that the structure's cutplane is located at a constant cross section such that the 2D port modes are the same on both segments. In case of a numerical discretization the 2D port-modes are not exactly the same on both sides of the cutplane. It is thus assumed that the discretization is sufficiently accurate.

For further convenience, the idempotent[7] and symmetric matrix $\mathbf{K}$ is introduced as

$$\mathbf{K} = \mathbf{I} - \bar{\mathbf{B}}_{\mathrm{b},1}\,\mathbf{F}\left[\mathbf{F}^{\mathrm{T}}\bar{\mathbf{B}}_{\mathrm{b},1}^{\mathrm{T}}\bar{\mathbf{B}}_{\mathrm{b},1}\,\mathbf{F}\right]^{-1}\mathbf{F}^{\mathrm{T}}\bar{\mathbf{B}}_{\mathrm{b},1}^{\mathrm{T}}. \tag{3.33}$$

This matrix $\mathbf{K}$ is used to replace the internal currents in (3.25)

$$\frac{\mathrm{d}^2}{\mathrm{d}t^2}\mathbf{x}_{\mathrm{b}}(t) = \mathbf{K}\left(\mathbf{A}_{\mathrm{b}}\mathbf{x}_{\mathrm{b}}(t) + \bar{\mathbf{B}}_{\mathrm{b},2}\,\frac{\mathrm{d}}{\mathrm{d}t}\mathbf{i}_{\mathrm{ext}}(t)\right). \tag{3.34}$$

To remove the linearly dependent states, the null-space of $\mathbf{F}^{\mathrm{T}}\bar{\mathbf{B}}_{\mathrm{b},1}^{\mathrm{T}}$ has to be computed

$$\mathbf{M} = \mathrm{Null}(\mathbf{F}^{\mathrm{T}}\bar{\mathbf{B}}_{\mathrm{b},1}^{\mathrm{T}}), \tag{3.35}$$

and is applied to the state-vector

$$\mathbf{x}_{\mathrm{conc}}(t) = \mathbf{K}\mathbf{M}\mathbf{x}_{\mathrm{b}}(t). \tag{3.36}$$

Now the state-vector $\mathbf{x}_{\mathrm{b}}(t)$ in (3.34) is replaced by the redundancy-free state-vector of the concatenated structure $\mathbf{x}_{\mathrm{conc}}(t)$

$$\frac{\mathrm{d}^2}{\mathrm{d}t^2}\mathbf{x}_{\mathrm{conc}}(t) = \underbrace{\mathbf{M}^{\mathrm{T}}\mathbf{K}\mathbf{A}_r\mathbf{K}\mathbf{M}}_{\mathbf{A}_{\mathrm{conc}}}\mathbf{x}_{\mathrm{conc}}(t) + \underbrace{\mathbf{M}^{\mathrm{T}}\mathbf{K}\bar{\mathbf{B}}_{\mathrm{b},2}}_{\mathbf{B}_{\mathrm{conc}}}\,\frac{\mathrm{d}}{\mathrm{d}t}\mathbf{i}_{\mathrm{ext}}(t). \tag{3.37}$$

The same replacement is done for the output equation (3.27)

$$\mathbf{v}_{\mathrm{ext}}(t) = \underbrace{\bar{\mathbf{B}}_{\mathrm{b},2}\mathbf{K}\mathbf{M}}_{\mathbf{B}_{\mathrm{conc}}^{\mathrm{T}}}\mathbf{x}_{\mathrm{conc}}(t). \tag{3.38}$$

The state-space system (3.37) and (3.38) can be further reduced by employing the CME once again for the final system, with the projection operator $\mathbf{W}_{\mathrm{conc}}$. This leads to the final SSM of reduced order, for the concatenated structure

$$\frac{\mathrm{d}^2}{\mathrm{d}t^2}\mathbf{x}_{\mathrm{conc,red}}(t) = \underbrace{\mathbf{W}_{\mathrm{conc}}^{\mathrm{T}}\mathbf{A}_{\mathrm{conc}}\mathbf{W}_{\mathrm{conc}}}_{\mathbf{A}_{\mathrm{conc,red}}}\mathbf{x}_{\mathrm{conc,red}}(t) + \underbrace{\mathbf{W}_{\mathrm{conc}}^{\mathrm{T}}\bar{\mathbf{B}}_{\mathrm{conc}}}_{\mathbf{B}_{\mathrm{conc,red}}}\,\frac{\mathrm{d}}{\mathrm{d}t}\mathbf{i}_{\mathrm{ext}}(t) \tag{3.39}$$

$$\mathbf{v}_{\mathrm{ext}}(t) = \underbrace{\bar{\mathbf{B}}_{\mathrm{conc}}^{\mathrm{T}}\mathbf{W}_{\mathrm{conc}}}_{\mathbf{B}_{\mathrm{conc,red}}^{\mathrm{T}}}\mathbf{x}_{\mathrm{conc,red}}(t). \tag{3.40}$$

the indices for this final system e.g. in $\mathbf{A}_{\mathrm{conc,red}}$ indicate that this matrix originates from the concatenated, reduced system. The system can be comprised as

[7] $\mathbf{K}^2 = \mathbf{K}$

$$\mathbf{M}_{\mathrm{conc,red}} = \left[\begin{array}{c|c} \mathbf{W}_{\mathrm{conc}}^{\mathrm{T}}\mathbf{A}_{\mathrm{conc}}\mathbf{W}_{\mathrm{conc}} & \mathbf{W}_{\mathrm{conc}}^{\mathrm{T}}\bar{\mathbf{B}}_{\mathrm{conc}} \\ \hline \left(\mathbf{W}_{\mathrm{conc}}^{\mathrm{T}}\bar{\mathbf{B}}_{\mathrm{conc}}\right)^{\mathrm{T}} & \mathbf{0} \end{array}\right]. \tag{3.41}$$

This system is used throughout this thesis whenever the RF-properties of a structure have to be comprised in an efficient manner.

3.1.5 Projection to Initial, Non-Reduced Space

SSC generally allows the computation of fields in a comparably simple post-processing step. For a given excitation (e.g. by a modal current), the state-vector of the reduced model $\mathbf{x}_{\mathrm{conc,red}}$ is computed. With the stored projection matrix, the state-vector is projected back to the original space, thus computing the field-distribution in the initial, non-reduced space. Due to the fact that several projections are employed and the original space is decomposed into several geometrical subspaces this is far from trivial. The reconstruction of the field distribution is discussed in the following.

Firstly, for a given excitation the state-vector of the space of the concatenated reduced order SSM $\mathbf{M}_{\mathrm{conc,red}}$ (system (3.39) and (3.40)) has to be projected to the space of the concatenated SSM $\mathbf{M}_{\mathrm{conc}}$ (system (3.37) and (3.37)) using the projection operator $\mathbf{W}_{\mathrm{conc}}$. This state vector consists of the state vectors of the reduced order models of the segments (system (3.15) and (3.16)) as

$$\mathbf{W}_{\mathrm{conc}}^{\mathrm{T}}\mathbf{x}_{\mathrm{conc,red}} = \mathbf{x}_{\mathrm{conc}} = \left[\mathbf{x}_{\mathrm{red,1}},\ \ldots,\ \mathbf{x}_{\mathrm{red,N_{seg}}}\right]^{\mathrm{T}}. \tag{3.42}$$

The state-vectors of all N_{seg} segments all have to be projected back to the non-reduced space of their regarding segment. The state-vector $\mathbf{x}_{\mathrm{red,n}}$ of the n-th segment can be projected to initial, non-reduced space of the n-th subdomain by the projection operator $\mathbf{W}_{\mathrm{full,n}}$ originating from the MOR of the non-reduced SSM of the n-th subdomain as

$$\mathbf{W}_{\mathrm{full,n}}^{\mathrm{T}}\mathbf{x}_{\mathrm{red,n}} = \mathbf{x}_{\mathrm{full,n}}. \tag{3.43}$$

The state-vectors of the non-reduced state-space models of the segments are the electric fields in said segments, according to system (3.5) and (3.6). This projection has to be carried out for all segments. The resulting state-vectors of the segments can be summed up to the full state-vector (i.e. the fields) in the full non-reduced, non-decomposed space. The latter described process is further highlighted in Fig. 3.2.

3.1.6 Scattering Formulation

In some cases it is more advantageous to use a so-called *scattering formulation* instead of an impedance formulation (which was used up until this point of the thesis). While an impedance formulation uses modal currents and voltages as input

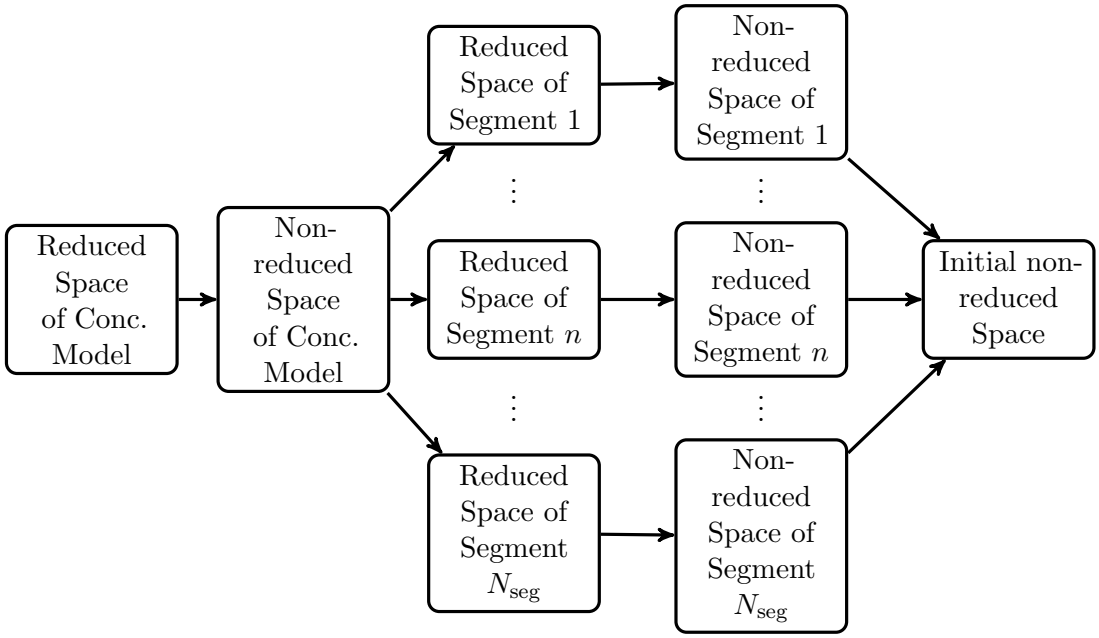

Abbildung 3.2: This picture shows the different spaces between which the computed state vector of the reduced and concatenated space has to be projected to get the state vector of the initial non-reduced space. One starts with the state vector $\mathbf{x}_{\text{conc,red}}$ of the concatenated and reduced SSM $\mathbf{M}_{\text{conc,red}}$. Using the projection operator $\mathbf{W}_{\text{conc}}$ this state vector is projected into the concatenated space with $\mathbf{W}_{\text{conc}}^{\text{T}}\,\mathbf{x}_{\text{conc,red}} = \mathbf{x}_{\text{conc}}$. This state vector consists of the state vectors of the reduced order models of the segments. The state-vectors of all N_{seg} segments all have to be projected back to the non-reduced space of their regarding segment. The state-vector $\mathbf{x}_{\text{red,n}}$ of the n-th segment can be projected to initial, non-reduced space of the n-th subdomain by $\mathbf{W}_{\text{full,n}}^{\text{T}}\mathbf{x}_{\text{red,n}} = \mathbf{x}_{\text{full,n}}$. The state-vector of the initial, non-reduced space is simply the addition of all state-vectors of the initial, non-reduced space of the decomposed subdomains (which are only non-zero in their regarding subdomain).

and output quantities for the SSM, a scattering formulation uses normalised, incident wave-amplitudes $\mathbf{a}_{\text{ext}}(t)$

$$\mathbf{a}_{\text{ext}}(t) = \frac{1}{2}\left(\mathbf{D}_z^{-\frac{1}{2}}\mathbf{v}_{\text{ext}}(t) + \mathbf{D}_z^{\frac{1}{2}}\mathbf{i}_{\text{ext}}(t)\right), \tag{3.44}$$

as input quantities and normed scattered wave amplitudes $\mathbf{b}_{\text{ext}}(t)$

$$\mathbf{b}_{\text{ext}}(t) = \frac{1}{2}\left(\mathbf{D}_z^{-\frac{1}{2}}\mathbf{v}_{\text{ext}}(t) - \mathbf{D}_z^{\frac{1}{2}}\mathbf{i}_{\text{ext}}(t)\right), \tag{3.45}$$

as output quantities with the diagonal matrix $\mathbf{D}_z$, containing the wave impedances of the corresponding 2D modes (see (2.39) and (2.41)). After some rearrangement of (3.39) and (3.40) this leads to the system

$$\frac{\mathrm{d}^2}{\mathrm{d}t^2}\mathbf{x}_{\text{s}}(t) = \underbrace{\mathbf{A} - \mathbf{B}\mathbf{D}_z^{-1}\mathbf{B}^{\text{T}}}_{\mathbf{A}_{\text{s}}}\mathbf{x}_{\text{s}}(t) + \underbrace{2\mathbf{B}\mathbf{D}_z^{-\frac{1}{2}}}_{\mathbf{B}_{\text{s}}}\frac{\mathrm{d}}{\mathrm{d}t}\mathbf{a}_{\text{ext}}(t), \tag{3.46}$$

$$\mathbf{b}_{\text{ext}}(t) = \underbrace{\mathbf{D}_z^{-\frac{1}{2}}\mathbf{B}^{\text{T}}}_{\mathbf{B}_{\text{s}}^{\text{T}}}\mathbf{x}_{\text{s}}(t) - \underbrace{\mathbf{I}}_{-\mathbf{D}_{\text{s}}}\frac{\mathrm{d}}{\mathrm{d}t}\mathbf{a}_{\text{ext}}(t). \tag{3.47}$$

The matrices of the impedance formulation have no subindices in (3.46) and (3.47) since the conversion holds true for any impedance formulation used in this thesis, reduced or not. The indices e.g. in $\mathbf{A}_{\text{s}}$ indicate that this matrix originates from a scattering formulation. Scattering formulations have the advantage that certain properties like the incident and scattered, normalised wave amplitudes are measurable at high frequencies[8]. A well established, measurable quantity for RF-Structures are the so-called *scattering-parameters*. They can be computed via the transmission function of the system (3.46) and (3.47) transformed into frequency domain as

$$\mathbf{S}(s) = s\mathbf{B}_{\text{s}}^{\text{T}}\left(s^2\mathbf{I} - \mathbf{A}_{\text{s}}\right)^{-1}\mathbf{B}_{\text{s}} + s\mathbf{D}_{\text{s}}. \tag{3.48}$$

These scattering parameters are used later to compare measurements with the results acquired by SSC in Chapter 5.2.

3.2 Implementation

For arbitrary structures the described algorithms for SSC can not be employed without approximations. Therefore, in this thesis a collection of software was implemented, that allows for the effective and automated solution of the Helmholtz-equation of large, complex SRF structures using FIT and SSC, based on the theory presented in Chapter 3.1. Furthermore, an implementation using FEM has been conducted in

[8] In contrast to modal voltages and currents, which are rather a mathematical concept and are not measurable at high frequencies.

this thesis. The FEM implementation is not used in this thesis due to performance issues and rather serves as a proof of concept. The decision for FIT was, that some major parts that would have to be implemented for SSC, were already present in the commercial software CST MWS. Unfortunately the export of such results, is solely possible for FIT and hexahedral grids in CST MWS, but not for tetrahedral grids. In this section, some implementation details are further explained and justified. The steps that had to be implemented were: the construction of the unreduced SSM, the MOR, concatenation and post processing as highlighted in Alg. 2.

Algorithm 2 Computation of electromagnetic fields and secondary quantities in an arbitrary domain with SSC

Require: CAD Model of the investigated structure
1: Decompose structure into N_{seg} substructures
2: **for** $i = 1 \rightarrow N_{\text{seg}}$ **do**
3: Determine unreduced FIT system of i-th substructure with Algorithm 3
4: MOR for i-th substructure with Algorithm 4
5: **end for**
6: Determine matrices $\mathbf{P}_{\text{s}}$ according to (3.20) and $\mathbf{F}$ according to (3.28)
7: Concatenation of reduced order models (ROMs) of segments after (3.37) and (3.38)
8: Further MOR of concatenated system with Algorithm 4
9: Post processing

The steps of this algorithm and their implementation are explained in this section.

3.2.1 Domain Decomposition

While the theoretical aspects of the decomposition were discussed in Chapter 3.1.1, this subsection focuses on the practical implementation. The full geometry is generally available in form of a CAD model. This CAD model has to be decomposed into CAD models of all substructures as shown in Fig. 3.1. The decomposition is the only part of the entire algorithm that is not fully automated. This has several reasons. On one hand, the decomposition takes some practice/expert-knowledge in order to find a suitable decomposition. Furthermore, some ROMs of substructures might be readily available. The third point is, that the mathematical formulation and automation of the decomposition is rather complicated and hardly contributes to the usability of the code. A limiting condition is, as mentioned earlier in 3.1.4, that the 2D modes on both side of the decomposition plane have to be the same. Therefore, a cut is only possible at locations with constant cross section. A technological limitation of the current CST MWS implementation is that cutting planes

have to be aligned with a euclidean coordinate system[9]. Furthermore, the cutting planes (and all waveguide-ports) have to have a constant cross section for a certain distance orthogonal to the cutting-surface[10].

The goal of the decomposition is to have a good performance regarding the computational time. There are generally two influential factors, the number of 2D modes M_{2D} needed at the cutting plane to ensure a sufficient accuracy and the number of 3D modes N_{3D} inside the domain needed to ensure a sufficient accuracy. Another way to increase the performance is to find decompositions such that symmetry-boundary conditions can be applied or substructures can be treated entirely analytical. Especially in the context of accelerator physics where the structures are often repetitive, it is of special interest to find a decomposition such that a model can be reused several times e.g. for a cavity. In the context of accelerator physics often decompositions are reliable that use the logical components of the accelerating structure, e.g. a decomposition of a cryomodule into couplers, cavities and beampipes.

3.2.2 Construction of the Unreduced SSM Using FIT

For each substructure that was determined during the decomposition in Chapter 3.2.1, the unreduced SSM (3.5) and (3.6) has to be determined, which can be later reduced and concatenated. As mentioned earlier, in most cases an analytical description of the electromagnetic fields inside an arbitrary structure is rarely feasible. Therefore, FIT is used to discretize said structure which is explained in the following.

Firstly, a CAD model of each segment has to be provided by the decomposition. This CAD model marks the computational domain in which Maxwell's equations have to be discretized by FIT. This is done using CST MWS in a combination with several scripts written in Matlab, Python and Visual Basic for Applications (VBA). Everything is controlled from Matlab ®, which calls the other scripts[11]. Unfortunately, a bilateral exchange of data between CST MWS and Matlab is not possible, making it a common practice to simply write data to *.txt* files and let CST MWS read said files via a VBA script [43]. So in a first step, a *.txt* file is generated by Matlab containing parameters that are needed for the CST MWS solver (e.g. the mesh density, solver accuracy, boundary conditions, port-information and/or structural parameters). The location of the waveguide-ports is determined either by the application itself or by the decomposition. Matlab then opens CST MWS and executes a VBA macro in CST MWS. This macro reads the stated information from the *.txt* file, creates the structure, creates waveguide-ports with the

[9] A limitation that is not given in the FEM implementation.

[10] The specific distance depends on the mesh density. This drawback is also not present in the FEM implementation.

[11] For the convenience of the reader, the ® symbol is omitted for Matlab from hereon.

desired number of 2D modes for each port, sets the correct boundary conditions[12] and then computes the $M_{2\mathrm{D}}$ 2D-eigenmodes in the port surfaces and assembles the desired 3D FIT matrices.

After that, Matlab executes a compiled C++ function which can import matrices from CST MWS via a *Dynamic-link library* (dll) [44][13]. This framework is used to read the desired 3D FIT matrices as well as the solution to the 2D Helmholtz-equation (2.25) in the port surfaces: $\mathbf{L}_{\mathrm{t,m}}(\mathbf{r}_{\mathrm{t}})$ and $k_{\mathrm{t,m}}$. The solutions of said equation which are obtained by a discretization in FIT are further denoted as $\mathtt{L}_{\mathrm{t,m}}(\mathbf{r}_{\mathrm{t}})$ and $\mathtt{k}_{\mathrm{t,m}}$.

The exported FIT-matrices as well as the solution of the 2D Helmholtz-equation allows for the discretization of the system (3.5) and (3.6) as discussed in detail in [40]. Using the employed nomenclature in Chapter 2.3 the desired system can be outlined in the following manner

$$\frac{\mathrm{d}^2}{\mathrm{d}t^2} \underbrace{\widehat{\mathbf{e}}}_{\mathtt{x}_{\mathrm{full,n,FIT}}} = \underbrace{\mathtt{M}_\epsilon^{-\frac{1}{2}} \mathtt{C}^{\mathrm{T}} \mathtt{M}_\mu^{-1} \mathtt{C} \mathtt{M}_\epsilon^{-\frac{1}{2}}}_{\mathtt{A}_{\mathrm{full,n,FIT}}} \widehat{\mathbf{e}} - \frac{\mathrm{d}}{\mathrm{d}t} \underbrace{\mathtt{M}_\epsilon^{-\frac{1}{2}} \mathtt{R}}_{\mathtt{B}_{\mathrm{full,n,FIT}}} \mathbf{i}(t), \tag{3.49}$$

$$\mathbf{v}(t) = \underbrace{\mathtt{R}^{\mathrm{T}} \mathtt{M}_\epsilon^{-\frac{1}{2}}}_{\mathtt{B}^{\mathrm{T}}_{\mathrm{full,n,FIT}}} \widehat{\mathbf{e}}. \tag{3.50}$$

with the FIT input matrix $\mathtt{R}$ holding the discrete solutions of the 2D Helmholtz-equations inside the port surface projected onto the discrete 3D space. This formulation assumes that there is no grid dispersion [40], i.e. that the grid is sufficiently fine. For a meshed structure with $\mathtt{N}_P$ nodes, the resulting size of the unreduced state-space matrices are $\mathtt{A}_{\mathrm{full,n,FIT}}$ with $\mathtt{A}_{\mathrm{full,n,FIT}} \in \mathbb{R}^{3\cdot\mathtt{N}_P \times 3\cdot\mathtt{N}_P}$ and the input matrix of the second order state-space system $\mathtt{B}_{\mathrm{full,n,FIT}}$ with $\mathtt{B}_{\mathrm{full,n,FIT}} \in \mathbb{R}^{M_{2\mathrm{D}} \times 3\cdot\mathtt{N}_P}$ and $\mathtt{C}_{\mathrm{full,n,FIT}}$ with $\mathtt{C}_{\mathrm{full,n,FIT}} \in \mathbb{R}^{3\cdot\mathtt{N}_P \times M_{2\mathrm{D}}}$. The system is further denoted as $\mathtt{M}_{\mathrm{full,n,FIT}}$

$$\mathtt{M}_{\mathrm{full,n,FIT}} = \left[\begin{array}{c|c} \mathtt{M}_\epsilon^{-\frac{1}{2}} \mathtt{C}^{\mathrm{T}} \mathtt{M}_\mu^{-1} \mathtt{C} \mathtt{M}_\epsilon^{-\frac{1}{2}} & -\mathtt{M}_\epsilon^{-\frac{1}{2}} \mathtt{R} \\ \hline \left(\mathtt{M}_\epsilon^{-\frac{1}{2}} \mathtt{R}\right)^{\mathrm{T}} & 0 \end{array}\right]. \tag{3.51}$$

When assembling the system (3.51), one first has to assemble the desired FIT matrices, i.e. $\mathtt{M}_\epsilon, \mathtt{M}_\mu$ and $\mathtt{C}$ as well as compute the solutions to the discretized Helmholtz-equation in the port surfaces, $\mathtt{L}_{\mathrm{t,m}}(\mathbf{r}_{\mathrm{t}})$ and $\mathtt{k}_{t,n}$. In the next step, the curl matrix needs to be changed to incorporate the correct boundary conditions (PMC at every port surface). Secondly, the matrix $\mathtt{R}$ has to be assembled from the discrete solutions

[12] As discussed in Chapter 3.1.2 a PMC boundary has to be set in each port-surface.

[13] Unfortunately, this script is only able to export FIT-matrices for hexahedral meshes. This becomes one of the main limiting factors for SSC (though it is purely technological and is fixed by the FEM implementation).

of the 2D Helmholtz-equation. Therefore, the 2D solutions are projected on the 3D discretized space. The practical construction of the non-reduced, discretized models is comprised in Algorithm 3.

Algorithm 3 Construction of n-th non-reduced SSM $\mathtt{M}_{\mathrm{full,n,FIT}}$

Require: CAD Model of the investigated structure

1: Discretize structure with mesh and assemble FIT matrices $\mathtt{M}_\epsilon, \mathtt{M}_\mu$ and $\mathtt{C}$
2: Obtain solution of 2D Helmholtz equation in port surfaces, $\mathtt{L}_{\mathrm{t,m}}(\mathbf{r}_\mathrm{t})$ and $\mathtt{k}_{t,n}$
3: Set boundary condition to $\mathtt{C}$
4: Assemble $\mathtt{R}$ and $\mathtt{M}_{\mathrm{full,n,FIT}}$

3.2.3 MOR of Unreduced State-Space System

The MOR was implemented by T. Flisgen in [8]. It employs the formalism described in Algorithm 1 to an efficient code. As input it receives the unreduced SSM, i.e. the FIT system $\mathtt{M}_{\mathrm{full,n,FIT}}$ (3.51), as well as the desired frequency domain and the number of desired 3D modes N_{3D}[14]. The MOR returns the reduced state-space model $\mathtt{M}_{\mathrm{red,n,FIT}}$ and the according projection matrix. The entire MOR is implemented in Matlab. The key requirements, the eigenmode solver and the solution of the frequency excitation, could also be executed by CST MWS but Matlab was chosen due the improved performance [45]. This subsection discusses some important properties of the implementation.

Firstly, one has to compute the incomplete eigendecomposition of the system-matrix $\mathtt{A}_{\mathrm{full,n,FIT}}$. This is done for a small system (e.g. when the concatenated system is reduced again in order as in (3.39) and (3.40)) using a direct solver[15] with LAPACK. For large systems as in (3.49) and (3.50) an iterative algorithm is used. In this case Matlab uses a precompiled version of ARPACK, a FORTRAN77 library which is especially used for large, sparse eigenvalue problems if few, small eigenvalues are needed [46] and employs the implicit restarted Arnoldi method.

For the computation of the snapshots, one has to solve the linear system of equations (3.10) of the size of the number of DOFs in the state-vector. This is solved using the symmetric LQ method for sparse matrices [47]. As initial guess one can use the solution obtained by the reduced order model and project it's solution back to the non-reduced space which reduces the number of iterations needed.

[14] As mentioned earlier, there is no straightforward way to approximate the required number of 3D modes. In this thesis the number is chosen by experience.

[15] A direct eigensolver obtains all solutions, while an iterative solver is generally only effective when a few solutions are required.

3.2.4 Concatenation of Reduced Order Models

The concatenation is (as most other parts) fully automated. Therefore, one needs a script that automatically generates the permutation-matrix $\mathbf{P}_\mathrm{s}$ according to (3.20) and $\mathbf{F}$ according to (3.28). After generating theses matrices, the reduced state-space system of the full structure is generated according to (3.37) - (3.38). The resulting system is then again reduced in its order by the MOR script which gives the system (3.39)-(3.40). The additional reduction is not mandatory but can further improve the performance.

3.2.5 Post Processing

The post processing consists of the computation of several secondary quantities like r/Q , Q_ext and the visual representation of the fields and secondary quantities. Due to the size of the computed fields the post processing is far from trivial. As an example, in the first application of Chapter 5 in this thesis, the BESSY$^\mathrm{VSR}$ cryomodule is investigated and discretized using SSC with roughly 30 Mio. DOFs. By default MATLAB uses double precision floats in each element of a matrix, which allocates 64 bits (i.e. 8 bytes) per element. For this example, SSC finds 1576 eigenmodes. Hence, loading all eigenmodes into the memory would need roughly 400 GB of RAM and is beyond the scope of a standard workstation computer. Therefore, the treatment of the fields is done separately (meaning subsegment per subsegment). The correctly weighted eigenmodes are stored using the .vtk format for all eigenmodes of the full structure. A Python script later generates the field-plots using Paraview [48] for all eigenmodes.

3.3 Analytical Example and Comparison to other Methods

3.3.1 Analytical Example

After discussing the implementation of SSC with FIT, this chapter compares the numerically obtained solution for a test-problem with its analytical solution, as well as the straight-forward solution with FIT (without employing SSC). Of special interest is the accuracy as well as the convergence order. As analytical example, the solution of the Helmholtz-equation for the electric field (see (2.21)) in a box of PEC is chosen. The box is closed with a PMC boundary in positive and negative z-direction, is 80 mm wide, 40 mm high and 420 mm long (in z-direction, which is further referred to as longitudinal direction). All other boundaries are PEC. This structure is depicted in Fig. 3.3. Firstly, the Helmholtz-equation is solved analytically for the

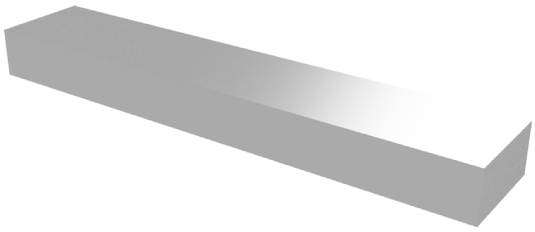

Abbildung 3.3: This picture shows the structure for which the Helmholtz-equation of the electric field is solved analytically. The box is 80 mm wide, 40 mm high and 420 mm long (in z-direction, which is further referred to as longitudinal direction). In both longitudinal boundaries a PMC boundary condition is chosen. All other boundaries are PEC.

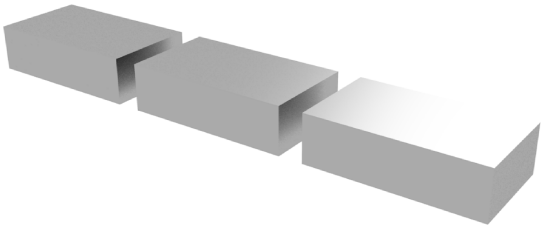

Abbildung 3.4: This picture shows the decomposition that is used for the SSC for the test-structure depicted in Fig. 3.3. The box is decomposed into three equal parts, a box with a length of 140 mm. For plot purposes the separation is exaggerated and the computation is done, such that the substructures touch at the waveguide ports.

box[16]. Furthermore, the Helmholtz-equation is solved in the same domain, using FIT (incorporated in CST MWS 2017[17]) and SSC using FIT (with the processing of the models as described in Chapter 3.2) where the structure is decomposed into three boxes with the same length in z-direction, as shown in Fig. 3.4. In the following, both the resonant frequencies (derived from the solutions of the Helmholtz-equation) and field-distributions are to be computed using the different methods in order to show the functionality of the implemented code and the order of convergence of the numerical solutions regarding the mesh-density. It should be noted that for both approaches the adaptive mesh refinement was disabled to allow for a better control of the number of DOFs.

Firstly, in Fig. 3.5 the relative error of the mode with the lowest resonance frequency[18] is depicted, in dependency on the DOFs of the discretization. It compares the error of a plain FIT discretization (as employed in CST MWS) with the error of the discretization of SSC in combination with FIT (computed by the framework

[16]For the sake of simplicity, the analytical solution is not derived in this thesis since there is a lot of literature outlining the solution, e.g. [24].

[17]The current implementation was tested with the CST MWS versions from 2014 - 2017.

[18]The described investigation was conducted for the first few modes but for simplicity only the first mode is shown.

described in Section 3.2). It can be seen that for both discretizations, the error decreases, as the number of DOFs increases. Also the order of convergence as well as the error for a specific number of DOFs is roughly the same.

Secondly, in Fig. 3.6 the field of an arbitrary mode is compared to the analytical solution on an axis through the middle of the structure. For comparison, the $TM_{1,0,3}$ mode is computed using FIT and the combination of FIT and SSC. The results indicate the same conclusion as for the frequency. Generally, SSC does not perturb the underlying order of convergence of FIT and the error for a certain number of DOFs is similar for both approaches.

Furthermore, Fig. 3.7 investigates the scaling of the computational times of the prior computations with the DOFs[19]. The scaling of the computational time is important since it allows the comparison of algorithms for their usefulness to perform computations with a large number of DOFs. From a standard FIT discretization it is expected that the scaling is roughly quadratic (i.e. a doubling in the DOFs, requires four times the computational time on the same hardware), which is confirmed by the results. For SSC, the scaling is comparable to the plain discretization, even though SSC is more than ten times faster.

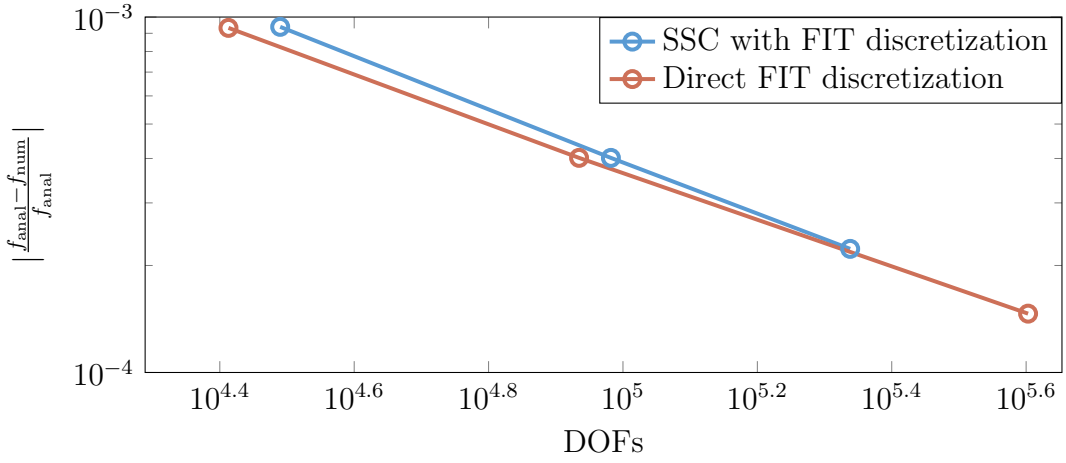

Abbildung 3.5: This picture shows the relative error in the resonance frequency of the first 3D mode of the test-example in Fig. 3.3, in dependence of the number of DOFs of the underlying FIT discretization. The error is compared for the plain FIT discretization and the combination of SSC and FIT.

The same investigation is conducted using SSC with FEM as discretization (as described in [49]). In FEM one has (despite the number of DOFs) another parameter that influences the accuracy, which is the order p of the ansatzfunction. For $p = 1$

[19] A similar investigation was done in Fig. 3.5, but a comparable scaling in the accuracy does not guarantee that the scaling is also the same for the computational time.

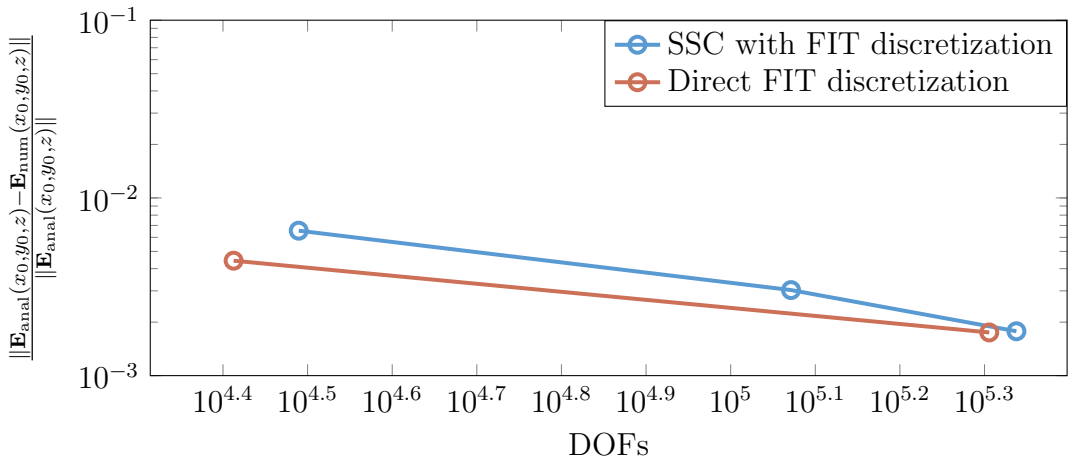

Abbildung 3.6: This picture shows the euclidean norm of the relative error in the field on the beam-axis of the $TM_{1,0,3}$ mode of the test-example in Fig. 3.3, in dependence of the number of DOFs of the underlying FIT discretization. The error is compared for the plain FIT discretization and the combination of SSC and FIT.

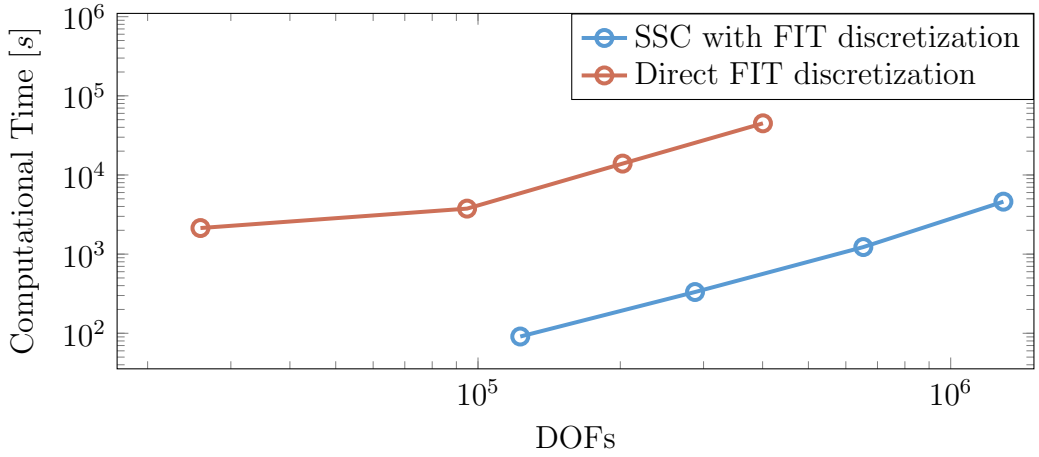

Abbildung 3.7: This picture shows the computational time required to compute all 221 modes in a frequency range from 0-8 GHz inside the box shown in Fig. 3.3 using either SSC with the earlier discussed separation and a plain FIT discretization with CST MWS with a certain number of DOFs. It can be seen that the computational time of the straight forward discretization with FIT, scales a little better than quadratically with the number of DOFs, as expected from the literature [30]. Furthermore, the plot indicates that the implementation of SSC does not change the underlying scaling behavior of the discretization technique for this simple example.

FEM has (theoretically) the same convergence order as FIT. Fig. 3.8 shows the comparison between the FIT and FEM implementation. It can be seen that for SSC

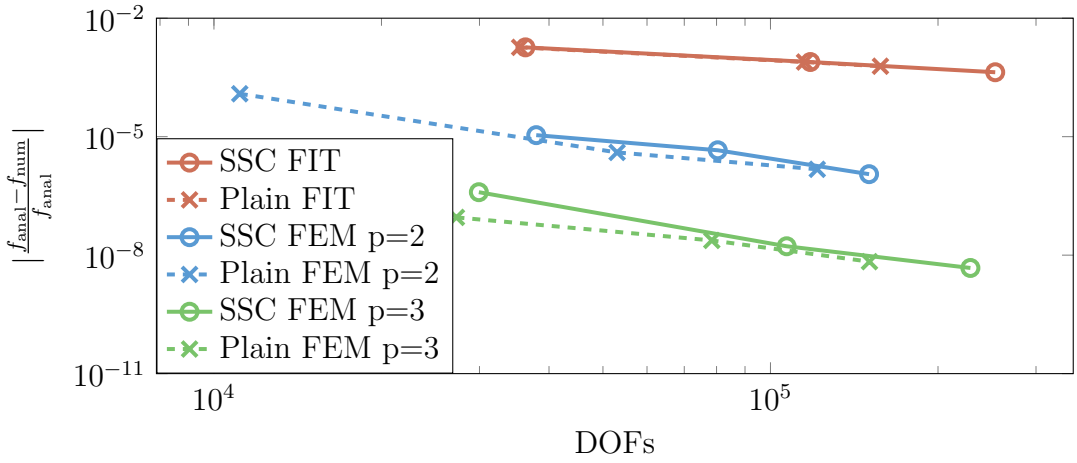

Abbildung 3.8: This picture shows the relative error in the resonance frequency of the first 3D mode of the test-example in Fig. 3.3, in dependence of the number of DOFs of the underlying FIT and FEM discretization. The error is compared for the plain FIT discretization and the combination of SSC and FIT as well as the combination of FEM (with varying order of ansatzfunctions) and SSC and plain FEM. The remarkable alignment of the FIT-based curves is caused by both approaches using the same software for mesh generation (i.e. CST MWS).

with FEM, roughly the same observations can be made as for SSC with FIT. The convergence order remains the same and the combination of SSC and FEM needs fewer DOFs than plain FEM to reach the same accuracy. FEM has the benefit over FIT that the order of ansatzfunctions p can control the convergence order[20]. It is concluded, that there are strong hints that SSC, when combined with a numerical discretization technique, does not perturb the underlying order of convergence of said discretization technique for simple domains.

3.3.2 Discussion of Usability of SSC

After explaining the basics of SSC, one can derive its advantages and disadvantages for the usage in accelerator physics which will be comprised in this section. Of special interest are not only the theoretical aspects but also the practical aspects that result from the implementation. All of these aspects were discussed earlier in this chapter and are comprised in bullet points.

Firstly, SSC has many advantages compared to the straightforward solution of Maxwell's equations:

[20]This statement only holds true for simple domains. The convergence can not always be improved by increasing the order of the ansatzfunctions [27]. Furthermore, it should be noted that theoretically one can also user higher order functions as basis for FIT.

- Employing SSC for the solution of the Helmholtz equation can drastically decrease the required computational time to acquire its solution. Especially, if many modes are desired.
- Structural elements with multiplicity (like e.g. cavities) have to be treated only once, thus decreasing the computational time.
- For simple examples, SSC preserves the convergence order of the underlying discretization scheme.
- SSC is a continuous formulation. This is of advantage from a numerical point-of-view, e.g. regarding the detection of poles in frequency-domain [50].

Due to the inherent eigendecomposition as well as the practical implementation there are also some disadvantages:

- It is assumed that the solution of the Helmholtz equation is readily available or computable in reasonable time and sufficient accuracy. This might not be possible e.g. when a comparably large frequency range is required.
- The location of the cutting planes for the decomposition are theoretically arbitrary, while in practice there are some limitations, e.g. the distance between two decomposition planes or their positioning at constant cross sections.
- The post processing is rather complex and might not be executable on a workstation-computer.
- The required number of 2D modes at the cutting-plane might become impractically high for certain topologies.
- In some cases, the underlying FIT discretization in combination with hexahedral meshes has a worse convergence than FEM combined with tetrahedral meshes, regarding the DOFs

Generally, SSC is very useful for the tasks at hand and thus is used throughout this thesis for the solution of Maxwell's equations in SRF structures.

3.3.3 Comparison with other Domain Decomposition Methods

The idea of domain decomposition methods in order to save computational time is rather old and has been used in Maxwell-related Computational Engineering for more than 40 years e.g. [36], [51], [52] to name just a few. The approaches can be subdivided in three groups as described in [53]. Firstly, there are some modifications of mode-matching techniques, in which the continuity of the fields on arbitrary

interfaces is secured by continuity constraints. Secondly, there are S-parameter based methods and thirdly equivalent-circuit methods in which an equivalent circuit that incorporates the same RF-properties as the investigated structures is computed.

In this chapter SSC is compared to common domain decomposition methods that find application in accelerator physics for the solution of Maxwell's equations. An in-depth explanation of all mentioned techniques would go far beyond the scope of this thesis. For further information it is simply referred to the cited literature. A more in-depth comparison of some of the mentioned techniques is given in [54]. The comparison to the most commonly used methods is given in table 3.1.

An important "milestoneïn using domain-decomposition methods in accelerator physics and general RF-design is the usage of mode-matching by e.g. [55] or [56], or sophisticated variations of it [57]. It generally decomposes the investigated domain into subdomains where an orthogonal decomposition of discrete modes is used to describe the electromagnetic fields. The subdomains are then combined by continuity constraints for the fields on the decomposition planes[21]. Mode Matching works theoretically for arbitrary structures but suffers from the same drawback as SSC, that an explicit eigendecomposition is inevitable which makes computations for comparably large frequency ranges not feasible. Furthermore, mode-matching is restricted to simple geometries.

The *Coupled S-parameter Calculations* (CSC) [42] is the predecessor of SSC and used sampled S-parameters which are concatenated using the same formalism as SSC as described in Chapter 3.1.4. Unfortunately, S-parameters describe only the transmission and reflection behavior of the structures, not their internal states (such as fields), meaning that certain information gets lost. Hence, CSC has been applied with great success for the computation of scattering parameters of large structures as shown in [58], [59] but the computation of all fields is comparably complicated and computationally demanding [60].

The recently proposed *Generalized Scattering Matrix* (GSM) approach [61] is comparable to CSC and uses sampled scattering parameters which are then concatenated for arbitrary topologies. Being S-parameter based, GSM suffers from the same drawbacks regarding field computations as CSC. GSM was recently successfully applied to compute the S-parameters of the Third Harmonic Module of the European XFEL in [62].

A comparably new development is the usage of circuit-theory to describe the electromagnetic behavior of the RF-structures using equivalent-circuits as in [63] and [40] (to name only a few). This has the advantage that for the solution of the resulting PDEs in such circuits, there exist powerful numerical tools in form

[21] The idea is very similar to SSC with the major difference that the continuity constraints in mode-matching are applied on 2D fields, while for SSC they are applied to 1D properties that are derived from fields (i.e. modal voltages and currents).

of so-called *Simulation Programs with Integrated Circuit Emphasis* (SPICE). A major drawback is, that due to the reduction of the RF-structures to a circuit, the field-information is lost, hence only transmission functions and time-domain excitations (e.g. at waveguide-ports) can be evaluated without computing actual field-information.

	SSC	CSC	GSM	Circuit-Theory	Mode-Matching
Time-Domain	✓	✓\✗	✓	✓\✗	✓
Frequency-Domain	✓	✓	✓	✓\✗	✓
MOR	✓	✗	✗	✓	✗
3D Fields	✓	✓\✗	✓\✗	✓\✗	✓

Tabelle 3.1: This table comprises a list of techniques that are used in accelerator physics to reduce the computational effort for the computation of electromagnetic fields in large and complex SRF structures. Furthermore, the techniques are compared in their desirable quantities such as the computation of 3D fields or time domain investigations. In the table the mark ✓ indicates that this property is available for the according technique, while the ✗ mark indicates that it is not available. Furthermore, the ✓\✗ indicates that said property is not fully available, or only with some major computational effort.

4 External Losses in SRF Cavities

Generally, SRF cavities are not lossless as assumed in the introductory chapters of this thesis. In practice, the external losses govern the overall losses. In modern accelerator physics, the computation of said external losses is comparably complicated due to the immense computational demand. This chapter introduces a formalism aiming to close this gap and allow for the computation of external losses of large numbers of modes in complex SRF structures that require many DOFs to be discretized accurately.

This is achieved by a perturbation approach that approximates the fields of lossy resonators as weighted sum of lossless fields, thus shifting the computational burden to a comparably cheap post processing step. The following chapter is structured as follows: Firstly, a rough estimation of the magnitude of the different loss-mechanisms in SRF cavities is given, thus motivating the restriction to external losses. Secondly, the nonlinear eigenvalue problem, whose solution is required for the computation of external losses, as well as previous solution approaches are introduced. Thirdly, the newly proposed approach is derived in detail and several numerical examples are shown to validate said approach.

4.1 Loss Mechanisms in SRF Cavities

There are three different groups of loss mechanisms in charge-free SRF cavities: *dielectric and magnetic losses*, *external losses* and *surface losses* [3]. A convenient mathematical description of such losses of each mode is the so-called quality factor given by

$$Q_n = \frac{2\pi f_n W_{\text{stored},n}}{P_{\text{loss},n}}, \tag{4.1}$$

where n is the mode-number, f_n denotes the resonance-frequency, $W_{\text{stored},n}$ the energy that is stored in the mode and $P_{\text{loss},n}$ the losses of this specific mode. When investigating all three loss mechanisms, the combined losses are governed by the smallest quality factor as they can be roughly approximated by

$$Q_{\text{n}} \approx \frac{1}{\frac{1}{Q_{\text{mat,n}}} + \frac{1}{Q_{\text{ext,n}}} + \frac{1}{Q_{\text{surf,n}}}}, \tag{4.2}$$

with the quality factor for dielectric and magnetic losses $Q_{\text{mat,n}}$, for surface losses $Q_{\text{surf,n}}$ and for external losses $Q_{\text{ext,n}}$. The approximation in (4.2) is only valid if the

frequency of the investigated mode is hardly shifted by the losses, i.e. the losses can be linearly superpositioned.

The cavities are operated at 2 K, at which Niobium has a surface resistance of 10-100 nΩ [1], depending on the material quality. These small surface resistances result in intrinsic quality factors of 10^{10} - 10^{11} [1], so surface losses play hardly any role (assuming the external quality factors are lower). Since the structure is assumed to be evacuated, dielectric and magnetic losses only contribute to the losses significantly if HOM absorbers are considered. Assuming that quality factors resulting from external losses are all below 10^9, this is the main loss mechanism. Therefore, in the problems investigated in this thesis, external losses are considered to be the only loss mechanism and the other two loss mechanisms are neglected. External losses occur when energy is propagating out of the structure through the waveguide ports, as introduced in Chapter 2.1.1. This is especially important for HOMs. These HOMs can lower the beam-quality, deviate the beam from its optimal trajectory or lead to avalanche-like field emission. In order to avoid these effects, the structure is designed in a way that the external losses for the HOMs are very high. Physically speaking, this means that these modes couple well through the HOM couplers outside of the system and their energy is converted to heat. Generally, this is not always possible since not all modes couple strongly to the HOM coupler or beam pipes. Modes with small losses are denoted as *trapped modes* and can be identified by their high quality factors. The identification and quantification of the losses of such trapped modes is an important task in the design of accelerating resonators [36], [55].

Two cases have to be distinguished when dealing with external losses, a *loaded* and a *matched* resonator. For the loaded resonator a lossy material is attached to the waveguide port in a way that some energy gets converted to heat inside the *load*. Examples for this are HOM absorbers [3], or simply termination impedances attached to HOM couplers. For most applications, RF-engineers are not interested in the fields inside the load, but rather the influence of the load in the fields inside the resonator. Hence this can be modeled as an impedance attached to the waveguide, instead of a geometrical object[1]. This impedance might be frequency dependent. The second case for external losses are so called matched resonators. In this case RF-engineers assume, in lack of a better assumption, that either the beam pipe at the waveguide port continues infinitely long without a change of crosssection, or that the beam pipe is perfectly matched with a non-reflective load (which leads to the exact same problem). The matched cavity is so to say, a special case of the loaded cavity. The examples in this thesis are limited to matched cavities. All described algorithms are however able to handle loaded cavities as well, without loss of generality.

[1] This means that neither shape nor exact properties of the load need to be known but only its electromagnetic transmission and reflection properties.

4.2 The Nonlinear Eigenvalue Problem

In this chapter the discretization of the Maxwell equations inside a resonator with matched waveguide ports is considered. While there exist some, rather restricted, approaches to (semi)-analytically solve the latter described physical problem (e.g. [64] and [65]), in the general case it is not possible to find an analytical solution. Therefore, the numerical discretization of Maxwell's equations in lossy SRF structures is generally carried out using an appropriate discretization technique such as FEM, FIT or BEM. Therein, the boundary conditions at the waveguide ports are chosen in such a way that no energy is reflected back into the domain. This is given if the termination impedance is chosen to be the wave impedance of the 2D port mode. These wave impedances depend on the frequency and on the mode type for TE and TM modes, as introduced in Chapter 2.2.5 in (2.39) and (2.41). For TEM modes, the wave impedance is not dependent on the frequency. For these modes, generally the line impedance is chosen as reference, which, in most cases is roughly $50\,\Omega$. The line impedance of a circular coaxial cable can be computed by

$$Z_{\text{Line}}^{\text{TEM}} = \mathrm{Z}_0 \frac{\ln\left(r_a/r_i\right)}{2\pi}, \tag{4.3}$$

where r_a denotes the outer radius and r_i the inner radius of the cable. The line impedance in practical applications is chosen e.g. to allow maximum power transmissions.

This arising problem can generally be formulated in the following manner

$$\mathbf{T}(\lambda)\,\mathbf{x} = \mathbf{0}, \tag{4.4}$$

which is a nonlinear eigenvalue problem [66]. Generally, one is interested in all nontrivial solution-pairs (eigenvalues λ and their regarding eigenvector $\mathbf{x}$) of the arising problem in a certain spectrum. From the eigenvalues of (4.4) one can derive the external quality factors, the loaded frequency as well and from the eigenvector of (4.4) one can derive the electromagnetic fields. For the full solution of the problem, it is inevitable to determine the eigenpairs, not only the eigenvalues. Using either FIT or FEM the problem (4.4) can be rearranged to the following equation

$$\underbrace{\left(\mathbf{K}_1 - \mathbf{K}_2(\lambda) - \lambda\mathbf{K}_3\right)}_{\mathbf{T}(\lambda)}\mathbf{x}(\lambda) = \mathbf{0}, \tag{4.5}$$

with $\mathbf{K}_1$, $\mathbf{K}_2$ and $\mathbf{K}_3$ being problem specific matrices. Particularly interesting is the complex matrix $\mathbf{K}_2(\lambda)$, which makes the problem nonlinear due to its dependency on the eigenvalue itself. Many proposed solutions try to find some approximation for this matrix in order to reduce the computational effort as discussed in the next section.

4.2.1 Simplifications of the NLEVP

The computation of the eigenvalues of the system in (4.5) is generally very hard, sometimes even impossible [67][2]. Therefore in accelerator physics it is a common technique to introduce simplifications for (4.5) in order to produce results with acceptable accuracy. Most of these approaches try to find an approximation of the frequency dependency of the complex-valued matrix $\mathbf{K}_2(\lambda)$ in order to transform the posed problem from a general, nonlinear eigenvalue problem to a simpler one. Some techniques for such simplifications are explained and evaluated in this section. The goal of all simplification approaches is to find a problem that poses a good approximation of (4.5) while employing standard techniques and efficient implementations for linear eigenvalue problems to solve it.

Linearisation

The easiest way to simplify the NLEVP is to linearise it [68]. Generally, this approach assumes that the wave impedance is evaluated at a certain evaluation frequency f_{eval} and further regarded as constant, hence not frequency-dependent, thereby transforming (4.5) to the generalised, linear eigenvalue problem (LEVP)

$$\left(\mathbf{K}_1 - \mathbf{K}_2(f_{\mathrm{eval}})\right)\mathbf{x} = \lambda \mathbf{K}_3 \mathbf{x}. \tag{4.6}$$

As stated in the introduction of this chapter, the LEVP is generally easier to solve. This solution might give reasonable results in the vicinity of the chosen evaluation frequency, however, it is not a very accurate solution for the entire frequency interval of interest. It might lead to incorrect results for modes resonating far from the evaluation-frequency, especially if the cutoff frequency of any 2D-mode is inside the investigated spectrum.

For this simplification, there are generally two commonly used possibilities. The first is to use the absolute value of the wave impedance as termination-impedance for the waveguide ports. In this case, the termination-impedance is a real-valued number in any case. Hence, any 2D-mode is simplified to be able to propagate. It is assumed that this method is applied in CST MWS 2014 [38] as hinted in [69]. Unfortunately, this approach is only valid above the cutoff frequency and might lead to an underestimation of the quality factor of some modes, as shown later. A further problem with this approach is, that the external quality factors can be decreased, if the considered number of 2D modes at the waveguide port is increased, even if the newly added modes are far below their cutfoff frequency.

The second choice for the linearisation is to evaluate the wave impedance at the maximum or the mean frequency of the considered spectrum. However, also

[2]Impossible in the sense that the computational time exceeds a certain limit, thus making the computation impractical.

this might lead to errors when computing modes that are not in the vicinity of the linearisation. For comparison, both linearisation approaches will be used in this thesis. Theoretically, both linearisation approaches can compute also the eigenvectors of the system. In CST MWS however, it seems that there is some surrogate problem solved, which only gives the Q_{ext}[3].

Simplification to polynomial EVP

Another, common way for the simplification of the NLEVP is the restriction to only one 2D-eigenmode in each waveguide port as in e.g. [5], [70]. In these cases, the matrix $\mathbf{T}(\lambda)$ can be stated as a polynomial

$$\mathbf{T}(\lambda) = \lambda^r \mathbf{A}_r + \lambda^{r-1}\mathbf{A}_{r-1} + \cdots + \mathbf{A}_0, \tag{4.7}$$

for which a generalized linear eigenvalue problem of the size $r \times n$ needs to be solved [66]. For these quadratic eigenvalue problems, there exist several efficient solution methods, such as second-order Arnoldi-methods [71], Jacobi Methods [67] or Nonlinear Rayleigh-Ritz Approaches [70]. However, in real-life applications the number of 2D-eigenmodes needed for a full description of a certain frequency range of interest is higher than one, mostly 5 - 15 for each waveguide in practical SRF applications. It is concluded that by this simplification some eigenvalues can be computed correctly, but only in cases where an eigenmode couples to only the regarded 2D eigenmode. In practice, this is neither the case, nor is the number of modes known beforehand.

Surrogate Problem

A viable strategy is the solution of a surrogate problem for which the solution is simpler to obtain. This is a standard strategy in engineering. This can be done, among other approaches, using so called *pole fitting* (PF) [72], [73]. Pole fitting (originally referred to as vector fitting) is a common approach used in accelerator physics [50] and [74] . For a full description it is referred to [72] and for the application in accelerator physics it is referred to [50].

The general approach is to obtain the S-parameters, which is feasible even for comparably complex structures. These S-parameters are then approximated by some low-order, linear, time-invariant SSM whose poles approximate the poles of the S-parameters. From these poles one can easily compute the quality factors and loaded frequencies. The drawback of this scheme is that, even though it is comparably fast, the eigenvectors are not obtainable[4]. Another drawback is that it is not always

[3]Since CST MWS is a proprietary software, the actual problem that is solved remains unknown.
[4]This means that the field, as well as any secondary quantity derived from it, is not computable.

straightforward to say which modes are physical and which ones are artificial due to an over-fitting of the approximation.

Another surrogate problem solution that should be mentioned is the usage of so-called perfectly matched layers (PML)[75]. The basic idea is to attach some lossy material to the waveguide ports, thus making them free of reflection. However, in practice there occur unwanted, nonphysical resonances in the spectrum. Furthermore, using this approach the entire domain has to be discretized using complex algebra which might be very time consuming. This technique is still used in accelerator physics [76].

4.2.2 Straight-forward Solution of the NLEVP

In the literature, there are several solution approaches that do not use major simplifications and solve the full problem (4.5). In all publications that deal with the solution of the NLEVP for large scale accelerators, the system is assembled in a way that all matrices are large and sparse (in contrast to this thesis). A general complication is, that a balance has to be found between speed, accuracy and the completeness of the found solutions.

A common approach is the usage of so-called contour integrals as in [77], [78] and [79]. This technique, though very complex to implement, is currently the only technique that guarantees that all modes are found in a certain spectrum. Generally, a complex contour integral over the inverse of $\mathbf{T}(\lambda)$ has to be evaluated. In this thesis this technique is not used since it explicitly prohibits meromorphic functions[5] for $\mathbf{T}(\lambda)$ [79] (which is the case in the presented approach). Nevertheless, there are other formulations of the NLEVP for which this might be a viable solution strategy (e.g. [6]).

In [5] and [6], a straightforward implementation of the NLEVP is presented. Similar to the algorithm presented in this work, the solutions are computed separately in an iterative scheme. However, there are two major differences. The scheme presented in this thesis is based on matching wave impedances while the examples from the literature are based on wave numbers and additionally, no MOR is introduced. While [6] uses a Jacobi-Davidson Type Solver, [5] uses the Implicit Restarted Arnoldi Method for solving the discretized NLEVP.

[5] Meromorphic functions are complex differentiable everywhere but on some singularities.

4.3 Perturbation Approach by Lossless Impedance Model

All methods mentioned in 4.2 struggle with very large systems with several millions of DOFs. Unfortunately, such large systems can easily occur when dealing with accelerating structures. Therefore, the recently proposed methods have to be enhanced. While a common approach, would be application of HPC, in this thesis a combination of well known techniques to solve NLEVPs with the model-order reduction technique SSC is proposed, in order to overcome the problems with very large systems. In a first step, the reduced order model of the investigated, closed structure is computed. Then, the behavior of the same structure is emulated with the attached termination impedance, using a perturbation approach[6]. For a matched waveguide, this can be emulated if one finds a termination condition for each 2D-waveguide port, such that no energy is reflected back into the domain. This is the case if the termination condition $G_{\mathrm{tc,n}}$ is set to be the inverse of the frequency-dependent wave impedance of the 2D port mode:

$$G_{\mathrm{tc,n}} = \frac{1}{Z_{\mathrm{Wave,n}}(s)} = -\frac{i_{\mathrm{n}}(s)}{u_{\mathrm{n}}(s)}. \tag{4.8}$$

Plugging (4.8) into any SSM of the closed structure (e.g. (3.39) and (3.40))[7] one can (with some further modifications) define the problem as:

$$\underbrace{\left(\mathbf{A} + \mathbf{B}\,\mathbf{G}(s)\,\mathbf{B}^T - s\mathbf{I}\right)}_{\mathbf{T}(s)}\mathbf{x}(s) = 0, \tag{4.9}$$

with the matrix $\mathbf{G}(s)$ comprising all 2D wave impedances on the diagonal. The problem (4.9) is described in the literature as a nonlinear eigenvalue problem. It should be noted, that for the formulation of the problem one needs only the SSM of the closed structure and the wave impedance of all 2D waveguide modes which are known analytically for all cases investigated in this thesis. From the solution-pairs $\lambda_n, \mathbf{x}_n$ of the system (4.9) one can derive the external quality factors and the loaded frequencies of the lossy resonances with

$$Q_{\mathrm{ext,n}} = \frac{\Im\{\lambda_n\}}{2\Re\{\lambda_n\}}, \qquad f_n = -\frac{\Im\{\lambda_n\}}{2\pi}. \tag{4.10}$$

[6] The word perturbation approach generally refers to finding an approximate solution to a complex problem, by starting from a known solution of a related, simpler problem. In the presented case, the solution of the complex problem (nonlinear eigenvalue problem) is developed as a weighted sum of solutions of the simple problem (linearized eigenvalue problem), hence it is referred to as perturbation approach.

[7] The indices of the SSM matrices are neglected in the following since the following approach works for any arbitrary impedance formulation in this thesis.

Here, f_n denotes the loaded frequency of the n-th mode and $\Re$ and $\Im$ denote the real- and imaginary part of a quantity. The fields can be extracted from the eigenvectors $\mathbf{x}_n$.

4.3.1 Mathematical Properties of the NLEVP

In this short section, the mathematical properties of the derived system (4.9) are investigated. This will lead to the carefully considered choice of solution algorithms in the next section. These properties differ significantly from standard approaches like [6] and [78], hence the applied techniques for the solution are different.

The derived matrix operator $\mathbf{T}(s)$ is in any case complex-valued. Furthermore, due to the meromorphic functions of the wave impedances (2.39) and (2.41) the matrix operator $\mathbf{T}(s)$ is also meromorphic with countably many isolated poles. These poles are not removable singularities since either the limit

$$\lim_{s \to j\omega_{co,n}} \mathbf{T}(s) \text{ or } \lim_{s \to j\omega_{co,n}} \mathbf{T}^{-1}(s), \tag{4.11}$$

does not exist, hence the function can not be reformulated in a continuous way. The isolated poles[8] are located at zero and eigenvalues with zero real part and an imaginary part with the absolute value of the cutoff-angular frequency of any 2D TM mode

$$\lambda = 0 \text{ or } \lambda = j\omega_{co,n}^{\mathrm{TM}} \quad \vee n. \tag{4.12}$$

Both singularities are not of practical relevance since one is not interested in static modes nor in modes that have no real part. Such a mode would have an infinite quality factor and is unphysical for the systems that are investigated in this thesis. However, these singularities hinder the employment of more sophisticated techniques like contour integrals which are only applicable for holomorphic functions [79].

If the matrices of the closed SSM in (4.11) originate from a concatenated, reduced system (which is the case for any shown application in this thesis), the matrix $\mathbf{T}(\lambda_i)$ is (comparably) small and dense. In all applications shown in this thesis the size of the systems remained below 5,000 DOFs. Due to the density, techniques that are suited for large, sparse matrices like e.g. Krylov-Subspace methods are not practical.

4.4 Newton Iteration for Matrix Operators

The method chosen in thesis has to be suited to compute the desired eigenpairs fast and accurately. Additionally, in all shown applications, several eigenmodes with

[8] An isolated pole z_0 means, that the function is holomorphic in the vicinity D of the pole, i.e. holomorphic on $D \setminus \{z_0\}$.

eigenvalues of multiplicity of at least two have to be computed. Hence, a technique is picked, that is suited for meromorphic matrix operators with dense matrices. Further, the chosen method has to be able to deflate[9] the search space by using the eigenvector or eigenpairs[10]. According to [81], there are surprisingly few methods to handle this problem. An easy way to compute some small eigenvalues is the Newton method (sometimes also referred to as Newton-Raphson method), further denoted as NM. With some minor changes to (4.5) one can use the NM to solve for the zeros as proposed in [82] and extended in [66]. The summary on how to apply NM to the studied problem is given in this section, partly following [66].

To obtain the i-th solution pair $\{\mathbf{x}_i, \lambda_i\}$ of (4.9) a linear, matrix operator $\mathbf{P}$ is defined as

$$\mathbf{P}\begin{bmatrix} \mathbf{x}_i \\ \lambda_i \end{bmatrix} = \begin{bmatrix} \mathbf{T}(\lambda_i)\mathbf{x}_i \\ \mathbf{v}^{\mathrm{H}}\mathbf{x}_i - 1 \end{bmatrix} = \mathbf{0}, \tag{4.13}$$

where the vector $\mathbf{v}$ acts as a normalisation for the eigenvector. The superscript H denotes the conjugate transpose of said vector. The goal is to find all solutions in a certain frequency range. This is achieved by finding the roots of $\mathbf{P}$, for which the eigenvalue λ_i has an imaginary part smaller than the maximal angular frequency. Further, the matrix operator $\mathbf{P}$ is differentiated with $\begin{bmatrix} \frac{\partial}{\partial \mathbf{x}_i} & \frac{\partial}{\partial \lambda_i} \end{bmatrix}$ to obtain the so-called Fréchet derivative[11] $\mathbf{P}'$

$$\mathbf{P}'\begin{bmatrix} \mathbf{x}_i \\ \lambda_i \end{bmatrix} = \begin{bmatrix} \mathbf{T}(\lambda_i) & \frac{\partial \mathbf{T}(\lambda_i)}{\partial \lambda_i}\mathbf{x}_i \\ \mathbf{v}^{\mathrm{H}} & 0 \end{bmatrix}. \tag{4.14}$$

From the problem specification in (4.9) one can determine the derivative

$$\frac{\partial \mathbf{T}(\lambda_i)}{\partial \lambda_i} = -\mathbf{B}\,\frac{\partial}{\partial \lambda_i}\mathbf{G}(\lambda)\,\mathbf{B}^{\mathrm{T}} - \mathbf{I}, \tag{4.15}$$

without approximation[12]. Further, from (4.15) one needs to determine the derivative $\frac{\partial}{\partial \lambda_i}\mathbf{G}(\lambda)$ for all possible 2D port modes. For a matched waveguide one can determine the derivative without approximation as

$$\frac{\partial}{\partial \lambda_i}\mathrm{G}^{\mathrm{TE}}(\lambda) = \frac{1}{\mathrm{Z}_0}\left(\frac{1}{\sqrt{\lambda^2 + \omega_{co}^2}} - \frac{1}{\lambda^2}\sqrt{\lambda^2 + \omega_{co}^2}\right), \tag{4.16}$$

[9] The method has to exclude all found eigenvectors from the search space. This is called deflation [80].

[10] Since, as stated earlier, the eigenvalues can have a multiplicity of at least two, while two eigenvectors can not be the same.

[11] Please note that this is not a common derivative in Euclidean-space but a generalization of the derivative for matrix-functions. Therefore, said derivatives follow slightly different mathematical rules shown in [83].

[12] The derivative itself is without approximation, even though, some of the matrices contained are not.

$$\frac{\partial}{\partial \lambda_i} \mathrm{G}^{\mathrm{TM}}(\lambda) = \frac{1}{\mathrm{Z}_0} \left(\frac{1}{\sqrt{\lambda^2 + \omega_{co}^2}} - \frac{\lambda^2}{(\lambda^2 + \omega_{co}^2)^{\frac{3}{2}}} \right), \tag{4.17}$$

$$\frac{\partial}{\partial \lambda_i} \mathrm{G}^{\mathrm{TEM}}(\lambda) = 0. \tag{4.18}$$

The equations (4.16) and (4.17) only hold for matched waveguides. In the case of a loaded waveguide, the derivative is not known analytically. It could be approximated numerically (but this is not investigated in this thesis). In the next step (for any arbitrary termination impedance), one can use a Taylor-Series expansion of first order of $\mathbf{P}$ and (after some rearrangements) derive the NM for the j-th iterative solution of the i-th mode of (4.13) as

$$\mathbf{P}' \begin{bmatrix} \mathbf{x}_{i,j} \\ \lambda_{i,j} \end{bmatrix} \begin{bmatrix} x_{i,j+1} - x_{i,j} \\ \lambda_{i,j+1} - \lambda_{i,j} \end{bmatrix} = \mathbf{P} \begin{bmatrix} \mathbf{x}_{i,j} \\ \lambda_{i,j} \end{bmatrix}. \tag{4.19}$$

The formulation (4.19) is written with $\mathbf{P}'$ on the left-hand-side in order to avoid explicitly computing its inverse. Plugging the definition of $\mathbf{P}$ (4.13) and its Fréchet derivative $\mathbf{P}'$ (4.14) into (4.19) gives

$$\begin{bmatrix} \mathbf{T}(\lambda_{i,j}) & \frac{\partial \mathbf{T}(\lambda_{i,j})}{\partial \lambda_{i,j}} \mathbf{x}_{\mathrm{i,j}} \\ \mathbf{v}^{\mathrm{H}} & 0 \end{bmatrix} \begin{bmatrix} \mathbf{x}_{\mathrm{i,j+1}} - \mathbf{x}_{\mathrm{i,j}} \\ \lambda_{i,j+1} - \lambda_{i,j} \end{bmatrix} = - \begin{bmatrix} \mathbf{T}(\lambda_{i,j}) \mathbf{x}_{\mathrm{i,j}} \\ \mathbf{v}^{\mathrm{H}} \mathbf{x}_{\mathrm{i,j}} - 1 \end{bmatrix}. \tag{4.20}$$

The system (4.20) has to be solved multiple times for each desired solution. It can be further simplified by separating the two equations into two linearly dependent equations. The upper equation from (4.20) gives

$$\mathbf{x}_{\mathrm{i,j+1}} = \underbrace{-\mathbf{T}^{-1}(\lambda_{i,j}) \frac{\partial \mathbf{T}(\lambda_{i,j})}{\partial \lambda_{i,j}} \mathbf{x}_{\mathrm{i,j}}}_{\mathbf{u}_{\mathrm{i,j+1}}} \cdot (\lambda_{i,j+1} - \lambda_{i,j}), \tag{4.21}$$

where the direction of the new iteration of the searched eigenvector $\mathbf{x}_{\mathrm{i,j+1}}$ is introduced as auxiliary variable $\mathbf{u}_{\mathrm{i,j+1}}$. The formula of the search direction $\mathbf{u}_{\mathrm{i,j+1}}$ can be explicitly written from (4.21)

$$\mathbf{u}_{\mathrm{i,j+1}} = \mathbf{T}^{-1}(\lambda_{i,j}) \frac{\partial \mathbf{T}(\lambda_{i,j})}{\partial \lambda_{i,j}} \mathbf{x}_{\mathrm{i,j}}. \tag{4.22}$$

Since $\mathbf{x}_{\mathrm{i,j}}$ is forced to be normalised by (4.13), the second equation gives

$$\mathbf{v}^{\mathrm{H}} \mathbf{x}_{\mathrm{i,j+1}} = \mathbf{v}^{\mathrm{H}} \mathbf{x}_{\mathrm{i,j}}. \tag{4.23}$$

Multiplying (4.22) with the normalisation vector $\mathbf{v}^{\mathrm{H}}$ under consideration of (4.23) gives

$$\lambda_{i,j+1} = \lambda_{i,j} - \frac{\mathbf{v}_i^{\mathrm{H}}\,\mathbf{x}_{i,j}}{\mathbf{v}_i^{\mathrm{H}}\,\mathbf{u}_{i,j+1}}. \tag{4.24}$$

Having determined the new direction $\mathbf{u}_{\mathrm{i,j+1}}$ from (4.22) and the new eigenvalue $\lambda_{i,j+1}$, their product can be used to compute the new eigenvector $\mathbf{x}_{\mathrm{i,j+1}}$ according to (4.21). Instead, the new eigenvector $\mathbf{x}_{\mathrm{i,j+1}}$ is computed as $\mathbf{x}_{\mathrm{i,j+1}} = c \cdot \mathbf{u}_{\mathrm{i,j+1}}$, with the arbitrary scaling constant c as $0 < c < 1$ to guarantee convergence as described in [83][13]. Note that this scaling does not influence the direction of the search-vector, just the step size.

This procedure is summed up in Algorithm 4.

Algorithm 4 Newton iteration i-th solution pair

Require: Initial guess $\{\lambda_{i,0}, \mathbf{x}_{i,0}\}$, desired residual θ, normalisation vector $\mathbf{v}_i^{\mathrm{H}}$

1: Normalize initial guess $\mathbf{v}_i^{\mathrm{H}}\mathbf{x}_{i,0} = 1$
2: **while** $r_i > \theta$, $j <$ max. iterations **do**
3: Compute new direction $\mathbf{u}_{\mathrm{i,j+1}} = \mathbf{T}^{-1}(\lambda_{i,j})\frac{\partial \mathbf{T}(\lambda_{i,j})}{\partial \lambda_{i,j}}\mathbf{x}_{\mathrm{i,j}}$
4: Compute new eigenvalue $\lambda_{i,j+1} = \lambda_{i,j} - \frac{\mathbf{v}_i^{\mathrm{H}}\,\mathbf{x}_{i,j}}{\mathbf{v}_i^{\mathrm{H}}\,\mathbf{u}_{i,j+1}}$
5: Compute new eigenvector $\mathbf{x}_{\mathrm{i,j+1}} = c \cdot \mathbf{u}_{\mathrm{i,j+1}}$
6: Compute residual $r_i = \|\mathbf{T}(\lambda_{i,j+1})\,\mathbf{x}_{\mathrm{i,j+1}}\|/\|\mathbf{x}_{\mathrm{i,j+1}}\|$
7: Increment j
8: **end while**

The i-th solution pair is considered as converged if the residual r_i is below the desired accuracy θ before the maximum number of iterations is reached. For further convenience, the converged eigenvectors $\mathbf{x}_{\mathrm{i,j}}$ are later normalised such that their energy inside the considered domain $\boldsymbol{\Omega}$ is 1 J. From (4.4) one can see that the energy is in fact not determined and can be chosen freely.

4.4.1 Deflation of the Search Space

For real life examples, one is generally interested in several eigenpairs, not just one. This leads to the deflation of the NLEVP. It needs to be ensured, that all eigenpairs of interest are found and that the scheme does not converge towards an already found eigenpair[14]. Since in problems originating from the Helmholtz equation multiple, equal eigenvalues (with multiplicities larger than two) can occur, a deflation strategy that is based either on eigenpairs or eigenvectors is needed, since neither has multiplicities. This is achieved by an elaborate determination of the

[13] The scheme converges as well if the new eigenvectors $\mathbf{x}_{\mathrm{i,j+1}}$ are computed according to (4.21) but the convergence is not guaranteed in that case.

[14] The second condition is not mandatory, but only to ensure an optimal performance.

(theoretically arbitrary) normalisation vector $\mathbf{v}_{\mathrm{i}+1}$ for finding the $(i+1)$-th eigenpair. In this case one can choose the normalisation vector such that it is orthogonal to all i eigenvectors that have already converged as described in [66][15]. It should be noted that the deflation strategy has not be very performant, due to the small size of the deflated system. A simple, yet very efficient way to compute a new orthogonal search direction is to comprise all i found eigenvectors in a matrix $\mathbf{X}_{\mathrm{i}}$ and find an arbitrary, non-trivial vector $\mathbf{v}_{\mathrm{i}+1}$ such that

$$\underbrace{\left(\mathbf{x}_1\ \mathbf{x}_2\ \ldots\ \mathbf{x}_{\mathrm{i}}\right)^{\mathrm{H}}}_{\mathbf{X}_{\mathrm{i}}^{\mathrm{H}}} \cdot \mathbf{v}_{\mathrm{i}+1} = 0. \tag{4.25}$$

Therefore, each vector of the null-space of $\mathbf{X}_{\mathrm{i}}$ can be used as new search direction[16]. Including the deflation, the Algorithm 4 can be extended in Algorithm 5.

Algorithm 5 Newton iteration for several solution pairs

Require: Initial guess $\{\lambda_{i,0}, \mathbf{x}_{i,0}\}$, desired residual θ
1: Determine vector norm $\mathbf{v}_0^{\mathrm{H}}\mathbf{x}_{i,0} = 1$
2: **for** $i = 1 \rightarrow N$ **do**
3: Compute solution pair according to Algorithm 4
4: Determine null-space of all found eigenvectors $\mathbf{X}$
5: Determine new normalisation vector $\mathbf{v}_{i+1}^{\mathrm{H}}$ as arbitrary vector from null-space
6: **end for**

4.4.2 Scaling of the NLEVP

The NLEVP as described in the previous section converges comparably slow. This is due to the bad condition number of the system of equations when computing the new search direction in (4.22). A closer look at the derivatives of the wave admittances (4.16) and (4.17) shows that this is caused by the inverse of the square of the eigenvalues. If the imaginary part of the eigenvalues is somewhere in the GHz range, this might cause the bad condition. This however, can be easily fixed by scaling the entire system such that the eigenvalues are not in the GHz range but in Hz range. According to [84] the problem at hand allows this kind of scaling without changing the eigenvalues nonlinearly[17]. This simple trick restores the convergence to a few iterations (generally <5) as expected from literature from comparable problems [83].

[15] It should be noted that this property does not require the eigenvectors to be mutually orthogonal.
[16] If there have not been found any eigenvectors yet, e.g. for the solution of the very first eigenmode, one can simply pick a random vector or a solution to the linearised eigenvalue problem.
[17] At first sight it is counter-intuitive that a problem that is nonlinear regarding the frequency can be scaled in the frequency range but if the entire system (including e.g. the cutoff frequencies) is scaled, the eigenvalues can be scaled back linearly to the original frequency domain.

4.5 Relative Power through Port Mode

An important investigation that is possible by solving the NLEVP is the computation of the power through each port mode. This enables a more sophisticated investigation of the power than external quality factors since the relative power loss could be accounted to a specific port and port mode. This would be especially important e.g. for the design of HOM couplers and to deepen the understanding of lossy effects. There are generally two ways to compute the power through the port surfaces. The first is to compute the full electric and magnetic fields from the eigenvectors of the NLEVP. Then one has to integrate the Poynting vector by integrating the cross-product of electric and magnetic field in the waveguide-port surface. Another, drastically simpler way was proposed by S. Zadeh [85], by computing the product of modal voltage and current for each 2D port mode, as highlighted earlier in (2.33), for a given eigenvector $\mathbf{x}_\mathrm{i}$ with the eigenvalue λ_i. Firstly, the relationship between modal voltages and currents can be written as

$$\mathbf{i}(s) = \left(\mathbf{B}^\mathrm{T}\left(\lambda_\mathrm{i} - \mathbf{A}\right)^{-1}\mathbf{B}\right)^{-1}\mathbf{v}(s). \tag{4.26}$$

This is the inverse transmission function of the system at the specific resonant frequency of the investigated mode. The modal voltage can be described as

$$\mathbf{v}(s) = \mathbf{B}^\mathrm{T}\mathbf{x}_\mathrm{i}. \tag{4.27}$$

Plugging (4.27) into (4.26) one can multiply the vectors of modal voltages and currents element by element, leading to the power of the i-th mode through the port modes as

$$\mathbf{P}_\mathrm{Prt} = \mathbf{i}(s) \circ \mathbf{v}(s) = \left(\mathbf{B}^\mathrm{T}\left(\lambda_\mathrm{i} - \mathbf{A}\right)^{-1}\mathbf{B}\right)^{-1}\mathbf{B}^\mathrm{T}\mathbf{x}_\mathrm{i} \circ \mathbf{B}^\mathrm{T}\mathbf{x}_\mathrm{i}. \tag{4.28}$$

with the vector $\mathbf{P}_\mathrm{Prt}$ containing the power through each 2D port mode for the solution pair $\lambda_\mathrm{i}, \mathbf{x}_\mathrm{i}$. The elementwise multiplication of modal voltages and currents is denoted with the Hadamard product $\circ$. Unfortunately, only the relative power can be computed due to the fact that the energy of the eigenvector is not uniquely determined by the NLEVP. Therefore, only a relative statement about how much of the losses is going through which port-mode is possible. It should be further noted that this approach is not equivalent to computing the quality factors for each port while closing all others which does not lead to reasonable results due to the nonlinearity of the problem.

4.6 Numerical Examples

In this chapter some results are shown that have been obtained by solving the NLEVP and they are partly compared to the two linearisation approaches and PF.

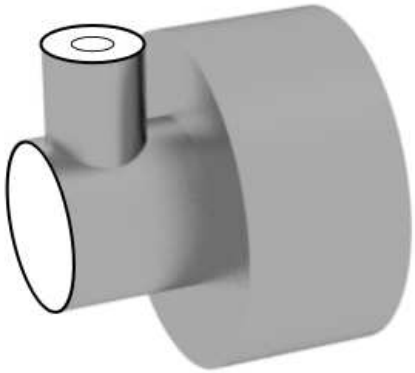

Abbildung 4.1: This picture shows a structure which is used as model example to solve the NLEVP, consisting of a resonator and a simplified HOM coupler. This structure has two waveguide ports, one at the coupler and the other one at the beam pipe. To avoid confusion, the port surfaces are colored in white. The frequencies of the considered 2D port modes is shown in Table 4.1.

Unfortunately, to the author's best knowledge, there is no analytical example which contains only external losses to test the proposed algorithm. Therefore, two numerical examples are investigated: A simplified resonator and a cavity with two couplers (with a structure described in [86] and [87]). All computations were performed on a Intel(R) Xeon(R) CPU E5-2687W @3.4 GHz with 256 GB of RAM, running on Windows Server 2012 as operating system. All shown cases used SSC as described in this thesis. In all shown cases all eigenmodes of the NLEVP (that were found by the algorithm) in the given frequency interval were computed with a relative residual smaller than 10^{-6}. The residual of the j-th mode at the i-th iteration is defined as $\|\mathbf{T}_j(\lambda_{i,j})\,\mathbf{x}_{i,j}\|_2/\|\mathbf{x}_{i,j}\|_2$. The solution of the NLEVP was implemented straightforward from Algorithms 4 and 5 and was done in Matlab R2015b [88]. All field visualizations have been generated in Paraview [48], the structures were visualized in Blender [89].

4.6.1 Minimalistic Resonator

As a minimalistic model to show the performance of some of the latter described algorithms a minimalistic resonator with a simplified HOM coupler as denoted in Fig. 4.2 is computed. This structure does not have any practical relevance, it just serves as example. A frequency domain of 0 - 6 GHz is chosen, which results in eight waveguide portmodes that are being used in this example. Three waveguide-portmodes are located at the antenna (one TEM mode and two TE modes) and five are located at the beam pipe which is further described in Table 4.1. The solutions were computed using the Newton Method as given in Algorithms 4 and 5.

Tabelle 4.1: The list of 2D waveguide port modes for the minimalistic resonator shown in Fig. 4.1 and its cutoff frequencies in a frequency domain of 0 - 6 GHz.

Port	**Mode**	f_{co} **[GHz]**
1	TEM	0
1	TE_{11} pol. 1	5.902
1	TE_{11} pol. 2	5.902
2	TE_{11} pol. 1	4.389
2	TE_{11} pol. 2	4.389
2	TM_{01}	5.732
2	TE_{21} pol. 1	7.275
2	TE_{21} pol. 2	7.275

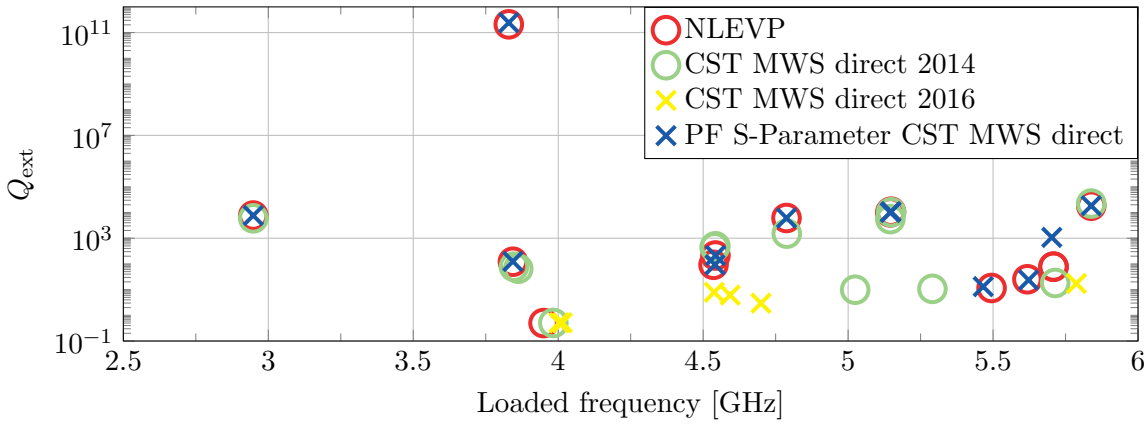

Abbildung 4.2: This picture shows a comparison of computed Q_{ext} using different methods for the simple test resonator from Fig. 4.1 in a frequency interval from 0 - 6 GHz. All modes with a Q_{ext} below 0.1 were neglected for this plot. It can be seen that while the NLEVP and PF deliver comparable solutions, there are several modes for which CST MWS delivers different results.

In Fig. 4.2, the Q_{ext} as function of the loaded frequency as derived from the solution of the NLEVP inside the domain described in Fig. 4.1 is shown for different methods. The legend entry NLEVP refers to the solution of the non-simplified, NLEVP as outlined in Algorithms 4 and 5. All methods use the exact same underlying discretization with FIT in CST MWS using a hexahedral grid resulting in roughly 233,000 DOFs. For the discretization, no domain decomposition was used (i.e. only a MOR). Computing all 15 modes in the frequency range took 22 s for a ROM with 194 DOFs. The ROM was obtained in 7 m and 41 s. Computing the Q_{ext} with CST

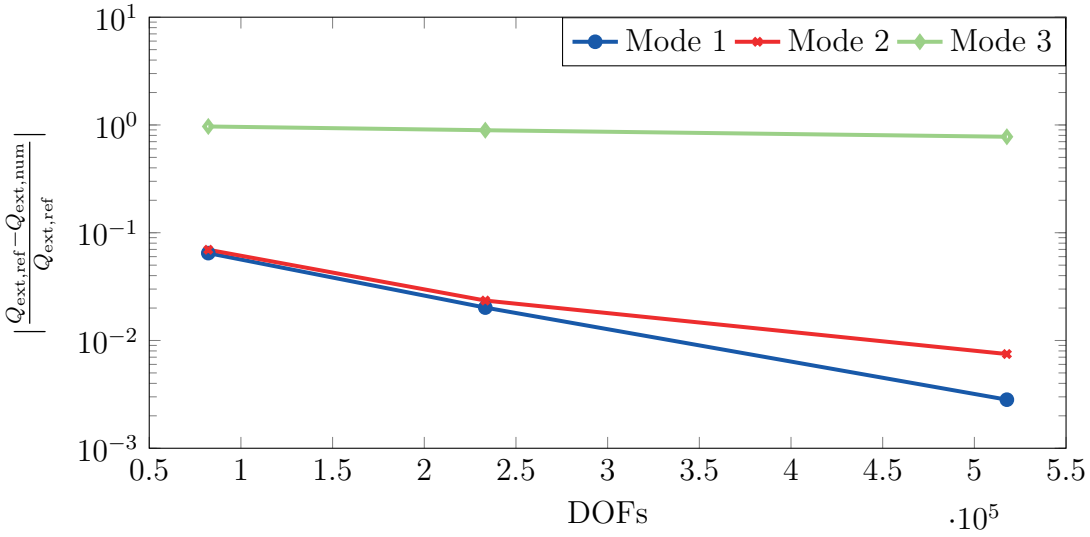

Abbildung 4.3: This picture shows the convergence of Q_{ext} regarding the DOFs of the initial non-reduced FIT discretization, obtained from the first three solutions (regarding their frequency) of the NLEVP. These solutions are denoted by $Q_{\text{ext,num}}$. Since there is no analytical solution available, the solution of the same problem with roughly 1 Mio. DOFs was chosen as reference and is denoted with $Q_{\text{ext,ref}}$. It can be seen that for the modes one and two, the solution gets more accurate, as the DOFs are increased. Unfortunately, for the third mode, this is not the case. It is assumed that this is due to the fact that the modes Q_{ext} should be infinite, which leads to problems in the algorithm.

MWS 2014 took 18 m and 8 s.[18] It can be seen that the proposed NM and PF give results within roughly the same order of magnitude. Above cutoff of the first two TE modes in the beam pipe (at approximately 4.38 GHz) the results of CST MWS 2014 also fit well to the other two methods. A large difference is clearly visible for a mode at approximately 3.82 GHz. While NM and PF find this mode to have a high Q_{ext} of approximately 10^{11}, CST MWS 2014 finds this mode to have a Q_{ext} of approximately 10^2. It is assumed that the different orders of magnitude originate from the linearisation employed in CST MWS. The discussed mode couples poorly to the TEM mode at the antenna. However, it couples well to the TE mode in the beam pipe. At the frequency at which this mode resonates, this TE mode is approximately 0.5 GHz below its cutoff frequency. Hence, for an infinitely long beam pipe, no energy couples out of the beam pipe, resulting in a very high Q_{ext}. The energy can couple solely through the TEM mode, which can be evaluated by (4.28). This is computed correctly by NM and PF. In contrast, CST MWS linearises the problem in a way that the TE mode is above its cutoff. Due to the artificial coupling

[18] It should be noted however, that this comparison is not really one-to-one since CST MWS solves a slightly simpler problem (by linearisation) and has no need to export the obtained matrices into Matlab.

between 3D and 2D-mode, the energy can couple out of the system well, resulting in rather low Q_{ext}. Taking the results into consideration, it is concluded that the presented approach to the solutions of the NLEVP delivers reasonable results that coincide well with known techniques like PF. For CST MWS 2014 the approximation, that every mode is above its cutoff frequency might lead to inaccurate results in some cases. For the shown example, CST MWS 2016 finds only five of the eleven modes in the investigated frequency-range. Hence, in this thesis CST MWS 2014 was used for comparison.

Furthermore, it is investigated how the solution of the NLEVP differs when the DOFs of the discretization are increased. The results are shown in Fig. 4.3 for the first three modes. It can be seen that for the modes one and two, the solution gets more accurate, as the DOFs are increased. Unfortunately, for the third mode, this is not the case. It is assumed that this is due to the fact that the Q_{ext} of this mode should be infinite, which leads to problems in the algorithm[19].

4.6.2 Cavity with Coupler

As a further numerical example, the NLEVP is solved for a structure that has practical relevance to accelerator physics, one nine-cell cavity with a HOM and an input coupler attached as shown in Fig. 4.4. This example was taken from [90] and is a subpart of the Third Harmonic Module which consists of four nine-cell 3.9 GHz cavities. For the sake of simplicity, the example is focused on only one cavity. The structure is investigated in a frequency range from 3 - 8 GHz. The FIT discretization results in 2.2 $\cdot 10^6$ DOFs. In this case there are 25 waveguide modes that need to be considered. Applying SSC with a decomposition in three parts (HOM coupler, cavity and HOM coupler wih input coupler) took roughly 5 h and 2 m. Computing all 160 lossy modes for the previously assembled NLEVP in the frequency domain of interest took 7 m and 50 s.

As a first step, the external quality factors were computed for the investigated structure with the previously proposed algorithm, a linearisation at 8 GHz, CST MWS and PF with scattering-parameters directly obtained by CST MWS. The results can be seen in Fig. 4.5. As mentioned earlier, when referring to specific modes, it is common practice to apply a multipole expansion (e.g. a mode could be the first TE quadrupole mode). The multipole expansion for this specific cavity was taken from [91].

Comparing the first monopole band from 3.75-3.9 GHz, one can see that the results from the PF and NLEVP coincide very well, while the Q_{ext} obtained by linearisation and CST MWS are lower for all modes in this band. This is due to the fact, that for both linearisation approaches, the first TM mode at the beam pipe is assumed

[19] This is not a problem solely of the proposed algorithm, but any algorithm that is used to compute quality factors.

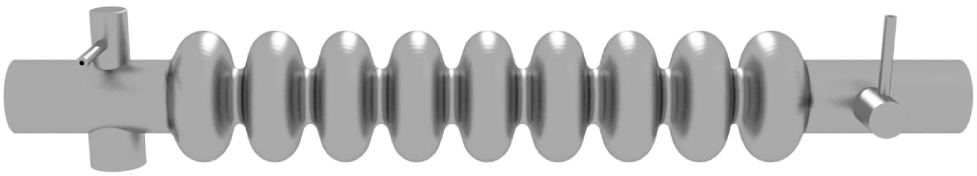

Abbildung 4.4: This picture shows the second example which is used to validate the proposed algorithm. The structure consists of a nine-cell 3.9 GHz cavity, a HOM coupler on the right and combined a HOM coupler and input coupler on the left. This structure is a part of the Third Harmonic Module from [90]. The waveguide ports are located at the two HOM couplers (with one TEM mode), the input coupler (with one TEM mode and two TE modes) and both sides of the beam pipe (with ten 2D modes each).

to be above its cutoff frequency. This means, that some energy can propagate out of the beam pipes through this mode. For PF and NLEVP, this TM mode is correctly assumed to be below its cutoff frequency at 5.74 GHz. Therefore, the energy can only couple out of the coupler through the TEM modes. The mode with the highest frequency from this band is the π-mode, whose field pattern is shown in Fig. 4.6.

The biggest difference between various linearisation approaches and the NLEVP can be seen in the mode resonating at 4.137 GHz[20]. The field pattern originating from the NLEVP can be seen in Fig. 4.7. This mode has a Q_{ext} of roughly $3.82 \cdot 10^6$. Here both linearisation approaches compute a rather low Q_{ext}. This is again due to the linearisation above cutoff, in this case of the first two TE modes in the beam pipe. The mode shows a good coupling to these two 2D modes, but not to the coupler. Since the two TE modes are below their cutoff frequency, the energy can not couple out through the beam pipe which is correctly represented by the NLEVP and PF. The same effect can be seen for the quadrupole modes at 7.25 GHz whose quality factors are slightly underestimated by both linearisation approaches. The field pattern of the mode with the highest Q_{ext} is shown in Fig. 4.8. PF could not accurately compute these modes and underestimates the Q_{ext}. It is assumed that PF has problems when dealing with high Q_{ext} in densely populated spectra. Even though some values fit well to the solution of the NLEVP, it is difficult to make a good assessment from this data.

It should be emphasized that even though CST MWS performs well above the first cutoff it does not provide the eigenvectors, hence the electromagnetic field distributions which are needed to compute the interaction with charged particles passing the structure or how much power propagates through which port mode.

[20] This mode has been computed e.g. in [87] with a comparably high Q_{ext} of roughly $5.5 \cdot 10^5$. However, these computations were conducted using the rather costly method of computing the frequency change when solving the problem with PMC and PEC boundaries at the port as suggested in [68].

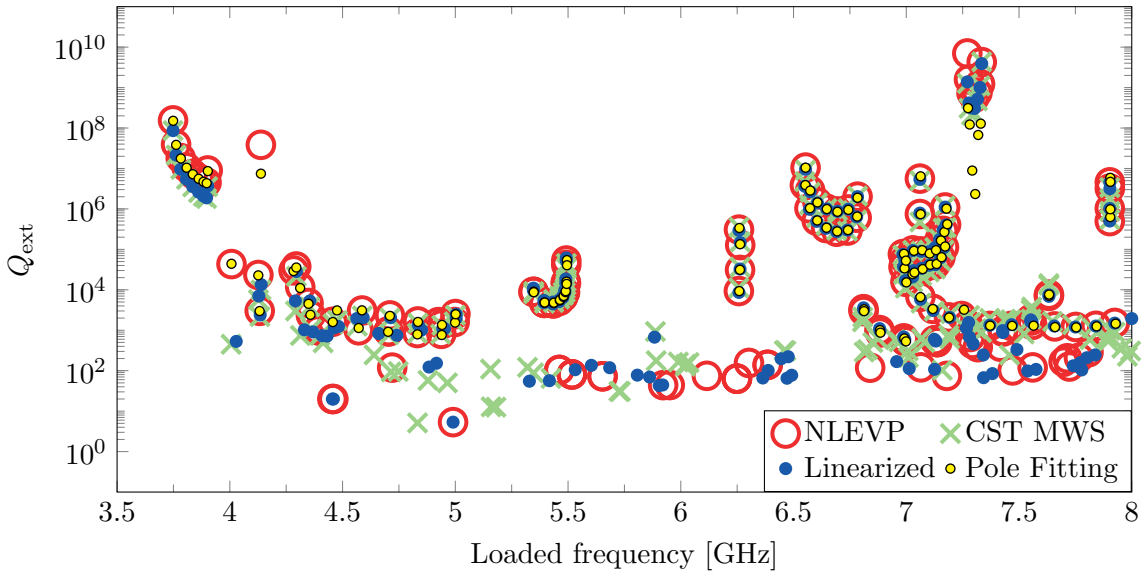

Abbildung 4.5: This plot shows the results computed for the cavity shown in Fig. 4.4 computed with different approaches. The solutions of the NLEVP are marked with red circles, the solutions obtained by CST MWS are marked with green crosses, the results obtained by the linearisation approach are marked by a blue dot and the PF results are highlighted by a yellow dot, respectively. For a better overview, eigenmodes with a loaded frequency below 3.5 GHz and eigenmodes with very low computed Q_{ext} have been omitted in this plot.

4.6.3 Physical Consistency of the Solution

An important property of the modeling of physical problems is that the model is still physically consistent[21]. In the context of the NLEVP, that means that, since the NLEVP-model is defined in a way that we have an infinitely long beam pipe attached, changing the actual length of the beam pipe attached at the end in the discretized domain should not change the results whatsoever [92]. In the following example the physical consistency of the solution obtained from the NLEVP is examined. For this, the example from Fig. 4.4 is computed with successively extended beam pipes.

It was found that for the previously used methods, i.e. CST MWS and linearisation, this statement does not hold true, hence the eigenvalues are a function of the beam pipe length (which should not be the case). In the following, the NLEVP is solved for three variations of the structure and the results are compared for all tested methods: First, the initial design as shown in Fig. 4.4, secondly, the same structure with every beam pipe extended by 42 mm and thirdly, the same structure with every beam pipe extended by $42{\cdot}\pi$ mm. In Fig. 4.9 the results are shown as computed with CST

[21] The word "consistentïs used in the logical sense as in: Free of logical contradictions instead of the numerical consistency.

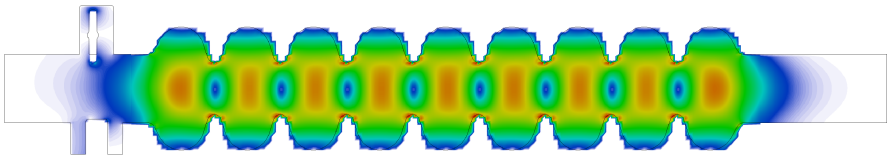

Abbildung 4.6: This picture shows the absolute value of the electric field strength from a lossy eigenmode computed with NM from the NLEVP. This mode occurs at 3.9 GHz and depicts the π-mode.

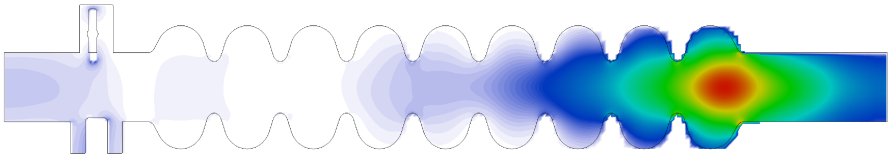

Abbildung 4.7: This picture shows the absolute value of the electric field strength from a lossy eigenmode computed with NM from the NLEVP. This mode occurs at 4.137 GHz and is shown to be trapped with a Q_{ext} higher than 10^6.

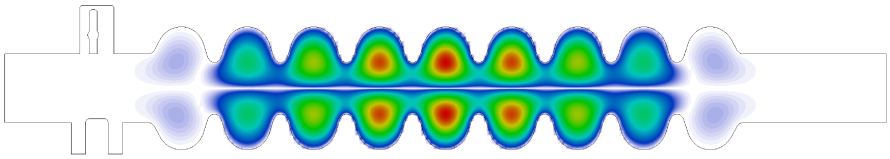

Abbildung 4.8: This picture shows the absolute value of the electric field strength from a lossy eigenmode computed with NM from the NLEVP. This mode occurs at 7.270 GHz. It has the highest Q_{ext} in the frequency domain of interest of approximately 10^9.

MWS. It can be seen that for different length of the beam pipes, the results change in some case by several orders of magnitude. This is problematic for the modes with high Q_{ext} since these modes need to be determined very accurately. Especially, the mode located at 4.15 GHz changes several orders of magnitude when increasing the length of the beam pipe.

In Fig. 4.10 the results of the NLEVP are shown for different length of the attached beam pipe. The results agree well for all three setups. As an example the mode at 4.137 GHz with a Q_{ext} of roughly $3.82 \cdot 10^6$, differs by 0.4 % between the minimum and maximum value between the three different structures. Therefore, one can conclude that the presented algorithm is physically consistent and shows the expected behavior. Only for some modes with $Q_{\text{ext}} < 10^2$ there are visible changes. Yet, one is generally not interested in these modes, since they can not endanger the beam quality.

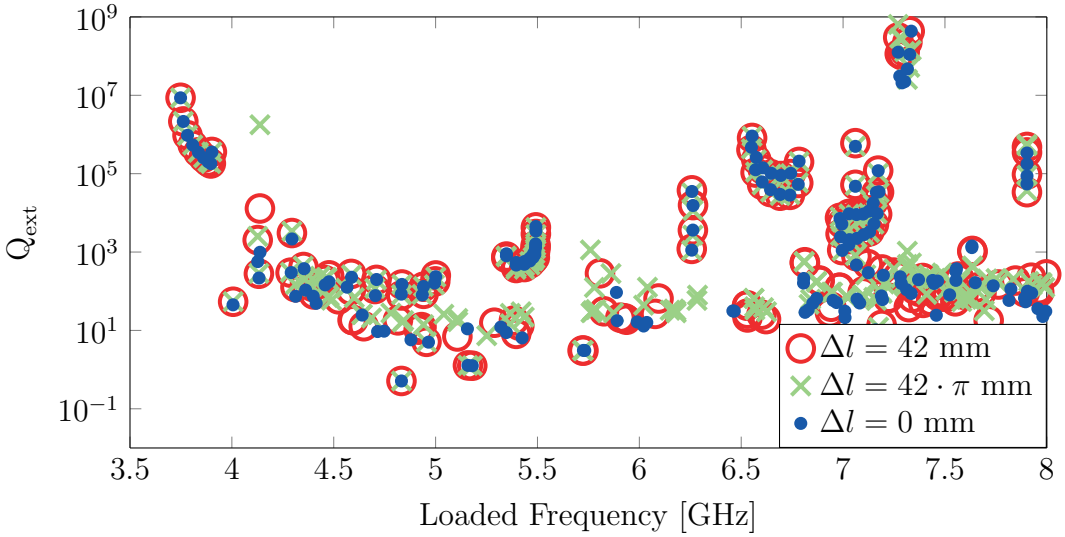

Abbildung 4.9: This plot shows a comparison of the computed external quality factors with CST MWS for the FLASH cavity with successively prolonged beam pipes for the cavity depicted in Fig. 4.4. It can be seen that for different beam pipe length, the Q_{ext} differ significantly, i.e. the simulation is not physically consistent.

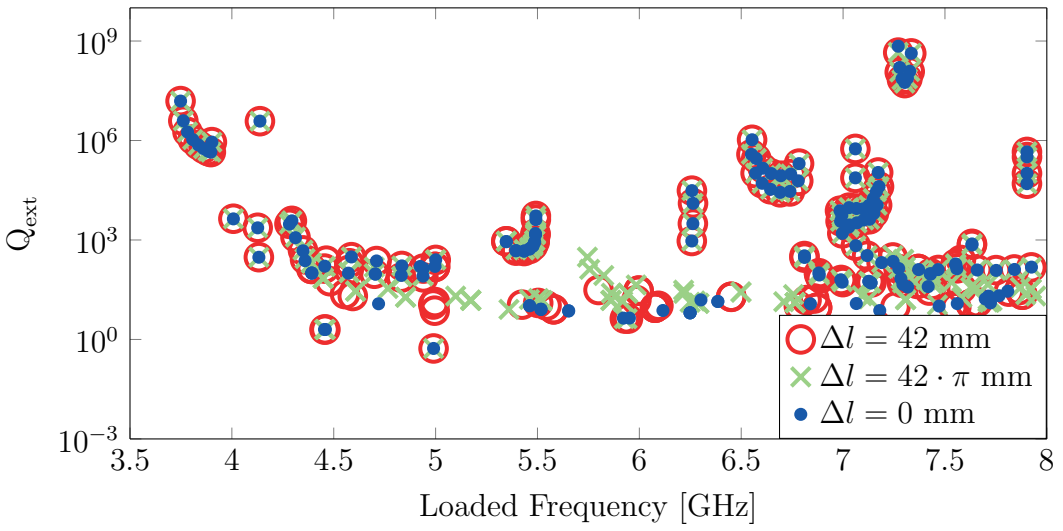

Abbildung 4.10: This plot shows a comparison of the computed external quality factors from the NLEVP for the FLASH cavity with successively prolonged beam pipes for the cavity depicted in Fig. 4.4. It can be seen that for different beam pipe length, the Q_{ext} for modes with $Q_{\text{ext}} > 10^2$ hardly differs for most modes, i.e. the simulation appears to be physically consistent.

4.6.4 Comparison to Measurements

The Q_{ext} can also be validated by measurements[22] as seen in Fig. 4.11. Here, the solution obtained by CST MWS and NLEVP are compared to measurements conducted in [95]. These measurements originate from pole-fitted scattering-parameters measured at the FLASH Third Harmonic Module at DESY. The comparison is restricted to the first monopole band. Therefore, there should be 36 modes measured (nine for each cavity). However, in all but one case the S-parameter peak of the π-mode was below the noise floor of the network analyzer and a good estimate of Q_{ext} could not be obtained. It should be noted however, that in [95] in fact the loaded quality factor is measured. But for the first monopole band, the external and loaded quality factors should be nearly equal due to the small losses.

The measurements and the numerical computations are generally in good agreement. For the π-mode the difference between NLEVP and measured Q_{ext} is smaller than 10 % while for CST MWS, the difference is bigger than 50 %. The differences between measurements and simulation might originate from the slightly different structure. Obviously the design can not be built without minor geometrical imperfections. Also, the built structure is cooled and tuned when commissioned, which might further perturb the structure. Another unknown influence are additional reflections from TEM modes used in the measurements due to an unmatched impedance which might lead to higher Q_{ext} from the measurements. In the presented simulations the line-impedance of the TEM mode is used as termination impedance of 50 Ω. Unfortunately, there is too few data so that it is hard to draw a significant conclusion from this example.

4.7 Conclusion

In this chapter the combination of a perturbation approach, based on SSC with Newton iteration was presented in order to solve the NLEVP that arises from the computation of external losses for SRF cavities. In investigations restricted to external losses only, it was shown that the proposed method is able to compute multiple eigenpairs even for large systems with several millions of DOFs on a workstation computer. Furthermore, it was shown that the proposed method is applicable to real-life structures that are in use in accelerator physics. Furthermore, the results match solutions computed with other methods (i.e. PF) relatively well. The eigenva-

[22] Unfortunately, one can only verify the eigenvalues using Q_{ext}, not the eigenvectors. Measuring electromagnetic fields inside a closed and cooled down SRF system would require a bead-pull measurements inside a cryogenic module, which is generally not feasible. Furthermore, the measurement of external quality factors as well as their loaded frequencies is theoretically possible yet, it is practically very demanding and not very accurate for high quality factors [93], [94]. Therefore, a common techniques for measuring external quality factors is their extraction from scattering parameter measurements as done in [95].

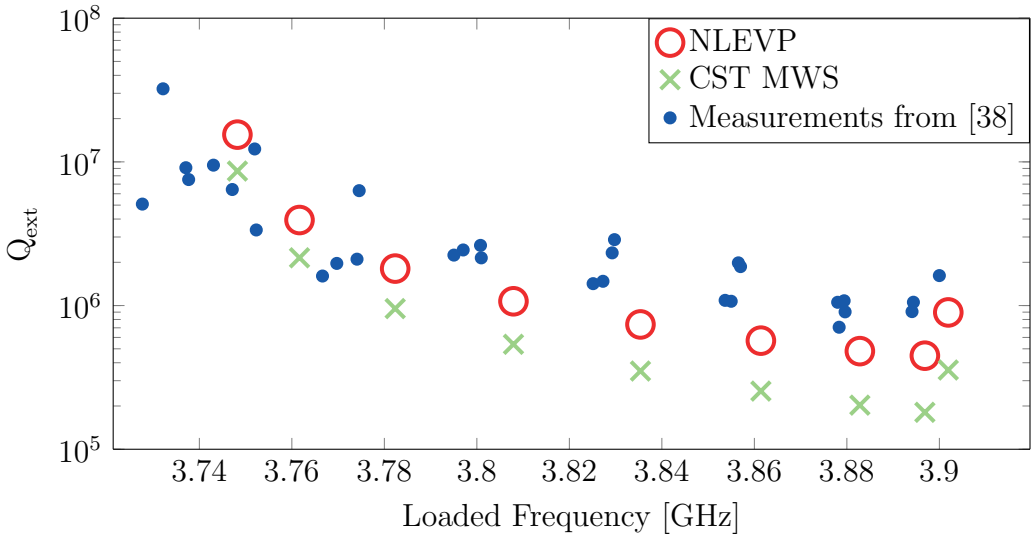

Abbildung 4.11: Comparison between measurements from [95] and computed external quality factors from the NLEVP and from CST MWS for the FLASH cavity. The measurements are restricted to the first monopole band from 3.75 - 3.9 GHz.

lues were validated by prolonging the beam pipes and computing the external quality factors, which remain constant in this case, as to be expected, which is a strong hint for physically consistent of the method. The eigenvalues of the first monopole band were further validated using measurements. The solution of the NLEVP was compared to simplified approaches like linearisation, CST MWS 2014 and PF. For the computation of the eigenvalues (and Q_{ext}) the simplified approaches give reasonable results in most cases, especially the PF worked reliably if given sufficiently many frequency-samples of the S-parameters.

Unfortunately, the comparison of the results to other, straightforward methods is not possible due to the lack of complete documentations regarding computational times, DOFs and computational resources in the literature. Investigations that deal with the computation of external losses in complex SRF structure are (among many others) [6], [70] and [96]. All of them heavily rely on high performance computational infrastructure. To the authors best knowledge, there is not a single article with methods that are able to solve the described problems with several millions of DOFs for large numbers of modes on a workstation computer. Furthermore, all of the cited literature has impractical computational times when a large number of modes has to be computed over a certain spectrum (due to the fact that the modes are not computed at once, but separately or in clusters). Therefore it is concluded that the proposed algorithm contributes to the solution of the NLEVP and thus the computation of external losses on workstation computers.

5 Application Examples

In this chapter, the techniques described in this thesis are used to analyse several real-life, large scale SRF structures. The goal is to show the performance and usability of the described algorithms to solve problems that occur in cutting edge projects from accelerator physics. The software implemented in this thesis was used by the author and several other scientists for various different projects such as:

- FLASH Third Harmonic Module [14],
- European XFEL [15],
- BESSY$^{\text{VSR}}$ [97],
- bERLinPro [98],
- MESA (ongoing, unpublished),
- Future Circular Collider (FCC) (ongoing, unpublished).

In the following, three of these examples (conducted in this thesis) have been selected to further outline the application of the previously derived theory, namely: the FLASH Third Harmonic Module, the bERLinPro main linac and the BESSY$^{\text{VSR}}$ chain of cavities. The following sections are ordered as follows. Firstly, an academic example serves as introduction and shows the necessity to take the entire structure into account. In each following section, one of the practical examples is discussed. Therefore, the structure is briefly described and its requirement for the bigger physical experiment is assessed. Furthermore, a specific problem is stated that can be addressed by the methods described in this thesis. Secondly, some general remarks about the discretization with SSC are discussed and thirdly, the actual results of the solution of the Helmholtz-equation and the NLEVP are discussed. For one example, the results are partly validated using measurements conducted by other scientists.

All computations where done on the same computer as mentioned in Chapter 4.6 (Intel(R) Xeon(R) CPU E5-2687W @3.4 GHz with 256 GB of RAM, running on Windows Server 2012). The SSC models of the substructures are adaptively improved until the relative residual the ROM is below 10^{-12} (with the residual as described in Chapter 3.1.3). For each example, the specific parameters of SSC like the number of mesh-cells, the number of 3D modes, as well as computational times etc. are summarized in the Appendix A. For the solution of the NLEVP, all modes

in the investigated frequency domain were computed with the NM as outlined in Chapter 4.4 with a residual below 10^{-6}. In some cases Q_{ext} is computed to be well above 10^{10}. In real life structures such high quality factors do not exist since the overall quality factors is limited by the intrinsic quality factor of the cavity (probably below 10^{11}). Furthermore, in the following examples the properties of certain modes are discussed. Generally it is not possible to assign r/Q and Q_{ext} to one specific mode since they originate from different computations. In some cases however, an eigenvector of the NLEVP consists predominately of just one mode of the closed structure[1]. Therefore, in some of the examples both r/Q and Q_{ext} are assigned to one mode, which is an approximation that only holds for modes with high Q_{ext} and modes which are dominated by one mode of the closed structure.

For the plots there is no legend or reference amplitude given, since it is not uniquely determined by the Helmholtz equation nor the NLEVP (i.e. the energy and amplitude of the modes in the plots can be freely normalised without violating the underlying equations). Thus, the modes can be scaled arbitrarily. Furthermore, for a more convenient visualization, the color-gradient of the plots is nonlinear.

5.1 Academic Example

The first example is merely investigated to establish the hypothesis that for multi-cavity structures, the investigation of the full structure is in fact needed and that there is no straightforward way to extrapolate the results from computing the resonances for only a subset of the structure. The test structure consists of a cylindric pillbox-resonator, connected by a beam pipe as shown in figure 5.1. Such a structure has no practical relevance in modern particle accelerators and serves solely as example. The resonances of this resonator are compared to a similar structures which contains two pillbox-resonators as depicted in figure 5.2. While the simplified structure looks very similar to the two-resonator structure, its electromagnetic behavior is not the same.

Firstly, the r/Q of both closed configurations is computed in a frequency domain of interest of 0 - 8 GHz. The r/Q for both structures are shown in Fig. 5.3. The results for the single resonator in Fig. 5.1 are highlighted in blue and the results for the full resonator in Fig. 5.2 are highlighted in red. Please note that in order to better visualize the results, all modes with an r/Q below 1 have been omitted in this plot. For a better overview, the 2D cutoff frequencies are displayed in Table 5.1. The first interesting effect can be observed for the modes below 5 GHz. For all of

[1] To clarify this further, the eigenvectors of the NLEVP originating from the open structure, consist of complex-valued weighting coefficients of the eigenvectors originating from the Helmholtz-equation of the closed structure. Thus, if an eigenvector of the NLEVP has one entry which comprises a significant portion of the vectors' absolute value, it can be said that the mode of the NLEVP is very similar to the mode of the closed structure.

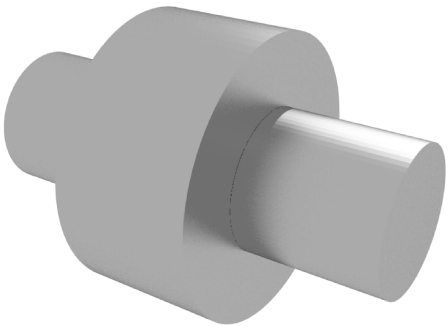

Abbildung 5.1: This picture shows the pillbox resonator with a beam pipe attached on both sides that is investigated in order to show the effects of the concatenation of several resonators.

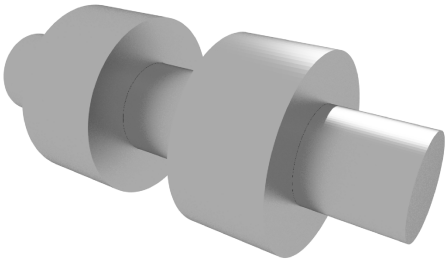

Abbildung 5.2: This picture shows two pillbox resonators with a beam pipe attached on both sides from Fig. 3.4 which are connected with a beam pipe.

Tabelle 5.1: The list of 2D waveguide port modes for the pillbox resonator and its cutoff frequencies. It should be noted that the diameter of the beam pipe is the same on both sides, so only the 2D modes of one port mode are sufficient. The abbreviation *pol.* refers to the polarization of the mode.

Mode	f_{co} **[GHz]**
TE_{11} pol. 1	4.389
TE_{11} pol. 2	4.389
TM_{01}	5.732
TE_{21} pol. 1	7.275
TE_{21} pol. 2	7.275

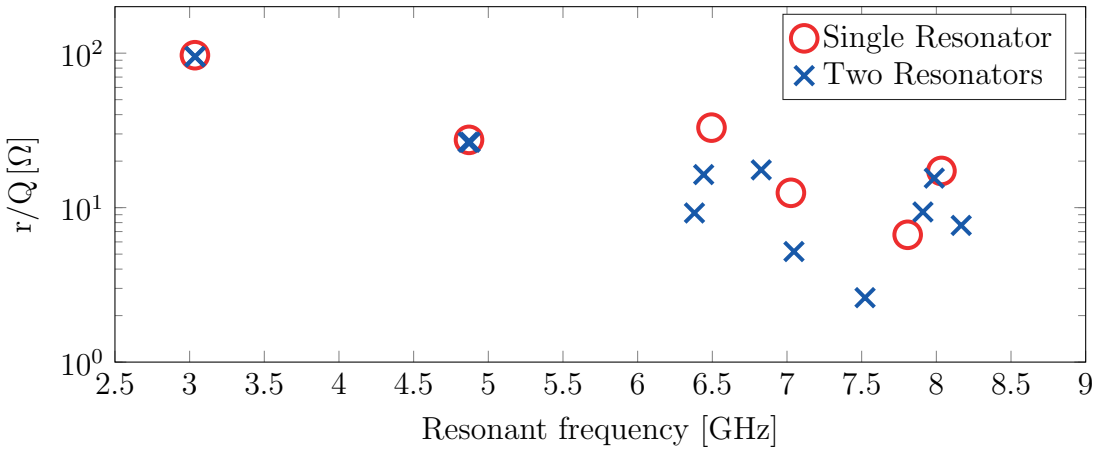

Abbildung 5.3: This picture shows a comparison of the r/Q between the two example resonators from figures 5.1 and 5.2. All modes with r/Q < 1 were omitted for this plot.

these modes (with non-vanishing r/Q), there seems to be hardly any influence on either the frequency or the r/Q , depending whether there are two resonators or only one. As the modes are confined in the pillbox, they are only minorly influenced by the rest of the structure. An example for such a mode is shown Fig. 5.4. Above the first cutoff frequency the modes are not confined to the single pillbox but can couple through the beam pipe, thus through the entire structure as indicated e.g. in Fig. 5.5. It can be seen from the results that above the first cutoff frequency the investigation of the entire structure is inevitable. These modes which are able to couple through the entire structure are further denoted as *multi-cavity modes*. Furthermore, certain modes have hardly any field inside the cavities and are rather located in the beam

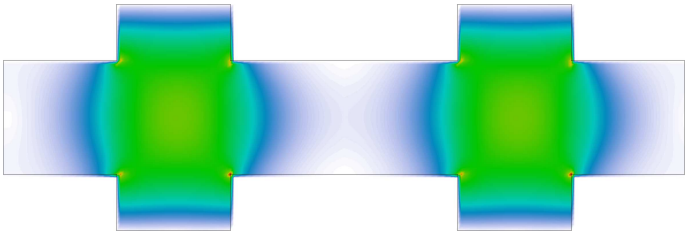

Abbildung 5.4: This picture shows the absolute value of a TM monopole mode computed in the structure shown in Fig. 5.2, resonating at 3.035 GHz with an r/Q of 94.92 Ω. This mode is an example for a mode that does not change substantially in field-pattern, r/Q or resonance frequency if two of the same resonators are concatenated. Therefore, these kind of modes do not require the solution of the Helmholtz-equation in both resonators since the results could be extrapolated from the (computationally less complex) solution of one resonator.

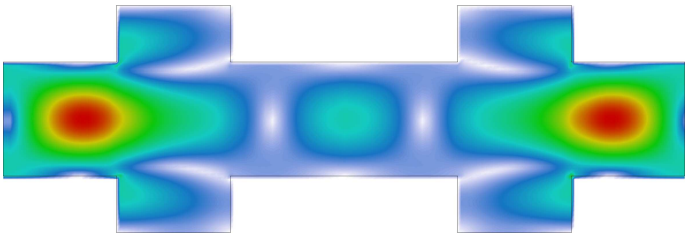

Abbildung 5.5: This picture shows the absolute value of a TM-like mode computed in the structure shown in Fig. 5.2, resonating at 6.383 GHz with an r/Q of 9.23 Ω. This mode is an example for a mode that does not exist if only one resonator is taken into account for the computation (i.e. the structure shown in Fig. 5.1). Therefore, these kind of modes do require the solution of the Helmholtz-equation in the complete structure with both resonators.

pipes between the cavities, these modes are further denoted as *inter-cavity modes*.[2]

5.2 FLASH Third Harmonic Module

The Free-electron laser in Hamburg (FLASH) is a user facility providing soft X-rays and extreme ultraviolet light. A subpart of the layout of the accelerator is highlighted in Fig. 5.6.

There, especially interesting is the so-called Third Harmonic Module which is a subpart of the accelerating structure. Its goal is to improve the quality of the bunch compression by linearising the phase space of the beam in longitudinal direction [100]. Therefore, the resonance frequency of the π-mode of the Third Harmonic

[2] A similar investigation of this simplified structure using Q_{ext} does not make much sense, since a lot of values would be theoretically infinite.

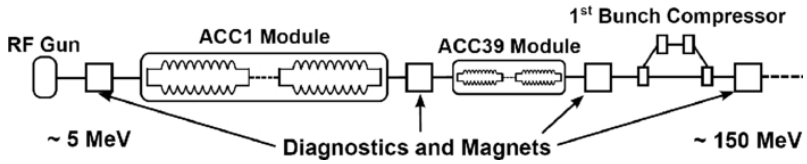

Abbildung 5.6: In this picture a sketch of the experimental setup for the FLASH injector is shown. It consists mainly the accelerating module ACC1, the Third Harmonic Module ACC39 and a bunch compressor [99].

Module is chosen to be a higher-harmonic of the resonance frequency of the π-mode of the basic 1.3 GHz cavity. Hence, 3.9 GHz were chosen. The module consists of four SRF cavities (mounted in one cryomodule), which are installed downstream of the main linac, but before the bunch compressor, as depicted in Fig. 5.6.

The Third Harmonic Module has been extensively investigated using numerical tools in the literature prior to this thesis. Firstly, there have been studies that investigate only one cavity and neglect the coupler in order to analyse the band structure of the modes inside the cavity [91]. The single cavity with couplers has been investigated in depth in [87], [99] (to name only a few), and with all four cavities but without couplers in [101]. Furthermore, the module was investigated in full (with all four cavities and couplers) with Omega3P in [54] but unfortunately no external losses were computed and the bellows were neglected. Lastly, the structure was investigated for its external losses and r/Q with all four cavities and couplers using SSC in [8] but some minor simplifications regarding the rotation of the power coupler. The investigation in this thesis tries to close the gap and comprise all prior investigations by computing Q_{ext} and r/Q similar to [8] but with the solution of the NLEVP instead of a linearised problem and with the correct rotation of the power coupler.

5.2.1 Application of SSC to the FLASH Third Harmonic Module

The structure consists of several repetitive substructures. Firstly, there are four SRF cavities with a π-mode frequency of 3.9 GHz. Each of the cavities is accompanied by two couplers, one HOM coupler and one input coupler with a HOM coupler attached. This coupler-cavity combination is depicted in Fig. 5.7. The combination of cavity with coupler is not the same for all four cavities. While the coupler structure is always the same, the coupler is in some cases mirrored and/or rotated. For a specific description of the structure it is referred to [102].

The structure in Fig. 5.7 is slightly simplified compared to the real-life structure operated at DESY. Firstly, the power coupler and HOM coupler pair is modified due to the issue with the practical implementation that waveguide ports have to

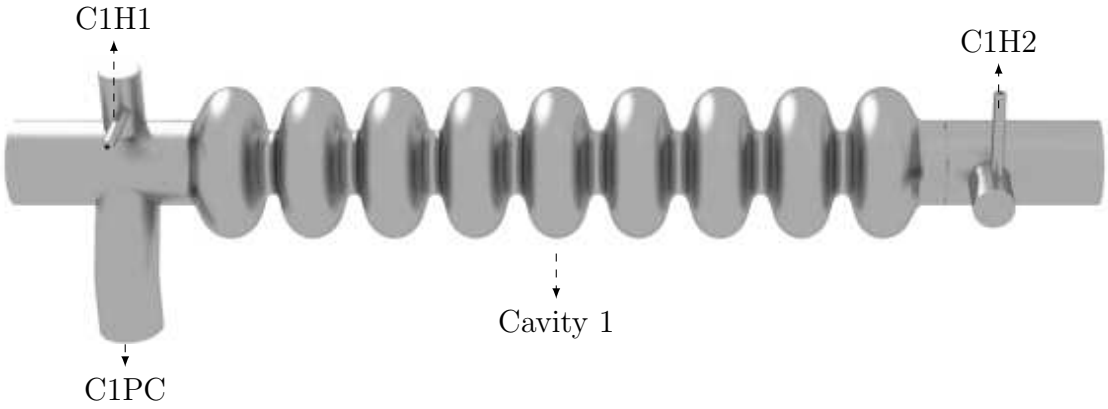

Abbildung 5.7: This picture depicts an example structure with a nine-cell 3.9 GHz cavity, a HOM coupler and a combined HOM coupler and input coupler. This structure is a part of the Third Harmonic Module from [90],[103]. For compatibility, the naming convention of the ports is taken from [95]. The Third Harmonic Module consists of four of such modules with different rotation of the attached couplers. All four modules are connected by bellows.

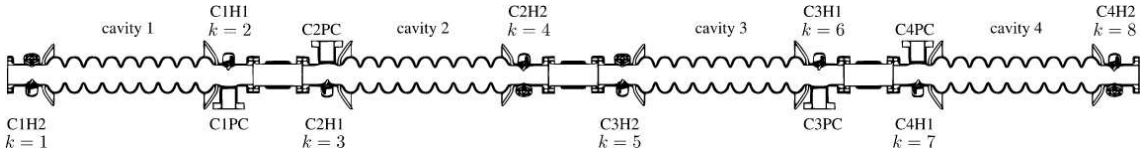

Abbildung 5.8: This picture shows a CAD model of the entire FLASH Third Harmonic Module. The structure consists of four cavities, with cavity 2 and 4 being similar to the cavity in Fig. 5.7. The cavities 1 and 3 are minorly varied from this design with a mirrored design. The graphical depiction is taken from [104].

be aligned with a Cartesian coordinate system to avoid large geometrical errors in the numerical simulation. Therefore, the coaxial part of the HOM coupler is bent in such a way that it is aligned like this while the cross section of the coaxial pipe remains the same along the bend.[3] The four cavities with attached couplers are connected by three bellows in total. In a real-life application, the bellows are normal conducting. However, for the simplicity of the solution, they are (throughout all following investigations) assumed to be superconducting and without surface losses. The full structure is depicted in Figure 5.8.

5.2.2 Results FLASH Third Harmonic Module

In this subsection the results for FLASH are discussed. In this thesis all eigenmodes for the FLASH Third Harmonic Module (as shown in Fig. 5.8) where computed in

[3]This variation of the structure should only change its RF properties minorly.

a frequency range from 0 - 8 GHz for the closed structure. The entire computation took roughly 11 h and 33 m. Furthermore, the NLEVP was solved in 18 h and 7 m in the same frequency domain. The solutions are shown in Fig. 5.9.[4]

As mentioned earlier, the full set of results is quite complex so only a small subset of them are discussed here. Of special interest are the modes with relatively high Q_{ext} and/or r/Q .

Of major interest for accelerating particles are the four π-modes[5]. These four modes have the highest r/Q of all modes with a mean of roughly 742.29 Ω which fits comparably well to the value computed in [99] of 747.8 Ω[6] and deviates by roughly 1% from the design value of 750 Ω [105]. The Q_{ext} of the π-modes is computed as $1.26 \cdot 10^6$ which is a 3% deviation from the design value of $1.3 \cdot 10^6$ [105].

Furthermore, the two modes resonating at 4.137 GHz are interesting due to their high quality factors. They both have roughly the same quality factor of $5.1 \cdot 10^6$ and $5.2 \cdot 10^6$, respectively. However, their r/Q of $< 0.1\,\Omega$ is comparably small.

A further interesting group of modes are resonating between 5 - 5.25 GHz. These modes are not located inside the cavities but resonate inside the bellows. Some of them have quality factors $> 10^4$ and might be potentially dangerous. The mode with the highest quality factor of $5.9 \cdot 10^6$ has a resonance frequency of 5.1524 GHz.

The mode with the highest r/Q (despite the π-modes) of 226.5 Ω is resonating at 7.6530 Ghz. This mode is particularly interesting since it supports some of the hypotheses given in this thesis. Since this mode seems comparably dangerous to the beam quality it needs to be computed very accurately. At the same time, it can couple through the entire chain of cavities which indicates that for an accurate computation the investigation of the full chain is inevitable.

5.2.3 Comparison of SSC Simulations to Measurements

In this subsection the obtained results for the FLASH Third Harmonic Module are compared to measurements conducted in [95]. Therefore the scattering parameters from measurement and numerical computation via SSC are compared. Unfortunately, the CSC-results from [95] are not available for comparison.

[4] The dedicated reader will notice a big discrepancy between the computed r/Q in [54] and Fig. 5.9 even though the structures on which both computations are based are nearly the same. The difference might originate in a different definition of the r/Q for multipole-modes. In this thesis however, a definition that is more common in literature such as [99], [101] and [8] is used.

[5] As mentioned earlier, the decomposition in four, mutually orthogonal π-modes is not unique.

[6] The investigation in [99] does not take the couplers into account which might explain the deviations. Furthermore, the r/Q is computed using an additional factor of 1/2, hence the actual number given is 373.9 Ω.

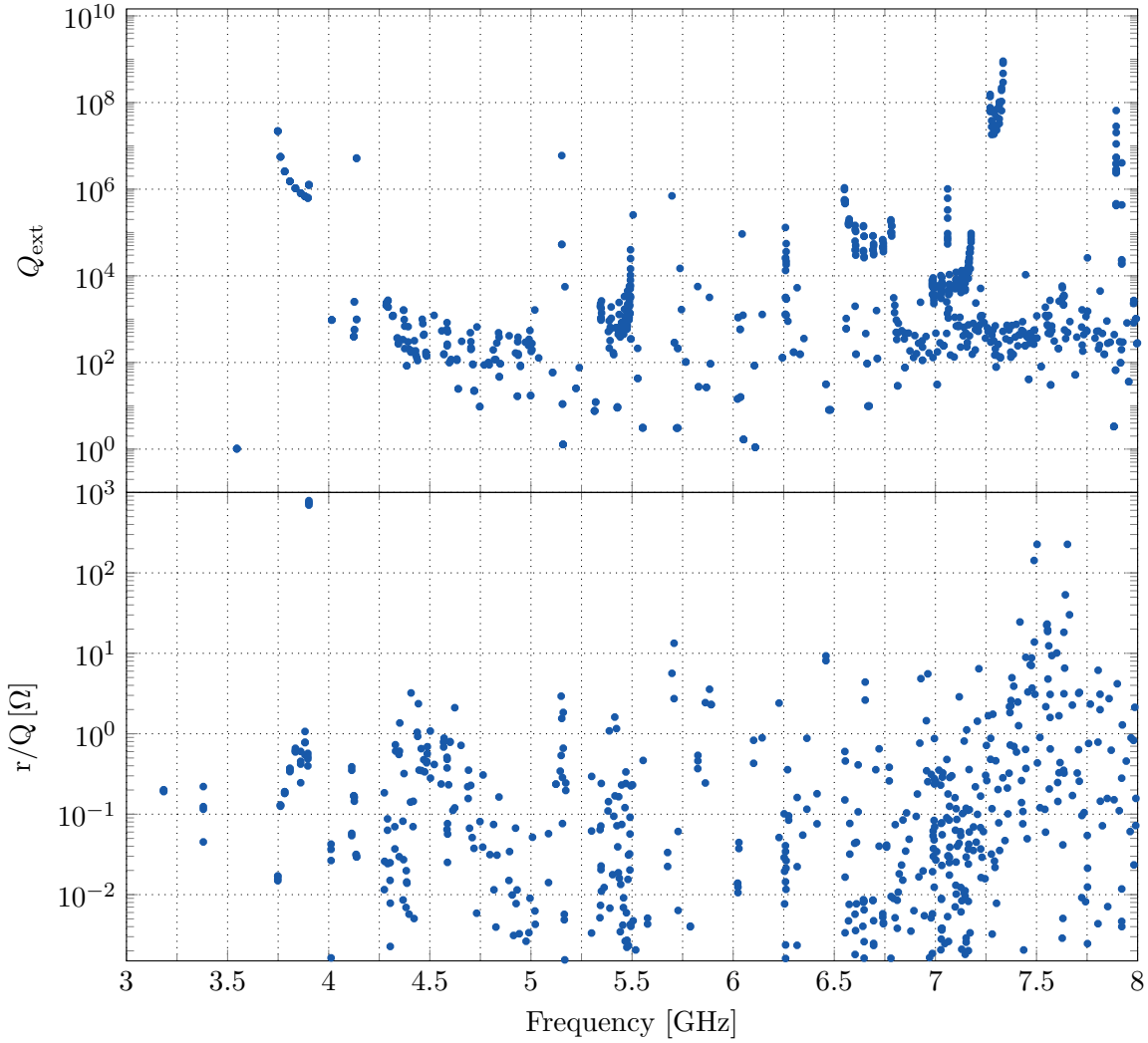

Abbildung 5.9: This plot shows the results computed for the FLASH Third Harmonic Module shown in Fig. 5.8. The computed values are shown for Q_{ext} (upper plot) and r/Q (lower plot). When computing the r/Q, the modes are computed for the closed structure (since r/Q is not defined for open structures), while Q_{ext} is computed for frequency-matched port-boundary conditions. Therefore, a comparison of both values is only reasonable for high Q_{ext} (since in that case the mode hardly couples to the port boundary and is not changed by it). Furthermore, it should be noted that both plots share the same x-axis. For a better overview, modes with a frequency below 3.0 GHz and eigenmodes with a very low computed quantity ($Q_{\text{ext}} < 10^{-1}$ and r/Q $< 10^{-3}$) have been omitted in this plot.

The measurements of the S-parameters were conducted by connecting cables (in some cases several meters long) to all the HOM couplers, which affects the measurements in a non negligible way. Therefore, to conduct a valid comparison, the effects

of the cables have to be added to the simulation[7]. For the sake of simplicity, the comparison is restricted to the absolute value and the phase is neglected from hereon. Since the exact measurement of the cables is not readily available, the effect of the cables is very roughly fitted in [95] with an exponential function

$$20 \cdot \log_{10}|S_{1,2,\mathrm{Cable}}| = -0.3f + 0.61. \tag{5.1}$$

For simplicity, it is assumed that all cables are the same. In order to account for this difference, the SSC scattering-parameters are multiplied twice[8] with the transmission-function of the cable in order to make it comparable to the measured scattering parameters. This leads to the computed transmission functions of the scattering parameters, transformed into the measurement setup as

$$|S_{\mathrm{tm}}| = |S_{1,2,\mathrm{Cable}} \cdot S_{\mathrm{SSC}} \cdot S_{1,2,\mathrm{Cable}}|. \tag{5.2}$$

It is emphasized again that (5.2) only holds for transmission functions. Furthermore, (5.2) is heavily simplified since it assumes that the cables are only attached to the ports that were measured and all other ports were left open. A more accurate way, would be to attach a SSM of the cable to each port they were connected to during the measurement.

The results are presented by the comparison of two example spectra as shown in Fig. 5.10 and 5.11. For both comparisons the S-parameters were computed on 5,000 equidistant frequency-samples from 3.5 - 8 GHz, while the measurements were conducted on 45,001 frequency-samples in the same frequency domain. For both plotted measurements, due to the accuracy of the network analyser for the given measurement time, the measurement of S-parameters below -100 dB was not feasible. For a thorough description of the measurement setup it is referred to [95]. A discussion of possible explanations for the discrepancies between measurements and results is given in the Appendix B. For both shown comparisons, there is a qualitative agreement between measurements and computations. Generally, the measurements seem to have a higher complexity, meaning there are more peaks and more noise than in the simulation. It should be noted that the dispersion characteristics (e.g. the width of a dipole band) is not extractable from the measurements because there is no way of actually measuring the field such that a multipole expansion is possible. It is rather assumed that the measured structure does not vary too much from the simulated one such that the multipole expansion can be carried out in a preprocessing step as in [91].

In Fig. 5.10 the transmission through cavity 2, more precisely the S-parameter from the TEM mode of the HOM coupler C2H2 to the TEM mode of the HOM

[7] Another possibility is to artificially remove the effect of the cables from the measurements which should lead to the same comparison.

[8] The signal goes back and forth through the cable.

coupler C2H1, is plotted once computed with SSC marked in red and once measured in [95], marked in blue.

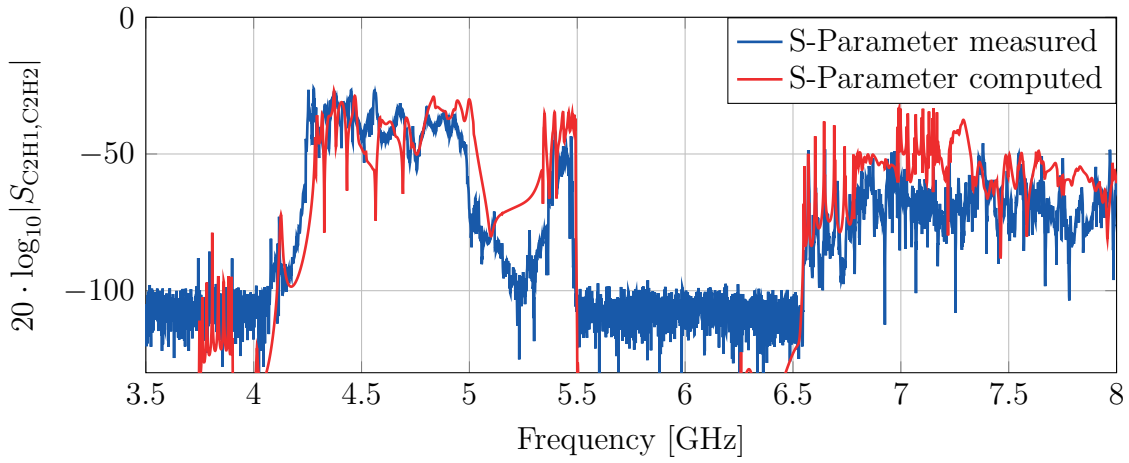

Abbildung 5.10: This picture shows the comparison between measurements and computations for $|S_{C2H1,C2H2}|$, i.e. the absolute value of the transmission from the left HOM coupler of cavity 2 to the right HOM coupler of cavity 2 (see Fig. 5.8). The measurements are further described in [95].

Firstly, the measurements and the computations in Fig. 5.10 show a qualitative agreement, most features of the curves are present in both measurements and computations. For both, the first monopole band of the cavity is located from 3.75 - 3.9 GHz, with the π-mode at 3.9000 GHz in the measurement and 3.9019 GHz in the simulation, which makes a difference of 1.9 MHz.[9]

From roughly 4.27 - 4.9 GHz one can see the first TE dipole band of the cavities. These modes are able to propagate through the entire chain of cavities. It appears that while the transmission is roughly the same in both measurements and simulations, the entire band is slightly shifted up in frequency by roughly 40 MHz. The origin of this shift is unclear. A possible explanation could be the sensitivity of dipole modes to differences in the structure. During the measurement the ACC39 is attached to the FLASH chain of 1.3 GHz cavities and it is very likely that the dipole modes can couple out of ACC39 to the rest of the accelerating cavities which might change their frequencies. Unfortunately, this coupling could not be taken into account in the simulation and could not be negated in the measurement since the Third Harmonic Module would have to be physically detached from the rest of the of the accelerator which is not feasible.

Modes from the second TE dipole band resonate from roughly 5.35 - 5.49 GHz in the simulations which coincides very well with the simulations of the dispersion

[9] This difference might very well be caused by the tuning of the cavity, which deliberately changes the π-mode frequency.

characteristics in [91]. In the measurements, this band is more narrow from 5.367 - 5.487 GHz and its transmission is worse by 10 - 20 dB than in the simulations.

From 5.5 - 6.5 GHz there are no modes in the natural band structure of the cavities which is reflected by the measured S-parameter being at the noise floor at these frequencies. The simulation shares this characteristic.

The first TE quadrupole band is located at roughly 6.56 - 6.70 GHz in both simulations and measurements. For this specific band the measurements and simulations agree very well regarding the resonant frequencies.

For frequencies above 6.5 GHz a detailed comparison is hardly feasible due to the complexity of both spectra. Generally, it can be said that the simulation appears to have a slightly better transmission than the measurement.

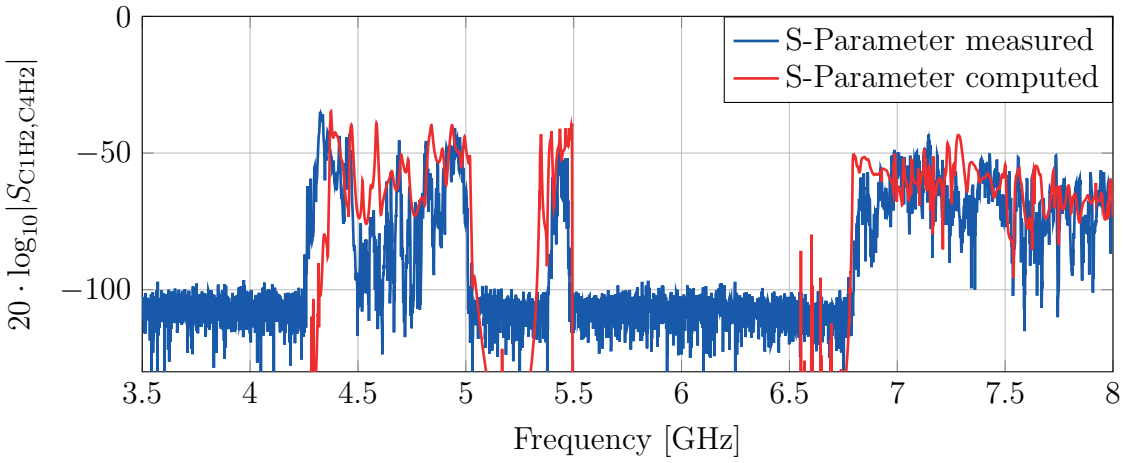

Abbildung 5.11: This picture shows the comparison between measurements and computations for $|S_{C1H2,C4H2}|$, i.e. the absolute value of the transmission from the HOM coupler attached to cavity 1 to the HOM coupler attached to cavity 4 (see Fig. 5.8). The measurements are further described in [95].

In Fig. 5.11 a second example is shown, specifically the transmission from the second HOM coupler of cavity 1 to the second HOM coupler of cavity 4, i.e. $S_{C1H2,C4H2}$. This comparison is particularly interesting since it measures the transmission through all four cavities (while the comparison in Fig 5.10 is only through one cavity). Generally, it can be said that the results show a qualitative agreement but seemingly the results align a little worse than the comparison through one cavity. Especially the width of the multipole bands differs drastically between measurements and simulations. Interestingly, the same is observed in [95].

5.3 Main Linac of bERLinPro

The Berlin Energy Recovery Linac Prototype *bERLinPro* is a planned Energy Recovery Linac (ERL) at the Helmholtz-Center in Berlin (HZB). The basic idea of an ERL is to have relatively high beam currents in an electron beam and a high brilliance[10] (just as in a linac) in order to produce X-rays by synchrotron radiation. The major difference to a linac is the recirculation of the beam by a magnetic lattice through the accelerating structure (with a phase change of 180° relative to its initial passing) in order to reuse its kinetic energy[11]. ERLs generally have comparably high repetition rates and spectral radiance. bERLinPro is planned to demonstrate the feasibility of the ERL technology as well as develop expertise for the next-generation light sources and would be (as of the publication of this thesis) the second fully functional ERL in the world. Due to the high beam current the demands on HOM damping are very high for bERLinPro which makes it an interesting application for the methods developed in this thesis.

In this example the main linac of the current design of bERLinPro is investigated. The structure is shown in Fig. 5.12. The investigated domain consists of three 1.3 GHz cavities, each equipped with two couplers. The three cavities are connected by bellows and both upstream and downstream the structure is terminated with a HOM absorber and a taper. For this investigation however, both tapers and HOM absorbers were neglected. Each of the three cavity-coupler pairs (as depicted in Fig. 5.13) consists of one cavity (all three cavities are the same), a waveguide HOM coupler and a combination of input coupler and waveguide HOM coupler. The spatial rotation as well as the ordering of the couplers varies between the three cavity-coupler pairs. In investigations prior to this one, the possible designs were reduced to two candidates that are shown in Fig. 5.14 (further denoted as design 1) and Fig. 5.15 (further denoted as design 2). The task of this investigation was, to solve the Helmholtz-equation and the NLEVP for both structures and assess their electromagnetic properties like r/Q and Q_{ext} to show that there are no dangerous modes and to compare the two design candidates.

It was an open question how the designed cavities would interact inside the cryomodule if three cavities were present as shown in Fig. 5.14 and 5.15. Firstly, this was investigated using wakefield calculations [106], [107]. Since these kind of investigations do not allow for the computation of external losses or field distributions, the following investigation were highly needed. Furthermore, modes with high external

[10] The brilliance is a measure to compare the quality of X-ray sources. It is proportional to the density of photons of a certain wavelength and direction per unit time [9].

[11] The recirculation of the beam through the accelerating structure is also applied in a storage ring. In contrast to a storage ring, the ERL does not use the recirculated beam for the generation of synchrotron radiation, which would lead to an emittance growth, hence a reduction of beam-quality over time. Basically, for an ERL, the beam is used only once, but its energy is used multiple times.

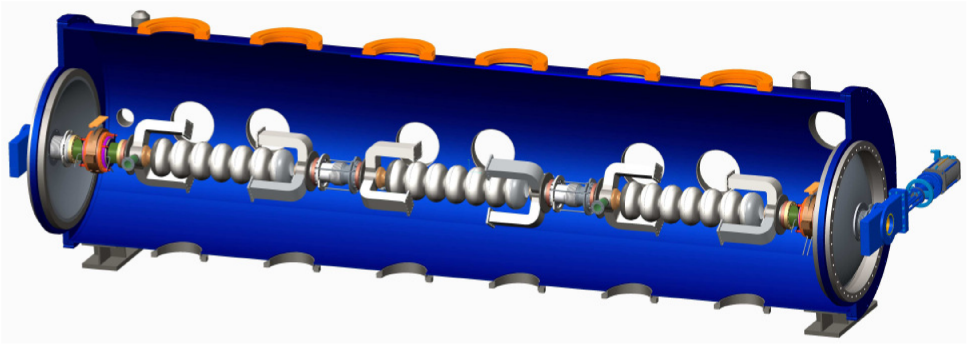

Abbildung 5.12: This picture shows a sketch of the main linac of bERLinPro [106]. The three cavities are connected by bellows and both upstream and downstream the structure is terminated with a HOM absorber and a taper.

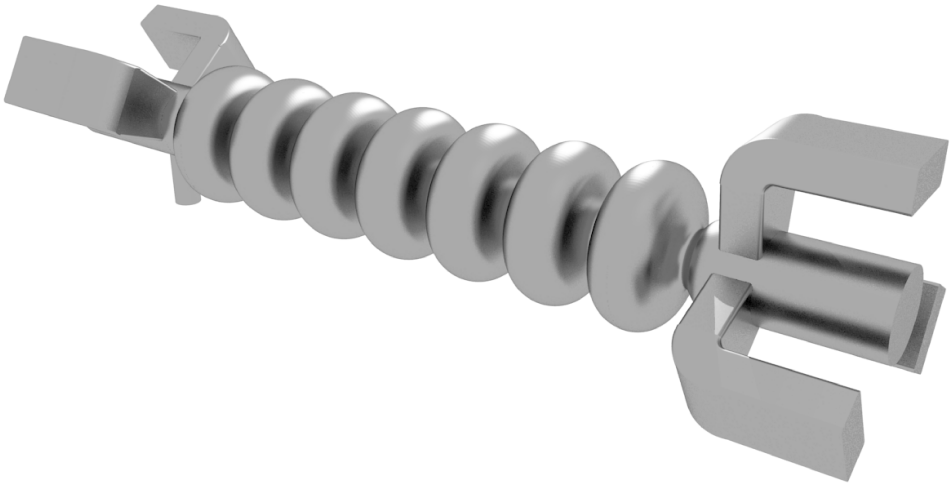

Abbildung 5.13: This picture shows a single cavity-coupler pair of the bERLinPro linac. It consists of one 1.3 GHz cavity, equipped with two couplers.

quality factors are harder to detect if the simulated wakelength is not sufficiently high.

While the cavity design itself was fixed, the ordering and rotation of the couplers was of special interest. Therefore, two possible permutations were given by the HZB which were to be investigated in a frequency range of interest from 1 - 4 GHz. Here it should be investigated if any dangerous modes result in the concatenation of the three cavities. Of special interest are potentially dangerous modes at the beam repetition rate, e.g. at frequencies that are close to integer multiples of the frequency of the π-mode (e.g. 2.6 GHz and 3.9 GHz).

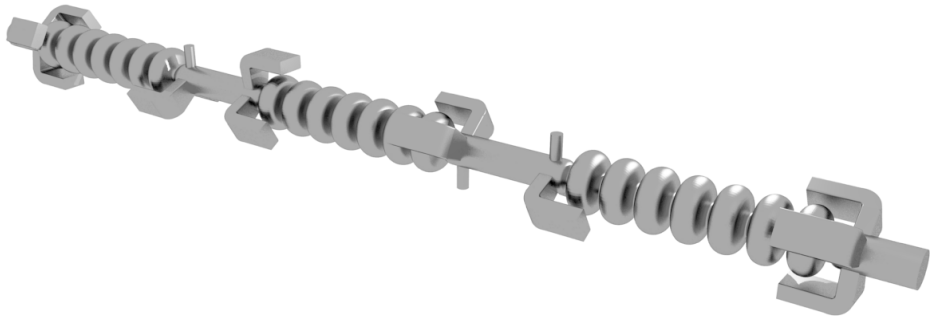

Abbildung 5.14: This picture shows the first design candidate that is investigated. It consists of three cavities with a HOM coupler and a combination of HOM and input coupler. All three cavity-coupler pairs are mirrorings and/or rotations of the structure shown in Fig. 5.13.

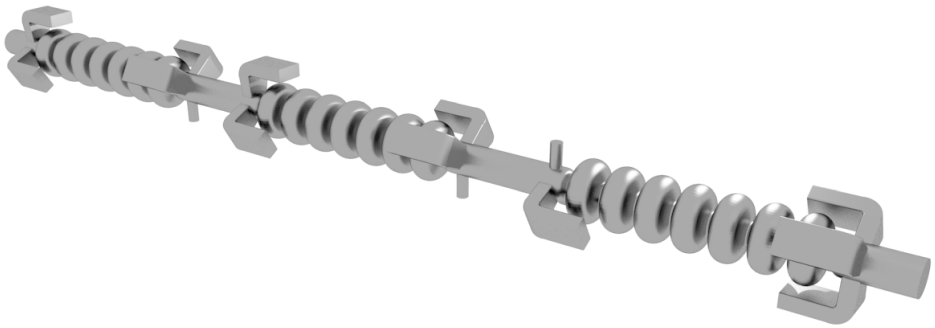

Abbildung 5.15: This picture shows the second design candidate that is investigated. It consists of three cavities with a HOM coupler and a combination of HOM and input coupler. All three cavity-coupler pairs are mirrorings and/or rotations of the structure shown in Fig. 5.13. The second design differs from the first design by the rotation of one cavity-coupler pair (the very left in this picture) by 180° around the beam-axis.

5.3.1 Application of SSC to bERLinPro

In a first step, a sufficiently good decomposition of the structure is determined. As mentioned earlier, the decomposition should be done in a way, that many, sufficiently small structures can be used several times. The standard approach is to decompose the structure into its cavities and couplers separately. Obviously, the cavity domain is chosen in a way that the SSM has to be computed only once. Then the remaining coupler are decomposed in a way that their models can be used as often as possible. The structure was decomposed into nine distinct segments; a cavity, four HOM couplers (the coupler is always the same but it is rotated in four different ways) and four input-HOM coupler combinations (again the coupler is the same but has four different rotations). The parameters of the decomposition such as mesh cells or number of 3D eigenmodes are summarized in Appendix A.2.

5.3.2 Results bERLinPro

In this subsection, the results of the investigation of bERLinPro are described and the two designs proposed by HZB are compared. Fig. 5.16 shows the Q_{ext} and r/Q of both designs in comparison in a frequency domain from 1 - 4 GHz. The complete solution of the Helmholtz-equation and the NLEVP for design 1 took roughly 2 d 5 h and 18 m. The computational time for design 2 was roughly the same.

Evaluating Fig. 5.16 one can see that the two designs hardly differ, regarding their Q_{ext} and r/Q . The modes with the highest r/Q are the three π-modes with a mean r/Q of the three modes of 769.30 Ω for Design 1 and 769.50 Ω for Design 2. One of these modes is depicted in Fig. 5.17 for Design 1. An important property for ERL cavities (due to the high HOM damping requirements), to avoid modes that can couple well to the beam in the vicinity of multiples of the π-mode frequency (i.e. 2.6 and 3.9 GHz in this case). This is fulfilled for both designs. Below 2.3 GHz, both designs appear to be nearly equal. In contrast to e.g. the results for the FLASH Third Harmonic Module (depicted in Fig. 5.9) there appear to be no dangerous inter-cavity modes in between the cavity bands that emerge from the concatenation of several cavities. There are however, modes that can couple through the entire chain of cavities, especially from the first TE dipole band. An example for one of these modes is depicted in Fig. 5.18, resonating at 1.8564 GHz.

As mentioned earlier, it is especially important to avoid modes with high interaction with the particle beam (i.e. r/Q). For both designs the mode with the highest r/Q is located in the second TM monopole band and resonating at roughly 2.42 GHz. Interestingly, this mode differs in r/Q with 203 Ω for Design 1 and 279 Ω for Design 2, being roughly 30 % higher for Design 2. Furthermore interesting is a mode located at roughly 2.42 GHz which has an r/Q of 45 Ω for Design 1 and 30 Ω for Design 2, which is roughly 33 % higher for Design 1. Regarding the Q_{ext} there are major differences in both designs for the first TE monopole band located roughly from 2.48 - 2.49 GHz.

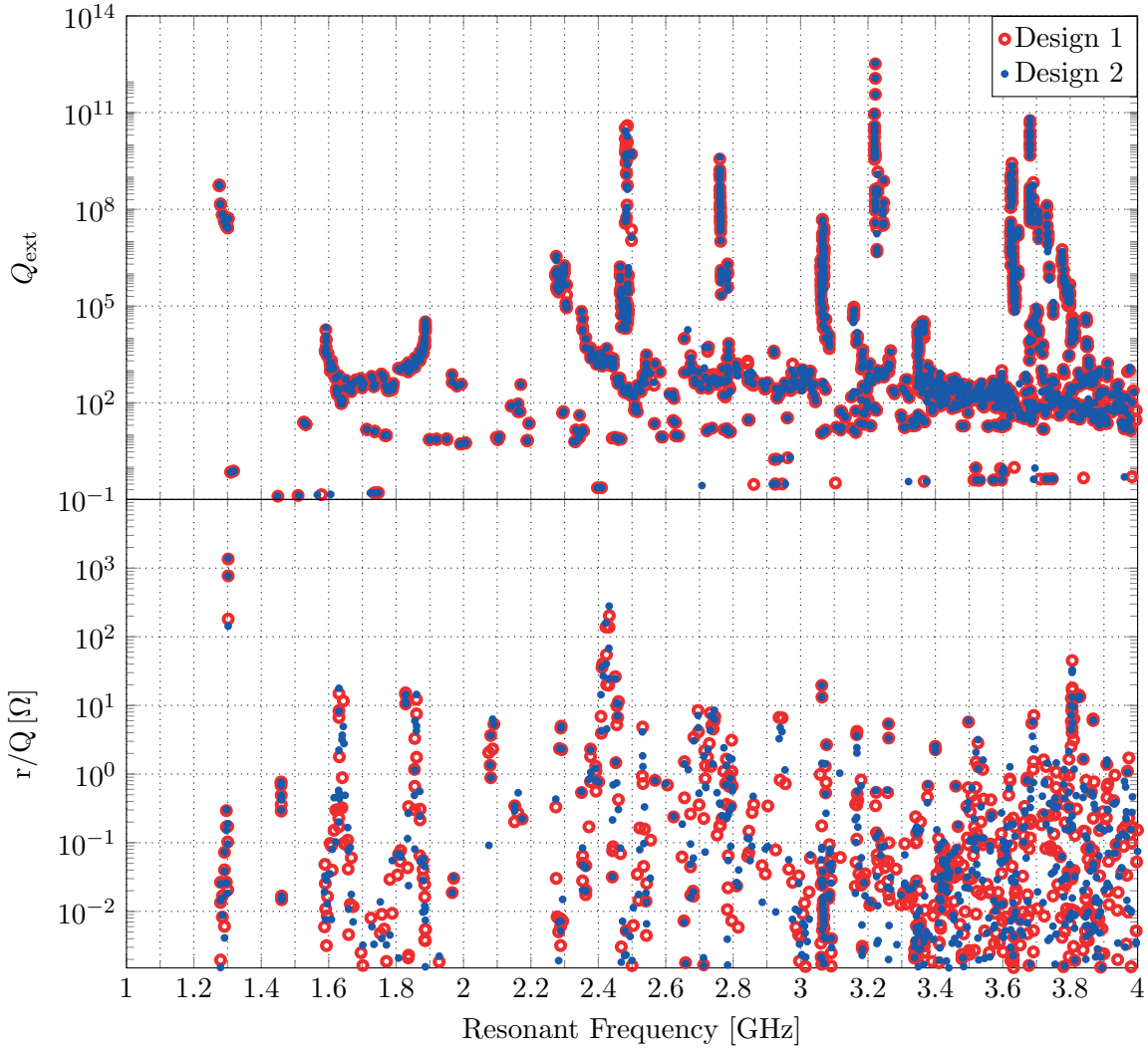

Abbildung 5.16: This plot shows the results computed for the chain of cavities for bERLinPro shown in Fig. 5.14 for design 1 and Fig. 5.15 for design 2. The computed values are shown for Q_{ext} (upper plot) and r/Q (lower plot). When computing the r/Q, the modes are computed for the closed structure (since r/Q is not defined for open structures), while Q_{ext} is computed for frequency-matched port-boundary conditions. Therefore, a comparison of both values is only reasonable for high Q_{ext} (since in that case the mode hardly couples to the boundary and is not changed by it). Furthermore, it should be noted that both plots share the same x-axis and legend. For a better overview, modes with a frequency below 1.0 GHz and eigenmodes with a very low computed quantity ($Q_{\text{ext}} < 10^{-1}$ and r/Q $< 10^{-3}$) have been omitted in this plot.

Generally, one can conclude that both designs show no signs of dangerous modes

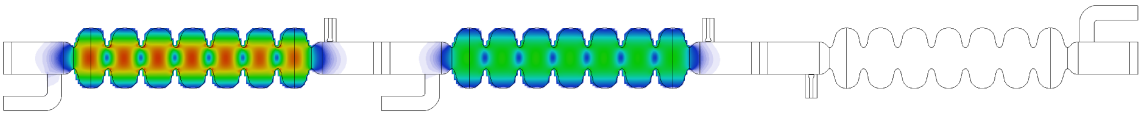

Abbildung 5.17: This picture shows the absolute value of the electric field of one of the three π-modes of the Design 2 of the bERLinPro main linac. The mode resonates at 1.3017 GHz with an r/Q of 1398.932 Ω. The solution of the NLEVP delivers a mode that consists solely of the lossless π-mode, with a Q_{ext} of $5.301 \cdot 10^7$.

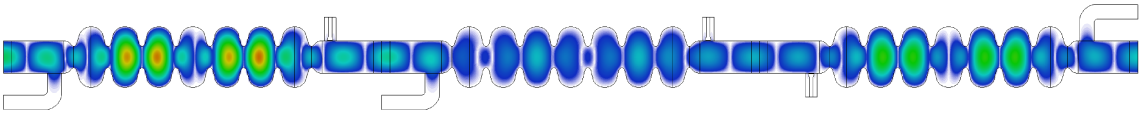

Abbildung 5.18: This picture shows the absolute value of the electric field of a multi-cavity mode of the first dipole-band of the Design 2 of the bERLinPro main linac. The mode resonates at 1.8564 GHz with a negligible r/Q of $< 1 \cdot 10^{-5}$ Ω. This mode is particularly interesting since it can traverse through the entire structure.

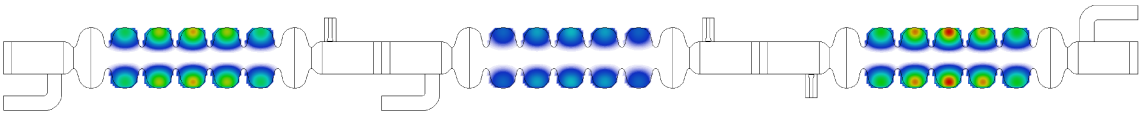

Abbildung 5.19: This picture shows the absolute value of the electric field of the mode with the highest Q_{ext} of the first TE decapole-band of the Design 2 of the bERLinPro main linac. The mode resonates at 3.6807 GHz with a Q_{ext} of $5.301 \cdot 10^7$.

in the vicinity of the higher harmonics of the π-mode frequency. Furthermore, even though the designs are comparably similar, the rotation of one of the cavities (including the input coupler), changes the r/Q of some modes. This effect should be part of future investigations.

5.4 BESSY^{VSR}

The variable pulse length synchrotron radiation source BESSY^{VSR} is an upgrade of the BESSY II storage ring in Berlin at the HZB. BESSY II is a 1.7 GeV storage ring, operational since 1998 [108]. In order to satisfy the user demands for shorter pulse lengths in combination with relatively high beam currents of 300 mA, the facility needs to be upgraded. To achieve this, the storage ring is planned to be filled with short bunches of 1.5 ps rms-length and long bunches of 15 ps rms-length simultaneously [108], [109].[12] Therefore, two SRF cavity systems[13] are to be installed in the normal conducting BESSY II ring. The resonance frequencies of the π-modes of these cavity systems are designed to be 1.5 GHz and 1.75 GHz as denoted in Fig. 5.20, which is supposed to generate a so-called "beating-patternïn the voltage, seen by a charged particle bunch as denoted in Fig. 5.21.

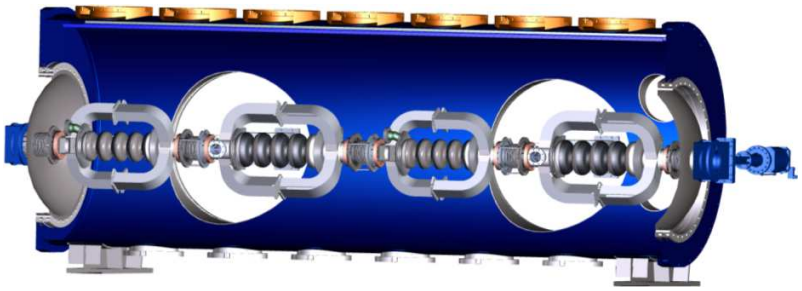

Abbildung 5.20: This picture shows the potential addition of a cryomodule to the BESSY II ring. The additional cryomodule will be filled with several SRF cavities of higher-harmonic π-mode frequencies to the 500 MHz BESSY II π-mode frequency, enabling the simultaneous storage of bunches of different lengths. The picture is taken from [110].

In the recent development of the project, four four-cell cavities have been designed by the HZB prior to this investigation [2], [111] (to name only a few). While two cavities are designed to have a resonance frequency of the π-mode of f_π =1.5 GHz, the other two have a resonance frequency of the π-mode of f_π =1.75 GHz.

5.4.1 Application of SSC to BESSY^{VSR}

The structure is subdivided into thirteen substructures. The two tapers, the valves with dipole-coupler and several variations of the cavity-coupler pairs and bellows. In this example the cavities and couplers are discretized in a single substructure (opposed to the procedure in the first two examples) since there is no constant cross section between the cavity and the HOM couplers. Therefore, the computation of

[12] It is a common practice in accelerator physics to refer to the length of a charged particle beam in seconds. With the velocity of the bunch, this can be converted to an actual length in meters.
[13] Cavity systems in that sense, that there might be one or more, cavities installed in each.

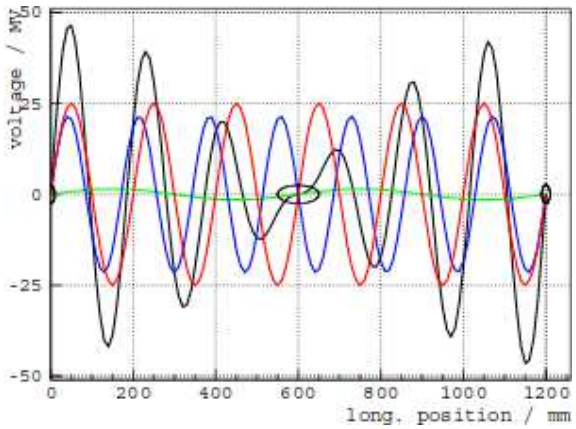

Abbildung 5.21: This picture shows the desired voltage in black, as seen by an ultra-relativistic bunch passing through the cavities with different π-mode frequencies. It consists of the voltage of the 0.5 GHz cavity in green, of the 1.5 GHz cavity in red and the 1.75 GHz cavity in blue [108]. The resulting voltage is able to provide a stable acceleration for particle bunches of varying bunch lengths.

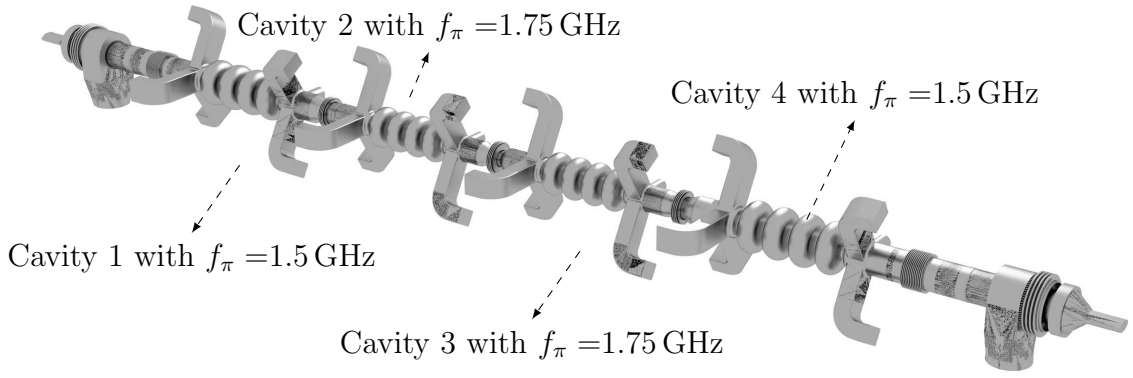

Abbildung 5.22: This picture shows a CAD model of the BESSY$^{\text{VSR}}$ structure which consists of two 1.5 GHz cavities (cavity 1 and 4) and two 1.75 GHz cavities (cavity 2 and 3). The cavity-coupler pairs are connected via bellows (all of which have a slightly different geometry). The structure is enclosed up- and downstream with a taper and a valve.

the MOR of the cavity-coupler pairs is comparably slow. The full separation is documented in the Appendix A.3.

In the tapers there is some lossy, dielectric material. Unfortunately, the current implementation of SSC does not allow for the simulation of lossy materials. The material losses can be modeled using a complex permittivity as

$$\varepsilon = \varepsilon'(\omega) - j\varepsilon''(\omega) = \varepsilon'(\omega) - j\frac{\kappa(\omega)}{\omega}. \tag{5.3}$$

In this simulation, both the frequency dependence of the real part of ε as well as the imaginary part of ε are omitted, simplifying (5.3) to $\varepsilon = \varepsilon'(\neq f(\omega))$. In the future, it might be advantageous to re-simulate the structures' electromagnetic behavior using the non-simplified material properties. Especially for modes being located inside the taper, the computed properties like losses or resonance-frequencies might be very inaccurate due to the chosen simplification[14].

5.4.2 Results BESSY^{VSR}

The results consist of the modes' interaction with an ultra-relativistic particle beam (r/Q) as well as their external losses (Q_{ext}). These results are shown in Fig. 5.23. In the following, firstly some general remarks are given about the results and secondly, some interesting modes (or groups of modes) are discussed. There were 1,576 modes found from 0.5 - 3.6 GHz. The computations as shown here took roughly 6 d and 2 h.

Regarding the interaction with a particle beam, the overall results do not hint to any mode that could drastically endanger the beam quality. For all modes but the π-modes of the 1.5 GHz and 1.75 GHz the r/Q is below 11 Ω. Especially close to multiples of the bunch repetition rate (i.e. 1.3 GHz and 2.6 GHz) all modes have a low r/Q . The external losses Q_{ext} show some interesting modes with comparably high quality factor which should be further investigated. They are discussed below. Generally the Q_{ext} seems to be dominated by effects due to the taper.

The results are subdivided into several groups in order to allow their proper discussion. The discussion is limited to some interesting modes since a complete discussion is not feasible due to the large amount of data. Furthermore, for several interesting modes, the absolute value of the electric field is plotted in the two orthogonal planes whose common intersection is the beamline.

The first interesting group is the first monopole band of the 1.75 GHz cavities. It can be seen that their Q_{ext} is relatively high ($\approx 5 \cdot 10^7$). The last mode in this band is located at 1.75 GHz and denoted as the cavities' π-mode with r/Q of 183 Ω. These two modes have the second highest r/Q of all modes located in the 1.75 GHz cavities, as expected. A plot of one of the two π-modes can be seen in Fig. 5.24.

[14] Unfortunately, there is no straightforward way to estimate the accuracy of the approximation. An alternative would be to make an estimation by trying to compute the losses using e.g. CST MWS. Unfortunately, to the authors best knowledge the exact electromagnetic properties of the taper over a sufficient frequency range are not known yet to a satisfying degree and are part of ongoing investigations. So it is unclear if such an additional investigation would bring any more insight into the problem (at the current state of uncertainty). If, in the future, the parameters of the taper are known one could instead measure (or simulate) it's scattering parameters from which it should be possible to compute a non-linear termination impedance that emulates it's behavior. The resulting problem could then be solved by the methodology described in this thesis.

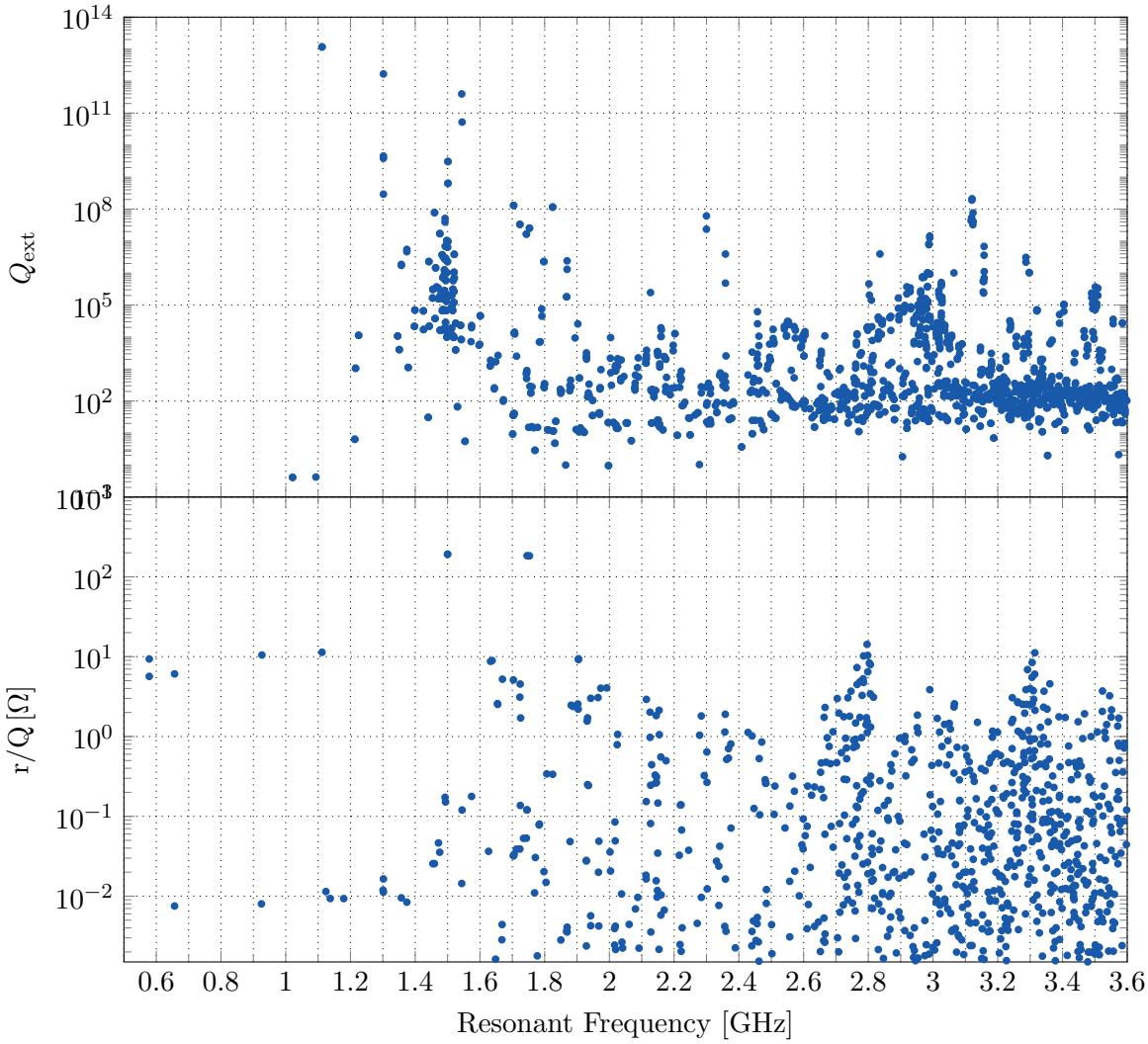

Abbildung 5.23: This plot shows the results for the BESSY$^{\text{VSR}}$ investigation, computed for the chain of cavities shown in Fig. 5.22. The computed values are shown for Q_{ext} (upper plot) and r/Q (lower plot). When computing the r/Q, the modes are computed for the closed structure (since r/Q is not defined for open structures), while Q_{ext} is computed for frequency-matched port-boundary conditions. Therefore, a comparison of both values is only reasonable for high Q_{ext} (since in that case the mode hardly couples to the boundary and is not changed by it). Furthermore, both plots share the same x-axis. For a better overview, modes with a frequency below 0.5 GHz and eigenmodes with a very low computed quantity ($Q_{\text{ext}} < 10^{-1}$ and r/Q $< 10^{-3}$) have been omitted in this plot.

The second interesting group is the first monopole band of the 1.5 GHz cavities. It can be seen that their Q_{ext} is relatively high ($\approx 1 \cdot 10^6$). The last mode in this band is located at 1.50 GHz and denoted as the cavities π-mode. This mode has the highest r/Q of all modes: 192 Ω. Unfortunately, there are comparably many modes at frequencies close to the π-mode frequency. These modes are all located in the taper and discussed later. A plot of one of the two π-modes can be seen in Fig. 5.25.

The third interesting frequency interval consists of several modes with comparably high Q_{ext} and low frequencies from 1.25 - 1.6 GHz. All modes contained in this frequency range (with the exception of the 1.5 GHz π-modes) are located in either of the two tapers. As an example for those modes, one field plot was selected and visualized in Fig. 5.26. The modes of this group are potentially very dangerous due to their high quality factors. It is however very questionable if the modes will exist as computed if the tapers have material losses (the lossy material in the taper was neglected).

The fourth group consists of the first quadrupole-band of the 1.5 GHz cavity located at 3.11 - 3.12 GHz. These modes are especially interesting since they have the highest quality factors of the modes located solely in one cavity. Fortunately, their r/Q is very low. The plot of one mode of this band is shown in Fig. 5.27.

Further interesting are the four modes between 2.3 - 2.4 GHz with Q_{ext} above 10^5. All of them are located in the bellows, two of them in bellow 3 and two in bellow 4. Though their high Q_{ext} makes them potentially dangerous, their r/Q is negligible. One of the four modes is plotted in Fig. 5.28.

The lastly discussed mode is located at 1.797 GHz with Q_{ext} above 10^8. The mode is located in the HOM coupler of the second cavity. Though the high Q_{ext} makes this mode potentially dangerous, its r/Q is negligible. A field plot is shown in Fig. 5.28.

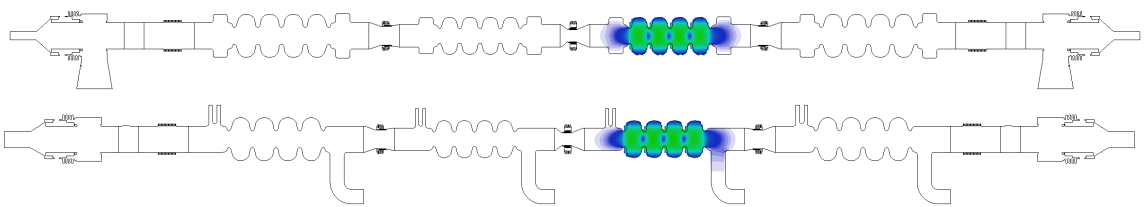

Abbildung 5.24: This picture shows the absolute value of the electric field of one of the two π-modes of the 1.75 GHz cavities resonating at 1.75 GHz with r/Q of 183 Ω.

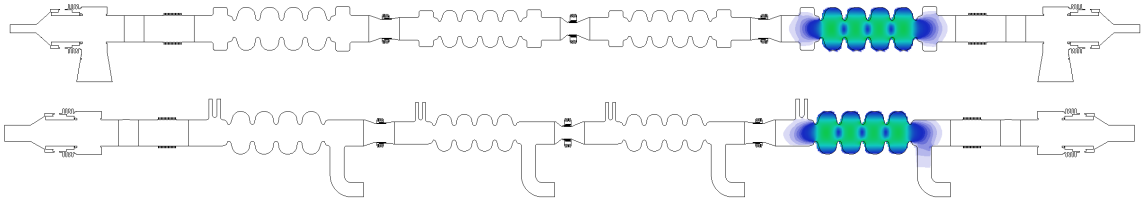

Abbildung 5.25: This picture shows the absolute value of the electric field of one of the two π-modes of the 1.5 GHz cavities resonating at 1.5 GHz with r/Q of 192 Ω.

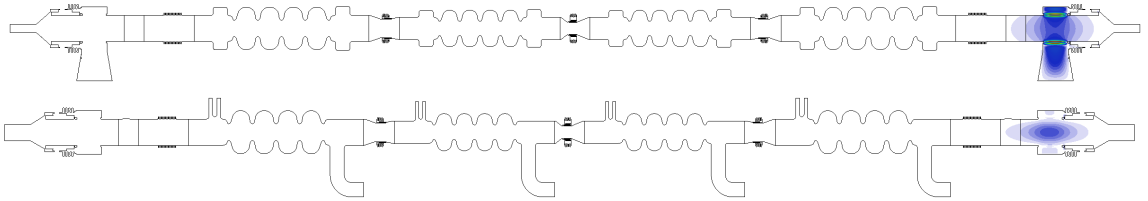

Abbildung 5.26: This picture shows the absolute value of the electric field of one mode that is resonating at a comparably low frequency of 1.5011 GHz inside the taper, dangerously close to the π-modes of the 1.5 GHz cavities.

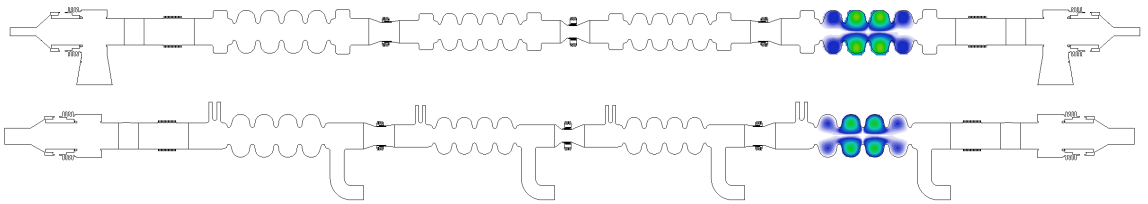

Abbildung 5.27: This picture shows the absolute value of the electric field of one of the modes from the first quadrupole-band of the 1.5 GHz cavities with a resonance frequency of 3.1 GHz. This mode has the highest Q_{ext} of all modes located in the cavities of $2 \cdot 10^8$.

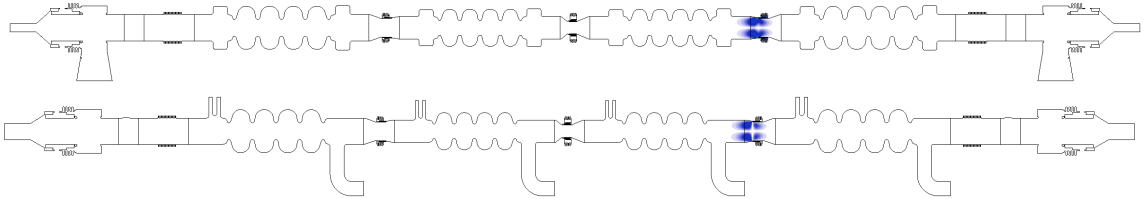

Abbildung 5.28: This picture shows the absolute value of the electric field of one of the modes which are located solely inside a bellow between 2.3 - 2.4 GHz. They are especially interesting due to their high Q_{ext} but do not endanger the beam quality due to their negligible r/Q .

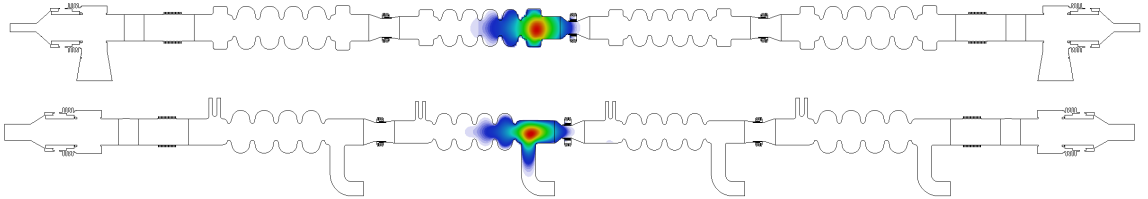

Abbildung 5.29: This plot shows the absolute value of the electric field of a mode with a comparably high Q_{ext} above 10^8. The mode is located in the HOM coupler of the second cavity. Though the high Q_{ext} makes this mode potentially dangerous, its r/Q is negligible.

6 Discussion and Outlook

In this thesis the behavior of electromagnetic fields in complex SRF cavities was investigated using numerical tools for applications in accelerator physics. In this chapter the thesis is shortly reprised and an outlook on possible future applications and developments is given.

To accomplish this task, firstly, the previously by T. Flisgen suggested state-space concatenation scheme was implemented and automated for (almost) arbitrary SRF structures in combination with the finite-integration technique using the commercial software CST MWS. The implementation of SSC allowed to investigate an analytical example and showed that, for simple structures SSC is able to solve the Helmholtz-equation for both the fields and frequencies with the same convergence order as the underlying discretization scheme.

Of special interest in applications from accelerator physics are the losses of certain modes. Therefore, in this thesis a perturbation approach based on SSC was developed, to compute said losses efficiently on workstation computers. In a first step, it was shown that the losses are governed mainly by external losses, such that the other loss mechanism can be neglected. Then, the perturbation approach was layed out where the state-space models of the closed structure are subjected to a termination condition that emulates the losses. The resulting equations formed a nonlinear eigenvalue problem. Said NLEVP was solved using the Newton method with a deflation technique. Furthermore, the implemented algorithm was compared to other available methods like pole-fitting and various linearization approaches, showing that pole-fitting and the suggested algorithm deliver similar results. It was also shown that the proposed algorithm is physically consistent regarding a length variation of the beam pipe, while the commonly applied linearization techniques are not. The results for one example structure were partly compared to measurements.

Both methods, the automation of SSC and the solver for the NLEVP, were used to solve three scientific questions of current accelerator physics projects: the Third Harmonic Module of the FLASH accelerator, the bERLinPro main linac and the BESSY$^{\text{VSR}}$ cavities. Firstly, a purely academic example, which has no practical application, was discussed. The example investigated the change of r/Q and the resonance frequencies when one or two similar resonators are concatenated in a chain, thus indicating that it is in fact necessary to take the full structure into account if there are multiple resonators and that the results for the full structure cannot be fully captured by simulation of only a single resonator.

For the Third Harmonic Module, SSC was applied in order to enhance the available literature since there is currently no investigation that takes the full structure (with correct coupler angular position) and the non-simplified NLEVP into account. Therefore, the r/Q , the Q_{ext}, the S-parameters and several field plots were computed using the methods outlined in Chapter 3 and 4. It was shown that, due to the concatenation of several resonators, there are several inter-cavity modes that resonate between the cavities. These results further motivate the investigation of the full structure, since said modes were not found by previous investigations where a single resonator was taken into account. Furthermore, the S-parameters were compared to measurements and showed a qualitative agreement.

The second real-life structure that was investigated, was the bERLinPro main linac cavities. In this example, two possible design candidates were compared and investigated for dangerous modes. Therefore, the r/Q , the Q_{ext} and several field plots were computed using the earlier outlined methods. It was shown that both designs are very similar regarding their RF-properties but that in one of the design the r/Q of a potentially dangerous mode can be reduced by roughly 30 %.

As last example, the cavities for the BESSY$^{\text{VSR}}$ upgrade were discussed. This example was particularly interesting since there are two sets of cavities with different π-mode frequencies (four cavities in full). The designs for both cavity types were made separately. Therefore, the task of this investigation was to show that there are no unwanted modes introduced by the concatenation of all cavities. It was shown using the suggested methods, that there are some modes located in the taper that might be dangerous regarding their Q_{ext}. Since material losses in the taper were not taken into account, this should be studied further in the future. For the r/Q there were no modes found that can interact well with the beam in a potentially dangerous manner.

In the future, the goal for SSC is to improve the performance further to allow a scaling beyond 10^8 DOFs. Currently, there are two possible improvements related to the MOR. Firstly, the number of samples for the corrected modal expansion in the MOR can be drastically decreased by employing a greedy positioning of the frequency samples instead of an equidistant sampling. The second possible improvement could be the usage of a proper orthogonal decomposition instead of a corrected modal expansion, which would make the necessity of an eigensolver obsolete. For the discretization technique it might be advantageous to have a deeper look into the efficient discretization with FEM. While the current implementation gives promising first results, the performance is simply not sufficient (yet). Also very interesting could be a discretization with isogeometric analysis which was discussed in depth in [112] and [113].

For the NLEVP, in future investigations, the performance can be drastically improved by using methods that allow for a guaranteed complete solution, which

the applied Newton methods with deflation does not. A possible method would be the use of contour integrals, which was investigated using the proposed perturbation approach in [114] and shows promising results. In the future it would be also interesting to use the proposed solver to investigate the effect of HOM absorbers on large SRF cavities.

For the applications there are various, more advanced investigations possible. An appropriate next step would be to compute the fields in the entire accelerating structure of FLASH which includes not only the shown 3.9 GHz Third Harmonic Module but also the 1.3 GHz cavities. For BESSY$^{\mathrm{VSR}}$ it is necessary in the future to include the effects of the tapers for a more accurate computation of multi-cavity modes as well as the losses in the taper. This will be possible by neglecting the lossy tapers in the physical model and emulating them by a frequency dependent termination impedance.

Generally, in this thesis it was shown that the automation of SSC, as well as the efficient assembly of the NLEVP and its solution with the Newton method are applicable with ease to arbitrary SRF structures and thus for real-life problems in accelerator physics. The discussed algorithms were applied to solve the Helmholtz-equation and the NLEVP for up to $3 \cdot 10^7$ DOFs on a workstation computer. In the future, several improvements can be made to potentially scale beyond 10^8 DOFs to allow for new, previously impossible investigations in the context of modern accelerator projects.

A SSC Parameters Practical Applications

To give more in-depth context for all performed computations in Chapter 5, all relevant parameters for the SSC computations are summarized in this appendix. That includes (among others) e.g. the number of DOFs for all segments as well as the computational times. As mentioned earlier in Chapter 4.6, all computations were performed on a Intel(R) Xeon(R) CPU E5-2687W @3.4 GHz with 256 GB of RAM, running on Windows Server 2012 as operating system.

A.1 FLASH Third Harmonic Module

In table A.1, the key parameters of the SSC computation for the FLASH Third Harmonic Module are comprised.

Tabelle A.1: This table comprises the properties of the computations conducted in Chapter 5.2. The computations were performed using SSC as outlined in this thesis. It should be noted that the sum of the DOFs of the discretization is rather in the range of 15 Mio. since some models (like e.g. the cavity) were used multiple times.

Structure name	DOFs	3D Modes	2D Port modes	$\sum$ Time
Bellow	427.119	45	[15,15]	38 min 2 s
9-cell cavity	1.146.471	300	[15,15]	4 h 16 min
Input coupler	996.930	200	[15,3,1,15]	1 h 25 min
Input coupler inv.	996.930	200	[15,3,1,15]	1 h 25 min
HOM coupler	435.600	200	[15,1,15]	55 min 46 s
HOM coupler inv.	435.600	200	[15,1,15]	55 min 46 s
$\sum$	10.077.225			$\sum$ 11h 33 min

A.2 bERLinPro

In table A.2, the key parameters of the SSC computation for the bERLinPro Main Linac are comprised.

Tabelle A.2: This table comprises the properties of the computations conducted in Chapter 5.3. The computations were performed using SSC as outlined in this thesis. It should be noted that the sum of the DOFs of the discretization is rather in the range of 9 Mio. since some models (like e.g. the cavity) were used multiple times.

Structure name	DOFs	3D Modes	2D Port modes	$\sum$ Time
Cavity	322500	600	[10,10]	5h 15 min
Left HOM coupler	472140	200	[10,5,5,5,10]	5h 39 min
Left Input coupler	436128	200	[10,5,5,1,10]	5h 9 min
Right HOM coupler	472140	200	[10,5,5,5,10]	5h 27 min
Right Input coupler Fig.	436128	200	[10,1,5,5,10]	5h 9 min
$\sum$	2,139.036			$\sum$ 2d 5h 18 min

A.3 BESSY$^{\mathbf{VSR}}$

In table A.3, the key parameters of the SSC computation for the Bessy VSR Cavities are comprised.

Tabelle A.3: This table shows several parameters which have to be chosen for the discretization and the following MOR.

Structure name	DOFs	3D Modes	2D Port modes	Time System Creation	Time MOR	$\sum$ Time
Warm taper up	2,982.996	650	[8,25,16]	6 h 15 min	1 d 4 h 16 min	1 d 10 h 31 min
Valve up	54.777	70	[16,16]	1 min	5 min	6 min
Bellow 1	287.595	70	[16,20]	4 min	52 min	56 min
Cavity 1	5,096.520	500	[20,7,7,1,7,7,7,20]	8 h 47 min	14 h 15 min	23 h 2 min
Bellow 2	1,096.095	70	[20,20]	21 min	4 h 15 min	4 h 36 min
Cavity 2	4,438.476	500	[20,7,7,1,7,7,7,20]	7 h 4 min	10 h 16 min	17 h 20 min
Bellow 3	1,010.685	70	[20,20]	25 min	4 h 21 min	4 h 41 min
Cavity 3	4,438.476	500	[20,7,7,1,7,7,7,20]	7 h 4 min	10 h 16 min	17 h 20 min
Bellow 4	1,096.095	70	[20,20]	21 min	4 h 15 min	4 h 36 min
Cavity 4	5,230.764	500	[20,7,7,1,7,7,7,20]	9 h 14 min	14 h 56 min	1 d 10 min
Bellow 5	287.595	70	[20,20]	4 min	52 min	56 min
Valve down	54.777	70	[20,16]	1 min	5 min	6 min
Warm taper down	2,982.996	650	[16,25,8]	6 h 15 min	1 d 4 h 16 min	1 d 10 h 31 min
$\sum$	30.697.769					6 d 1 h 51 min

B Discrepancies between Measurements and Results

In Chapter 4.6 and 5.2 numerically computed results are being compared to measurements. Both results fit relatively well even though there are some distinct differences to be observed. The reason behind these differences is unclear, yet there are several possibilities, which are comprised in this appendix. It is very likely that the disturbances between measurements and simulated results originate from a mixture of multiple of these reasons. However, it is very hard to estimate the single effect of each seperate error source.

The main reasons for differences are (in arbitrary order):

- There are geometric deviations between the computed design-structure and the fabrication of the measured structure due to finite production accuracies.
- The termination impedances are assumed to be perfectly matched in the simulations, while in real-life the reflections on each port are uncertain and very likely not zero.
- The cooled-down structure is geometrically perturbed compared to the warm structure.
- SSC and the underlying discretization scheme have a finite numerical accuracy.
- Generally the CAD model used for the simulations is a simplification of the real-life structure.
- There are certain simplifications assumed when transforming the simulations into the measurement framework in Chapter 5.2.
- In all simulations, the bellows are assumed to be superconducting, which is a major simplification.

Literaturverzeichnis

[1] H. Padamsee, J. Knobloch, and T. Hays. *RF Superconductivity for Accelerators*. Wiley Series in Beam Physics and Accelerator Technology. Wiley, 1998.

[2] A. Velez, J. Knobloch, and A. Neumann. BESSY VSR 1.5 GHz Cavity Design and Considerations on Waveguide Damping. *Proc. of IPAC*, 14, 2014.

[3] H. Padamsee. *RF Superconductivity: Science, Technology and Applications*. John Wiley & Sons, 2009.

[4] S. Posen, M. Liepe, and D. L. Hall. Proof-of-Principle Demonstration of Nb3Sn Superconducting Radiofrequency Cavities for high Q0 Applications. *Applied Physics Letters*, 106(8):082601, 2015.

[5] L. Lee, C. Ng, Z. Li, and K. Ko. Omega3P: A Parallel Finite-Element Eigenmode Analysis Code for Accelerator Cavities. Technical report, 2009.

[6] W. Ackermann, T. Weiland, et al. High Precision Cavity Simulations. In *Proceedings of the 11th International Computational Accelerator Physics Conference*, pages 1–5, 2012.

[7] T. Flisgen, H.-W. Glock, and U. van Rienen. Compact Time-Domain Models of Complex RF Structures based on the real Eigenmodes of Segments. *IEEE Transactions on Microwave Theory and Techniques*, 61(6):2282–2294, 2013.

[8] T. Flisgen. *Compact State-Space Models for Complex Superconducting Radio-Frequency Structures Based on Model Order Reduction and Concatenation Methods*. PhD thesis, University of Rostock, 2015.

[9] K. Wille. Physik der Teilchenbeschleuniger und Synchrotronstrahlungsquellen. Technical report, 1992.

[10] R. Landua. Accelerating Science, Das CERN als Beschleuniger von Technik, Kultur und Gesellschaft. In *Großforschung in neuen Dimensionen*, pages 87–118. Springer, 2016.

[11] S. Appel, O. Frankenheim, Rossbach J., and R. Schmidt. Beschleuniger für Teilchen, Wissen und Gesellschaft. *Komitee für Beschleunigerphysik KfB*, 2016.

[12] T. Behnke, J. Brau, B. Foster, J. Fuster, M. Harrison, J. Paterson, M. Peskin, M. Stanitzki, N. Walker, and H. Yamamoto. The International Linear Collider Technical Design Report Volume 1: Executive Summary. *arXiv preprint arXiv:1306.6327*, 2013.

[13] B. Aune, R. Bandelmann, D. Bloess, B. Bonin, A. Bosotti, M. Champion, et al. Superconducting TESLA cavities. *Physical Review Special Topics-Accelerators and Beams*, 3(9):092001, 2000.

[14] J. Heller, T. Flisgen, and U. van Rienen. Computational Benefits Using an Advanced Concatenation Scheme Based on Reduced Order Models for RF Structures. *Physics Procedia*, 79:38–45, 2015.

[15] T. Flisgen, J. Heller, T. Galek, L. Shi, N. Joshi, N. Baboi, R. M. Jones, and U. van Rienen. Eigenmode Compendium of the Third Harmonic Module of the European X-Ray Free Electron Laser. *Physical Review Accelerators and Beams*, 2017.

[16] J. C. Maxwell. *A Treatise on Electricity and Magnetism*, volume 1. Clarendon press, 1881.

[17] S. L. Altmann. *Rotations, Quaternions, and Double Groups*. Courier Corporation, 2005.

[18] R. E. Collin. Field Theory of Guided Waves. *McGraw-Hill*, 1960.

[19] R. P. Feynman. *Quantum Electro Dynamics QED*. Adelphi, 1999.

[20] I. N. Bronstein, J. Hromkovic, et al. *Taschenbuch der Mathematik*, volume 1. Springer-Verlag, 2012.

[21] R. P. Johnson, R. E. Hartline, C. M. Ankenbrandt, M. Kuchnir, A. Moretti, M. Popovic, M. Alsharoa, E. L. Black, K. Cassel, D. M. Kaplan, et al. Gaseous Hydrogen and Muon Accelerators. In *AIP Conference Proceedings*, volume 671, pages 328–336. AIP, 2003.

[22] E. Yamashita. *Analysis Methods for Electromagnetic Wave Problems*, volume 1. Artech House on Demand, 1990.

[23] S. A. Schelkunoff. Some Equivalence Theorems of Electromagnetics and their Application to Radiation Problems. *The Bell System Technical Journal*, 15 (1):92–112, 1936.

[24] G. Piefke. *Feldtheorie I*. 1974.

[25] F. Reimann, U. van Rienen, P. Michel, and U. Lehnert. A Dielectrically Lined Rectangular Waveguide as a Wakefield Dechirper for ELBE. In *Electromagnetics in Advanced Applications (ICEAA), 2015 International Conference on*, pages 827–830. IEEE, 2015.

[26] K. Zhang and D. Li. *Electromagnetic Theory for Microwaves and Optoelectronics*. Springer Science & Business Media, 2013.

[27] A. Bondeson, T. Rylander, and P. Ingelström. *Computational Electromagnetics*, volume 51. Springer Science & Business Media, 2005.

[28] T. Weiland. Eine Methode zur Lösung der Maxwellschen Gleichungen für sechskomponentige Felder auf diskreter Basis. *Archiv fr Elektronik und Übertragungstechnik*, 31(3):116–120, 1977.

[29] T. Weiland. Time Domain Electromagnetic Field Computation with Finite Difference Methods. *International Journal of Numerical Modelling: Electronic Networks, Devices and Fields*, 9(4):295–319, 1996.

[30] U. van Rienen. *Numerical Methods in Computational Electrodynamics: Linear Systems in Practical Applications*, volume 12. Springer Science & Business Media, 2012.

[31] M. Clemens and T. Weiland. Discrete Electromagnetism with the Finite Integration Technique. *Progress In Electromagnetics Research*, 32:65–87, 2001.

[32] K. Yee et al. Numerical Solution of Initial Boundary Value Problems involving Maxwells equations in Isotropic Media. *IEEE Trans. Antennas Propag*, 14(3): 302–307, 1966.

[33] T. Weiland and R. Wanzenberg. *Wake Fields and Impedances*. Springer, 1992.

[34] M. Clemens and T. Weiland. Transient Eddy-Current Calculation with the FI-method. *IEEE Transactions on Magnetics*, 35(3):1163–1166, 1999.

[35] P. Fellinger, R. Marklein, K. J. Langenberg, and S. Klaholz. Numerical Modeling of elastic Wave Propagation and Scattering with EFIT Elastodynamic Finite Integration Technique. *Wave motion*, 21(1):47–66, 1995.

[36] T. Weiland, U. van Rienen, P. Hülsmann, W. F. O. Müller, and H. Klein. Investigations of Trapped Higher Order Modes using a 36-cell Test Structure. *Physical Review Special Topics-Accelerators and Beams*, 2(4):042001, 1999.

[37] M. A. Armstrong. *Basic Topology*. Springer Science & Business Media, 2013.

[38] CST MWS®. Computer Simulation Technology: Microwave Studio. *Computer Simulation Technology Studio, Darmstadt, Germany*, 2014.

[39] A. C. Antoulas. *Approximation of large-scale dynamical Systems*, volume 6. SIAM, 2005.

[40] T. Wittig. *Zur Reduzierung der Modellordnung in elektromagnetischen Feldsimulationen*. Cuvillier Verlag, 2003.

[41] A. C. Antoulas, D. C. Sorensen, and S. Gugercin. A Survey of Model Reduction Methods for large-scale Systems. *Contemporary mathematics*, 280: 193–220, 2001.

[42] H.-W. Glock, K. Rothemund, and U. van Rienen. CSC-A Procedure for Coupled S-parameter Calculations. *IEEE Transactions on Magnetics*, 38(2): 1173–1176, 2002.

[43] RL Haupt. Using MATLAB to Control Commercial Computational Electromagnetics Software. In *ACES*, volume 23, pages 98–103, 2008.

[44] C. Baer, B. Hattenhorst, C. Schulz, B. Will, I. Rolfes, and T. Musch. Effective Permittivity Determination of Randomized Mixed Materials using 3D Electromagnetic Simulations. In *Microwave Symposium (IMS), 2015 IEEE MTT-S International*, pages 1–4. IEEE, 2015.

[45] F. Yaman, T. Weiland, and W. Ackermann. Comparison of Eigenvalue Solvers for Large Sparse Matrix Pencils. 2012.

[46] R. B. Lehoucq, D. C. Sorensen, and C. Yang. ARPACK Users Guide: Solution of Large-Scale Eigenvalue Problems with Implicitly Restarted Arnoldi Methods (SIAM, Philadelphia, 1998). *The software and this manual are available at URL http://www. caam. rice. edu/software/ARPACK*, 1989.

[47] C. C. Paige and M. A. Saunders. Solution of Sparse Indefinite Systems of Linear Equations. *SIAM journal on numerical analysis*, 12(4):617–629, 1975.

[48] A. Henderson, J. Ahrens, C. Law, et al. *The ParaView Guide*. Kitware Clifton Park, NY, 2004.

[49] T. Flisgen, J. Heller, and U. van Rienen. Combined Domain Decomposition and Model Order Reduction to Solve Complex RF Problems using FEniCS. Technical report, 2016.

[50] T. Galek, T. Flisgen, U. van Rienen, A. Neumann, B. Riemann, et al. Traveling Poles Elimination Scheme and Calculations of External Quality Factors of HOMs in SC Cavities. *WEP07, these proceedings*, 2012.

[51] E. Kühn. A Mode-Matching Method for Solving Field Problems in Waveguide and Resonator Circuits. *Archiv fuer Elektronik und Übertragungstechnik*, 27: 511–518, 1973.

[52] R. Mittra, Y. Hou, and V. Jamnejad. Analysis of Open Dielectric Waveguides using Mode-Matching Technique and Variational Methods. *IEEE Transactions on Microwave Theory and Techniques*, 28(1):36–43, 1980.

[53] I. R. R. Shinton and R. M. Jones. Large Scale Linac Simulations Using a Globalised Scattering Matrix Approach. *EPAC08, Genoa, Italy*, 2008.

[54] I. R. R. Shinton, P. Zhang, and T. Flisgen. Report on HOM Experimental Methods and Code. *EuCARD-REP-2013-033*, 2013.

[55] U. van Rienen. Higher Order Mode Analysis of Tapered Disc–Loaded Waveguides using the Mode Matching Technique. *Particle accelerators*, 41:173–201, 1993.

[56] W. Wessel, T. Sieverding, and F. Arndt. Mode-Matching Analysis of General Waveguide Multiport Junctions. In *Microwave Symposium Digest, 1999 IEEE MTT-S International*, volume 3, pages 1273–1276. IEEE, 1999.

[57] S. J. Cooke. Reduced-Order Simulation of Large Accelerator Structures. *Physics of Plasmas*, 15(5):056706, 2008.

[58] K. Rothemund, D. Hecht, U. van Rienen, et al. Calculation of RF Properties of the Third Harmonic Cavity. *LINAC 2004*, 14243:4, 2004.

[59] U. van Rienen, H.-W. Glock, D. Hecht, and K. Rothemund. Computation of Higher Order Modes in TESLA structures. *International Journal of Applied Electromagnetics and Mechanics*, 14(1-4):237–242, 2001.

[60] K. Rothemund, H.-W. Glock, and U. van Rienen. Eigenmode Calculation of Complex RF-Structures using S-Parameters. *IEEE Transactions on Magnetics*, 36(4):1501–1503, 2000.

[61] I. R. R. Shinton, R. M. Jones, Z. Li, and P. Zhang. Simulations of Higher Order Modes in the ACC39 Module of FLASH. *arXiv preprint arXiv:1205.3935*, 2012.

[62] R. M. Jones, L. Shi, and N. Baboi. Simulation of Electromagnetic Scattering Through the E-XFEL Third Harmonic Cavity Module. 2016.

[63] M. Liepe. Superconducting Multicell Cavities for Linear Colliders. Technical report, DESY, 2001.

[64] J. Gao. Analytical Formula for the Coupling Coefficient β of a Cavity-Waveguide Coupling System. *Nuclear Instruments and Methods in Physics Research Section A: Accelerators, Spectrometers, Detectors and Associated Equipment*, 309(1):5–10, 1991.

[65] N. Kroll and D. Yu. Computer Determination of the External Q and Resonant Frequency of Waveguide Loaded Cavities. *Part. Accel.*, 34(SLAC-PUB-5171): 231–250, 1990.

[66] A. Ruhe. Algorithms for the Nonlinear Eigenvalue Problem. *SIAM Journal on Numerical Analysis*, 10(4):674–689, 1973.

[67] I. C. F. Ipsen. Accurate Eigenvalues for Fast Trains. *SIAM News*, 37(9):1–2, 2004.

[68] R. Schuhmann and T. Weiland. Rigorous Analysis of Trapped Modes in Accelerating Cavities. *Physical Review Special Topics-Accelerators and Beams*, 3(12):122002, 2000.

[69] T. Flisgen, J. Heller, and U. van Rienen. Computation of External Quality Factors for RF Structures by Means of Model Order Reduction and a Perturbation Approach. *CERN-ACC-2016-0089*, 2016.

[70] B. Liao, Z. Bai, L. Lee, and K. Ko. Nonlinear Rayleigh-Ritz Iterative Method for Solving Large Scale Nonlinear Eigenvalue Problems. *Taiwanese journal of mathematics*, 14(3A):pp–869, 2010.

[71] B. Liao, Z. Bai, L. Lee, K. Ko, et al. Solving Large Scale Nonlinear Eigenvalue Problem in Next-Generation Accelerator Design. *Preprint August*, 19, 2006.

[72] B. Gustavsen and A. Semlyen. Rational Approximation of Frequency Domain Responses by Vector Fitting. *IEEE Transactions on Power Delivery*, 14(3): 1052–1061, 1999.

[73] B. Gustavsen. Improving the Pole Relocating Properties of Vector Fitting. *IEEE Transactions on Power Delivery*, 21(3):1587–1592, 2006.

[74] H.-W. Glock, T. Galek, G. Pöplau, and U. van Rienen. HOM Spectrum and Q-factor Estimations of the High-Beta CERN-SPL-Cavities. In *IPAC 2010, Kyoto, Japan*.

[75] J.-P. Berenger. A Perfectly Matched Layer for the Absorption of Electromagnetic Waves. *Journal of computational physics*, 114(2):185–200, 1994.

[76] F. Marhauser. Calculations for RF Cavities with Dissipative Material. In *17th International Conference on RF Superconductivity (SRF2015), Whistler, BC, Canada, Sept. 13-18, 2015*, pages 1056–1060. JACOW, Geneva, Switzerland, 2015.

[77] J. Asakura, T. Sakurai, H. Tadano, T. Ikegami, and K. Kimura. A Numerical Method for Nonlinear Eigenvalue Problems using Contour Integrals. *JSIAM Letters*, 1(0):52–55, 2009.

[78] R. Schuhmann. A Study on Non-Linear Eigenvalue Problems for Waveguide-Coupled Electromagnetic Cavities. 2015.

[79] W.-J. Beyn. An Integral Method for Solving Nonlinear Eigenvalue Problems. *Linear Algebra and Its Applications*, 436(10):3839–3863, 2012.

[80] S. Börm and C. Mehl. *Numerical methods for eigenvalue problems*. Walter de Gruyter, 2012.

[81] H. Voss. Numerical Methods for sparse nonlinear Eigenvalue Problems. 2004.

[82] H. Unger. Nichtlineare Behandlung von Eigenwertaufgaben. *ZAMM-Journal of Applied Mathematics and Mechanics/Zeitschrift für Angewandte Mathematik und Mechanik*.

[83] L. B. Rall. *Computational Solution of nonlinear Operator Equations*. Wiley New York, 1969.

[84] T. Betcke, N. J. Higham, V. Mehrmann, C. Schröder, and F. Tisseur. NLEVP: A Collection of nonlinear Eigenvalue Problems. *ACM Transactions on Mathematical Software (TOMS)*, 39(2):7, 2013.

[85] S. G. Zadeh. Personal Correspondance. 2017.

[86] K. Honkavaara, B. Faatz, J. Feldhaus, S. Schreiber, R. Treusch, J. Rossbach, et al. FLASH Upgrade. In *programme code TUOARA01, this conference*, 2010.

[87] T. Khabibouline, N. Solyak, and R. Wanzenberg. Higher Order Modes of a 3rd Harmonic Cavity with an Increased End-Cup Iris. Technical report, Fermi National Accelerator Lab., Batavia, IL (US), 2003.

[88] MATLAB. *Version R2015b*. The MathWorks, Inc., Natick, Massachusetts, USA, 2015.

[89] R. Hess. *The essential Blender: guide to 3D creation with the open source suite Blender*. No Starch Press, 2007.

[90] J. Sekutowicz, R. Wanzenberg, W. F. O. Müller, and T. Weiland. A Design of a 3rd Harmonic Cavity for the TTF 2 Photoinjector. *TESLA-FEL Report: TESLA-FEL*, 5:2002, 2002.

[91] I. R. R. Shinton and N. Juntong. Compendium of Eigenmodes in Third Harmonic Cavities for FLASH and the XFEL. *arXiv preprint arXiv:1204.0391*, 2012.

[92] P. Balleyguier. A straightforward Method for Cavity External Q Computation. *Part. Accel.*, 57:113–127, 1997.

[93] J. R. Bray and L. Roy. Measuring the Unloaded, Loaded, and External Quality Factors of One-and Two-Port Resonators using Scattering-Parameter Magnitudes at Fractional Power Levels. *IEE Proceedings-Microwaves, Antennas and Propagation*, 151(4):345–350, 2004.

[94] A. Khanna and Y. Garault. Determination of Loaded, Unloaded, and External Quality Factors of a Dielectric Resonator Coupled to a Microstrip Line. *IEEE Transactions on Microwave Theory and Techniques*, 31(3):261–264, 1983.

[95] T. Flisgen, H.-W. Glock, P. Zhang, I. R. R. Shinton, N. Baboi, R. M. Jones, and U. van Rienen. Scattering Parameters of the 3.9 GHz Accelerating Module in a Free-Electron Laser Linac: A Rigorous Comparison between Simulations and Measurements. *Physical Review Special Topics-Accelerators and Beams*, 17(2):022003, 2014.

[96] C. Liu. *A Contribution to the Computation of the Impedance in Acceleration Resonators*. PhD thesis, Technische Universität Darmstadt, 2016.

[97] T. Galek, J. Heller, T. Flisgen, K. Brackebusch, and U. van Rienen. Analysis of Higher Order Modes in Large Superconducting Radio Frequency Accelerating Structures. In *Electromagnetics in Advanced Applications (ICEAA), 2015 International Conference on*, pages 239–242. IEEE, 2015.

[98] T. Galek, J. Heller, T. Flisgen, and U. van Rienen. Report on SSC Calculations for bERLinPro Module Containing Three SRF Cavities. *Internal Document*, 2016.

[99] P. Zhang. *Beam Diagnostics in Superconducting Accelerating Cavities: The Extraction of Transverse Beam Position from Beam-Excited Higher Order Modes*. Springer Science & Business Media, 2013.

[100] K. Flöttmann, T. Limberg, and P. Piot. Generation of Ultrashort Electron Bunches by Cancellation of Nonlinear Distortions in the Longitudinal Phase Space. *TESLA-FEL Report: TESLA-FEL*, 6:2001, 2001.

[101] P. Zhang, N. Baboi, and R. M. Jones. Eigenmode Simulations of Third Harmonic Superconducting Accelerating Cavities for FLASH and the European XFEL. *arXiv preprint arXiv:1206.2782*, 2012.

[102] T. Flisgen, H.-W. Glock, N. Baboi, P. Zhang, and I. Shinton. Geometric Modeling of the ACC39 Module.

[103] N. Solyak, I. Gonin, H. Edwards, M. Foley, T. Khabiboulline, D. Mitchell, J. Reid, and L. Simmons. Development of the Third Harmonic SC Cavity at Fermilab. In *Particle Accelerator Conference, 2003. PAC 2003. Proceedings of the*, volume 2, pages 1213–1215. IEEE, 2003.

[104] E. Vogel et. al. Test and Commissioning of the Third Harmonic RF System for FLASH. In *Proceedings of International Particle Accelerator Conference 2010*, pages 4281 – 4283.

[105] E. Harms, H. Edwards, T. Arkan, A. Hocker, T. Khabiboulline, M. McGee, D. Mitchell, N. Solyak, M. Huening, K. Jensch, et al. Third Harmonic System at Fermilab/FLASH. *SRF09, Berlin, Germany*, page 11, 2009.

[106] A. Neumann, W. Anders, K. Brackebusch, A. Burrill, G. Ciovati, W. Clemens, C. Dreyfuss, D. Forehand, A. Frahm, T. Galek, J. Heller, et al. Update on SRF Cavity Design, Production and Testing for bERLinPRO. *Proc. of SRF2015, Whistler, BC, Canada*, 2015.

[107] H.-W. Glock, A. Frahm, J. Knobloch, and A. Neumann. Status of the BERLinPro Main Linac Module. In *7th International Particle Accelerator Conference (IPAC'16), Busan, Korea, May 8-13, 2016*, pages 1823–1826. JACOW, Geneva, Switzerland, 2016.

[108] G. Wüstefeld, A. Jankowiak, and M. Ries. Simultaneous Long and Short Electron Bunches in the BESSY II Storage Ring. *Proceedings of IPAC*, 11: 2936–2938, 2011.

[109] A. Jankowiak, W. Anders, T. Atkinson, A. Burrill, H. Ehmler, A. Föhlisch, P. Goslawski, K. Holldack, J. Knobloch, P. Kuske, et al. The Bessy VSR Project for Short X-Ray Pulse Production. In *7th International Particle Accelerator Conference (IPAC'16), Busan, Korea, May 8-13, 2016*, pages 2833–2836. JACOW, Geneva, Switzerland, 2016.

[110] A Jankowiak, J Knobloch, P Goslawski, and N Neumann. BESSY VSR -Technical Design Study. *Helmholtz-Zentrum Berlin*, 2015.

[111] A. Vélez, H.-W. Glock, A. Neumann, and J. Knobloch. HOM Damping Optimization Design Studies for BESSY VSR Cavities. *Proc. of IPAC 2015, Richmond, USA*, 2015.

[112] J. Corno. *Numerical Methods for the Estimation of the Impact of Geometric Uncertainties on the Performance of Electromagnetic Devices*. PhD thesis, Technische Universität, Darmstadt, 2017.

[113] J. Corno, C. de Falco, and S. Schöps. IsoGeometric State Concatenation Method for Reduced Order Simulation of Complex Accelerator Cavities. In *19th European Conference on Mathematics for Industry*, page 168.

[114] H. Pommerenke. Untersuchung von Konturintegralmethoden zur lokal vollständigen Lösung nichtlinearer Eigenwertprobleme, die auf den Maxwell-Gleichungen basieren. *Master Thesis, Universität Rostock*, 2017.

Selbstständigkeitserklärung

Hiermit erkläre ich, dass ich die vorliegende Dissertation mit dem Titel "Numerical simulation of electromagnetic fields in complex multi-cavity superconducting radio frequency resonatorsßelbstständig und ohne fremde Hilfe und nur unter Verwendung der von mir angegebenen Quellen und Hilfsmittel verfasst habe.

Rostock,

Johann Heller